UNIVERSITY OF CAPE TOWN

DEPARTMENT OF MECHANICAL ENGINEERING

RONDEBOSCH, CAPE TOWN, SOUTH AFRICA

The Feasibility of a Road Vehicle Mounted Aerodynamic Testing Apparatus

Submitted in partial fulfilment of the requirements for the Master of Science in Mechanical Engineering degree

AUTHOR: **ADAMS, JORDAN (ADMJOR001)**

SUPERVISOR: **Prof. C. Redelinghuys**

DATE: **31 March 2011**

COURSE CODE: **MEC5010Z**

Abstract

The decreasing cost and increasing power of modern electronics is enabling academic institutions, businesses and individuals to begin developing small, unmanned aircraft. However, the high cost of low speed wind tunnel testing and the difficulties associated with using purely computational methods to characterize an aircraft, make the development of well calibrated airframes a daunting prospect.

A ground vehicle mounted aerodynamic testing apparatus has been identified as a candidate concept for a low-cost alternative to traditional techniques. This dissertation explores the feasibility of a ground vehicle based system by identifying physical and practical issues facing such a system. The focus is on the two most important physical problems facing the concept. These are: the ride dynamics of a vehicle as it traverses a road, and the extent of the distortion of the airflow around a vehicle. Each of these problems is quantified using approximate methods in order to estimate their influence on the testing of the aircraft in order to determine if the concept is workable.

Acknowledgements

I would like to thank several people who played important roles in helping me complete this dissertation:

My supervisor, Professor Christiaan Redelinhuys, for the encouragement, guidance and patience he has offered in the completion of this dissertation, as well as the many opportunities to attend conferences and expos in the time it took for me to undertake this work.

My friends and fellow students William Norton and Jordi Reddy, who completed their masters dissertations during my studies, with whom I exchanged many thoughts on this project and life in general.

My friend and lecturer in the Department of Mechanical Engineering, Ernesto Ismail, who offered me assistance on a number of occasions with both work and less serious matters.

Tracy Booysen, Chief Scientific Officer in the Department of Mechanical Engineering, who assisted me with my motivation and provided support to me when I needed it.

All of the staff in the Department of Mechanical Engineering with whom I have shared many cups of tea and coffee.

Declaration

I declare that this dissertation contains only my work and that each significant contribution to, and quotation in this report from the work of other people has been cited and referenced. The IEEE convention for citation and referencing has been used.

Where a reference is relevant to an entire paragraph, the reference has been placed after the full stop at the end of the paragraph.

I have not allowed, and will not allow anyone to copy my work with the intention of passing it off as his or her own.

Signed:_____

Jordan Adams

Date:_____

Table of Contents

List of Figures

List of Tables

Glossary of Terms

General

Spatial Frequency	Number of cycles per unit length
Wavenumber	*See: Spatial Frequency*

Abbreviations and Acronyms

ADC	Analogue to Digital Converter
CAA	Civil Aviation Authority
CFD	Computational Fluid Dynamics
c.g.	Centre of Gravity
CSIR	Council for Scientific and Industrial Research
DAQ	Data Acquisition
GPS	Global Positioning System
IIT	Indian Institute of Technology
IMU	Inertial Measurement Unit
IRI	International Roughness Index
ISO	International Organisation for Standardisation
LTI	Linear, Time Invariant
NASA	National Aeronautics and Space Administration
PCC	Portland Cement Concrete
PSD	Power Spectral Density
RMS	Root Mean Square

RN	Ride Number
RPV	Remotely Piloted Vehicle
RTRRMS	Response Type Road Roughness Measurement System
SAMAA	South African Model Aircraft Association
SMD	Spring-Mass-Damper
UAS	Unmanned Aerial Vehicle System
UAV	Unmanned Aerial Vehicle

Statistical Terms

Ergodic	A limited sample of an ergodic process is sufficient to obtain the statistical properties of the entire process. For a surface defined by a random function, the surface is ergodic if the statistical properties of the profile in one plane are the same as that of another profile in another parallel plane.
Homogeneous	The statistical properties of any part of a homogeneous process are the same as the overall process.
Isotropic	The properties of an isotropic process are the same in any direction.
Kurtosis	The fourth-order standardised moment which indicates the sharpness of a probability distribution curve.
Skewness	Third-order standardised moment which indicates an asymmetry between the left and right sides of a probability distribution curve.
Stationary	A stationary process is one with statistical properties which do not change with space or time.

List of Symbols

For clarity, some symbols are defined in the text when the relevant equation is presented. Only the symbols referred to in the text are defined here.

$\vec{a}_A$	Acceleration of point A representing the aircraft c.g.
f	Frequency
f	Number of line source singularities
$G_{z_r}(f)$	Continuous PSD function
$H(f)$	Frequency transfer function
N	Number of harmonics used
R_A	Distance (Radius) from vehicle to aircraft c.g.'s
x_A, z_A	Position coordinates of aircraft in vehicle axis system
$\langle x^v, z^v \rangle$	Vehicle fixed axis system
$\langle x^E, z^E \rangle$	Earth fixed axis system
$\langle x^n, z^n \rangle$	Equilibrium axis system
Z_n	Magnitude of the road signal harmonic
$\bar{z}^2_{\Omega_1 \to \Omega_2}$	Mean square value of road profile in frequency band $\Omega_1 \to \Omega_2$
z_r	Road profile elevation
α	Angle of attack
γ	Slip angle of the flow velocity towards the spanwise direction.
θ	Pitch displacement
ρ	Air density
σ^2	Variance
σ	Standard deviation
ϕ	Velocity potential
ψ	Stream function
Ω	Spatial frequency
ω	Temporal frequency

1 Introduction

The decreasing cost and increasing power of modern electronics is enabling academic institutions, businesses and individuals to begin developing small, unmanned aircraft. However, the high cost of low speed wind tunnel testing and the difficulties associated with using purely computational methods to characterize an aircraft make the development of well calibrated airframes a daunting prospect. A ground vehicle mounted aerodynamic testing apparatus has been identified as a concept for a low-cost alternative to traditional techniques. In the proposed system, a wind tunnel balance is to be mounted at a suitable location on a vehicle such that the force and moment coefficients can be obtained.

The concept of a ground vehicle based aerodynamic measurement system is developed by identifying physical and practical issues facing such a system. The sources of error are identified in the initial evaluation of the system through block diagrams describing the system. The two most important problems are then identified for more detailed study. These are: the ride dynamics of a vehicle as it traverses a road, and the extent of the distortion of the airflow around the vehicle. Each of these problems is quantified using approximate models in order to understand their influence on the testing of the aircraft.

This dissertation begins with the project background and literature review. From this, the proposed system is conceptualised in Chapter 3. The system is broken down and analysed to investigate the error sources present in the system. The chapter ends off by identifying the two main areas of focus which are presented in the following two chapters. In Chapter 4 the ride dynamics of road vehicles is investigated and the results of the modelling and simulation are presented. Chapter 5 deals with the aerodynamics of road vehicles and initial attempts at modelling the system. Following this, results of Chapters 4 and 5 are discussed in Chapter 6 which leads into a discussion of the overall concept. Conclusions are drawn before recommendations are made in Chapter 7.

2 Background and Literature Review

In this chapter the background to this project is presented. This is done by introducing the kinds of small UAVs and model aircraft currently being flown in South Africa that might benefit from a low cost testing apparatus in their development. The regulations restricting the size of the aircraft are presented as they have relevance to the desirable capabilities of the proposed measurement system. The need for an alternative testing system is justified further by discussing the factors which limit the development of UAVs. Alternative types of testing apparatus used in the past are then presented. The chapter ends with a summary of the points motivating the development of the vehicle based system.

2.1 Small UAVs and Model Aircraft in South Africa

Unmanned aircraft in South Africa may be divided into three groups: UAVs made by defence companies and smaller businesses, those made by CSIR and academic institutions, and model aircraft made by hobbyists. Although there are exceptions, the aircraft built by these three groups are separated by their budgets, the facilities they have access to, and the application of the aircraft.

2.1.1 UAVs Produced by South African Defence Companies

Local military contractors such as Denel and ATE have large budgets for their UAV and UAS projects. The largest unmanned aircraft produced in South Africa are Denel's Seeker II [*1*] and ATE's Vulture [*2*]. However, South African military contractors do not exclusively produce these larger UAVs. ATEs Kiwit, shown in Fig. 2.1 below, is a portable hand launched mini UAV capable of capturing video and images and automatic navigation and landing [*3*].

Fig 2.1: ATE's Kiwit mini UAV in flight. [*4*]

Denel has developed a prototype UAV named e-Juba for the National Health Laboratory Services (NHLS). This aircraft, shown in Fig. 2.2, is intended to provide a means of delivering medicines, therapeutic agents, anti-venoms and blood from an NHLS laboratory to a remote clinic. The aircraft is capable of autonomous navigation to a remote site where it can perform a precision landing. [*5*]

Fig 2.2: e-Juba ready for take-off. [*5*]

A smaller UAV was also developed for the NHLS by BFA systems, a small company located in Somerset West in the Western Cape. This micro UAV has a wingspan of 800 mm and is designed to drop smaller payloads. The aircraft can autonomously drop off samples at a predetermined location or have the drop remotely triggered in RPV mode

2.1.2 UAVs Developed by Academic Institutions

The CSIR have been involved with the development of UAVs in South Africa since the early 80's. Recently the CSIR has designed a series of small UAVs intended for use as research platforms and are the subject of combined research with several universities. Images of the most recent UAVs are shown below in Fig. 2.3.

a) b) c)

Fig 2.3: Recent UAVs designed by the CSIR: a) Indiza [*6*] b) Sekwa [*7*] c) Modular UAV [*8*].

The first of these, Indiza, is a small well characterized aircraft built to demonstrate some of the CSIR's capabilities [*9*]. Sekwa is a blended wing body design which was designed as a platform to study variable stability control. It was developed in close conjunction with the

University of Stellenbosch who focussed on the control systems. The wing span was limited to 1.7 m to allow the aircraft to fit into the 7 m and 2 m open section, and 5'x8' low speed wind tunnels at the CSIR. The design cruise speed and mass were 65 km/h and 3.2 kg. [*7*]

The modular UAV is the latest aircraft to be developed by the CSIR and is intended as a multi-purpose research platform with a variety of potential configurations. Though the configuration can potentially be altered, the current prototype has a wingspan of 4 m, a payload mass of 10 kg, and a dash speed of 120 km/h. [*10*]

Other research projects have been undertaken by academic institutions without the direct involvement of the CSIR, such as the Guardian UAVs constructed by the Adaptronic AMTL UAV Research Group at the Cape Peninsula University of Technology (CPUT). This project is a test platform for a number of research projects underway at CPUT. [*11*]

2.1.3 UAVs and Model Aircraft Developed by Hobbyists

The final group of unmanned aircraft are those developed by hobbyists. One is quickly impressed by the capability of some of these model aircraft constructed by individuals in their spare time with their personal funds. UAVs with onboard cameras capable of point to point navigation, circle-and-hold above a location and capturing images and video are currently being built by individuals. Exploring the DIY Drones web site [*12*], with over 10 000 members, gives an indication of the capabilities of the software, electronics and hardware used by hobby UAV enthusiasts. Many examples of projects are given and the website also organises competitions and challenges. This is a clear indication that electronics, software and aircraft components powerful enough to develop autonomous unmanned aircraft are now at a point where they are affordable.

While the apparent achievements and capability of the hobby sphere is impressive, it should not be overestimated. There is little evidence of any significant aerodynamic testing or analysis being conducted. There are, however, a number of individuals with aeronautical backgrounds, or who have educated themselves to a competent level, who attempt to implement technical ideas which they have developed in their private time. While these individuals would benefit from access to aerodynamic testing facilities or CFD analysis of their designs, there are several reasons why these tools are inaccessible to them which are discussed in section 2.3.

2.2 Regulation of Model Aircraft and its Implications for other UAVs

Model aircraft are regulated by the South African Model Aircraft Association (SAMAA).The rules and regulations governing model aircraft are given in the Manual of Procedure for Model Aircraft and Remotely-Piloted Air Vehicle Operation [*13*]. In order to fly an unmanned aircraft without special permission from the CAA, any unmanned aircraft must meet the requirements defined by SAMAA and may only be operated at an approved and registered site. The limits for the specifications of a model aircraft are defined as follows in table 2.1.

Table 2.1: Limits on the specifications of model aircraft as defined by SAMAA [*13*].

Specification	**Destination**
Maximum weight	30 Kg
Maximum wingspan (powered)	5000mm
Maximum wingspan (unpowered)	6000mm

Further restrictions and guides exist for operating the aircraft and for specifying servos and batteries.

These rules are not only relevant to hobbyists. Any aircraft that exceeds these limits requires permission from the CAA in order to fly. Since the Overberg Test Range (OTB) is the only certified test range for conducting experimental testing, classification as a model aircraft offers far more flexibility in an aircraft's testing program [*14*].

2.3 Shortcomings of Current Aerodynamic Testing Methods for the Testing of Model Aircraft

It is apparent that the majority of the unmanned aircraft in South Africa are modest in size. The reasons for this are a combination of many factors including the restrictions imposed by the regulations. Projects of this size, in particular those undertaken by academic institutions, small businesses and hobbyists, typically have small budgets which necessitate a compromise in the aerodynamic development of these aircraft. While electronics and control systems are rapidly becoming cheaper and more powerful, aerodynamic testing is still a key issue.

Wind tunnel testing is the most accurate and reliable way of determining the aerodynamic properties of an aircraft, but is also the most expensive. Large low-speed wind tunnels use high powered electric motors to turn fans which generate the airflow through the test section. The test section is typically fitted with a highly accurate balance system which is used to orient the aircraft and to measure the resulting forces and moments. Low speed wind tunnels are many times larger than their test sections, particularly if a closed circuit wind tunnel is used. The combined costs of the wind tunnel, the housing facility, the electrical power, the sensors and computers, and the personnel required, add up to make wind tunnel testing extremely expensive.

Due to the limited size of the test section in a wind tunnel, a scale model must be built to fit inside the test sections with sufficient space to diminish wall interference effects. These models must be highly accurate and are not trivial to produce. Construction of models for wind tunnel testing represents a significant cost to a low budget project.

To avoid the shortcomings of scale testing, it is possible to test small aircraft at full scale. Full scale testing eliminates scaling errors and allows the opportunity to test the control surfaces and structural strength of a complete prototype of the aircraft. However, testing a full scale aircraft, with a wingspan of even 1 m to 2 m, requires a large wind tunnel. This is exemplified by the Sekwa UAV mentioned in section 2.1.2. The only facility available for testing aircraft with wingspans larger than this is the 7 m wind tunnel at the CSIR. Being the only such facility in the country makes it logistically difficult to utilize as it requires transporting people and equipment to the wind tunnel. The result of this, and the associated high costs, is that small projects typically do not consider wind tunnel testing a feasible option and instead use traditional airframe designs and approximate methods for developing aircraft.

CFD methods are another alternative for studying the aerodynamic performance of an aircraft. However, successfully characterising a full body aircraft using these computational methods is not a simple problem. Turbulence effects, significant at wing-body junctions and in vortical separation from streamlined bodies at high incidence angles, require careful use of appropriate turbulence models to simulate [*15*]. Even when turbulence is not a significant problem, the mesh requirements for solving the flow around a whole aircraft requires great expertise and large numbers of elements to model successfully [*16*].

Panel methods have been used as a less computationally expensive, but more approximate tool for characterising aircraft analytically. Central to the simplicity of this technique is the treatment of the flow as inviscid. While this allows a rapid solution of the flow around a body, it represents a significant approximation. Furthermore, appropriately distributing panels in three dimensions and utilising the correct types of singularities is a substantial task. This again requires expertise to effectively implement and interpret. (Panel methods are discussed in further detail in the Chapter 5)

While computational methods do offer a lower cost solution to wind tunnel testing, the computers, software and skilled personnel required do not represent an insignificant cost. There is also a risk that the results obtained will not be accurate without validation of the results with a physical experiment. For these reasons, only basic computational methods are feasible for low budget projects, if at all.

2.4 Alternative Methods for Low-Speed Aerodynamic Testing

2.4.1 Historical Examples

This section draws heavily from the book 'Wind Tunnels of NASA' by D. Baals and W. Corliss [*17*]*, it is recommended for further reading on the history of aerodynamic measurement and wind tunnels. Other references are cited where appropriate.*

Early attempts at building craft which could mimic the flight of birds were unsuccessful. This was due to a poor understanding of the aerodynamics of flight. A scientific approach was needed in order to understand the flow of air over aerofoils in order to improve their design. Initially, models were tested in places where steady natural wind occurred, such as bridges and caves. The unpredictable nature of the air flow in these locations proved inadequate for scientific study. Clearly, an apparatus was required which would create its own 'wind'.

Some of the first devices created for this purpose were called 'whirling arms'. A sketch of a whirling arm is shown in Fig. 2.4. The aircraft was mounted on the end of a long arm which was spun to generate airflow over test objects placed at the end.

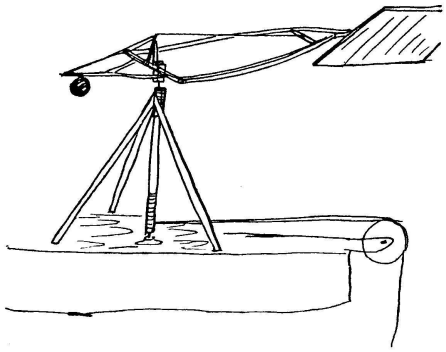

Fig 2.4: Sketch of a whirling arm device
as used by George Cayley in the 1800s [*18*].

The whirling arm was used until the late 19th century. However, it had several flaws, including the curved airflow generated over the test model and the disturbance caused by the model moving through its own wake. Whirling arm devices have been used in recent times for special types of aerodynamic measurement [*19*]; however, wind tunnels have eliminated their use. An example of a modern whirling arm is shown in Fig. 2.5 below.

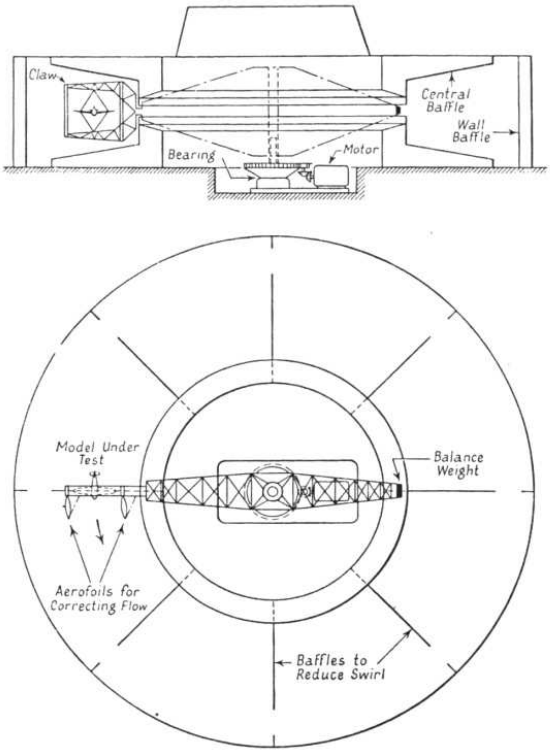

Fig 2.5: Example of a modern whirling arm [*19*].

Another historical case of aerodynamic testing without wind tunnels occurred when the Wright brothers were designing their gliders at the start of the 20th century. They had become dissatisfied with the data available to them at the time and decided to discard all previous data and only rely on their own.

At first a modified bicycle was used to perform testing. An airfoil shape being studied was compared to a reference shape by mounting the two on a third wheel on the side of the bicycle. By riding up and down the streets, the relative wind resulting from the forward velocity of the bicycle would flow over the test rig and allow a crude result to be obtained. The results of the bicycle tests confirmed to them that the current data was incorrect and inspired them to build their own wind tunnel.

2.4.2 Examples of Ground Vehicle Mounted Testing

In ground vehicle mounted testing, the object being tested is mounted onto a road or rail vehicle which is driven at the desired testing speed. In discussions with a number of individuals about the topic of this dissertation, many anecdotal examples of this type of testing were mentioned. Unfortunately, detailed reports on this type of testing have not been found in the published literature. The best documented cases are presented here.

2.4.2.1 SpaceShipOne

SpaceShipOne was the winner of the X-Prize for the first privately developed vehicle to enter space. The rules of the competition imposed limits on the budget for the development of the vehicle. For this reason, it was designed using only CFD methods with no experimental validation. [*20*]

It was clear that the CFD analysis had been insufficient when an unwanted pitch up of the nose was experienced by the test pilot during the first test flight. The unique outboard tail configuration was identified as the source of the problem. The horizontal stabilizers had to be modified and tested, however, there was, no budget available for wind tunnel testing. A low-cost alternative was required.

A full scale model of one of the tails was built and mounted on a pickup truck. The arrangement used is shown in Fig. 2.6. This was driven at speed on an airfield allowing the airflow around the tail modifications to be visualized and led to a successful redesign of the tail.

Fig 2.6: Road vehicle mounted ‘wind tunnel’ for SpaceShipOne [*21*].

The system was not used for characterizing the whole aircraft but provided a means for testing the tail modifications. This system inspired the design of a road vehicle mounted aerodynamic testing system in this dissertation.

2.4.2.2 Towed Parafoil Testing

For several reasons, parafoils are not suitable for scale wind tunnel testing. Brown [*22*] developed an economical, tethered testing technique that was effective in measuring the performance of full scale parafoils. The parafoil was attached to the rear of a utility vehicle. This was driven on a flat dry lake in the Mojave Desert during low wind conditions in the early morning. After inflation, the parafoil was brought under control and measurements were obtained. Using this technique, the lift to drag ratio and lift coefficient of the parafoil could be determined

From 1995 to 2003 NASA developed a prototype vehicle for the recovery of crew from the international space station. This system included a parafoil to control the final descent of the vehicle to landing. In the course of the X-38 program, the parafoil required testing to evaluate its inflation and aerodynamic characteristics. Part of the testing included towed tests behind a truck as shown in Fig. 2.7. The testing was conducted at full scale while a slightly scaled model was used for drop testing. Although the system was successfully tested with a full scale drop test, the program was cancelled in 2003. [*23*]

Fig 2.7: NASA truck towed testing of the X-38 parafoil [*23*].

2.4.3 Parameter Identification and Flight Testing

One further method for obtaining the aerodynamic coefficients of an aircraft is to use parameter identification methods with flight testing. By measuring the response of the aircraft to known conditions, its aerodynamic characteristics can be inferred. Kalman filters are commonly used for parameter identification, although there are a number of techniques which may be used. These methods allow the aerodynamic coefficients of an aircraft to be determined without the direct measurement of aerodynamic forces.

These methods are extremely powerful but require complicated analysis and electronics to implement. The aircraft is at great risk during the flight tests which could potentially result in expensive hardware being destroyed. The aircraft must therefore be stable and controllable by a human pilot in order for the aircraft to be recovered in an emergency or during an unexpected motion of the aircraft. This limits the potential for this method to be applied to unconventional aircraft designs.

2.5 Summary of Background Study

The following important points have been extracted from the background study:

- It is clear from the brief overview of the unmanned aircraft developed in South Africa that the majority of the aircraft are small enough to be classed as model aircraft.
- The electronics required for developing small unmanned aircraft are now affordable to private individuals.
- In order to be classified as a model aircraft a powered unmanned aircraft must have a wing span of less than 5000 mm and the mass must be less than 30 kg.
- It is apparent that, without funds or access to the wind tunnel facilities at the CSIR, aerodynamic testing of model aircraft with wingspans larger than 2 m is impossible without the use of scale models.
- Panel methods and CFD modelling are potentially lower cost alternatives to wind tunnel testing, however, they require skill to implement correctly and the results are not guaranteed to be accurate.
- A ground vehicle mounted aerodynamic testing apparatus is capable of providing useful information in the design of aircraft, however, there is little literature available assessing or reporting the capability of such systems.

These points indicate that a ground vehicle mounted should be assessed as an alternative, low-cost aerodynamic testing apparatus. In the next chapter, the concept is fleshed out and the important key areas to be studied are identified.

3 Conceptualisation of Ground Vehicle Mounted Systems

In this chapter, the research problem is clarified before the basic layout of a ground vehicle mounted system is defined. The layout of the system is evaluated to identify the sources of error and noise. Following this, a block diagram of the system is used to demonstrate how the errors from the various error sources are transferred to the final readings from the system. This diagram leads to the identification of vehicle ride and vehicle aerodynamics as the focus for the further development of the concept. At the end of this chapter, the approach to the study of these two focus areas is given which sets the stage for the proceeding chapters.

3.1 Defining the Research Problem

The research problem can be stated as follows:

Could a ground vehicle mounted aerodynamic testing apparatus provide sufficiently accurate measurement of the forces and moments on a model aircraft, as an accessible, low-cost alternative to wind tunnel testing and CFD?

In order to address this question, it is important to expand on certain aspects of it. These are:

- What is a ground vehicle?
- What can be mounted to a ground vehicle?
- What aerodynamic testing is to be conducted?
- What is a sufficiently accurate measurement of the forces and moments?
- How are the forces and moments measured?
- What is a model aircraft?
- What is meant by accessible?
- What is low-cost?

Before the concept layout of the apparatus is presented, each of the above points is discussed in more detail.

3.1.1 What is a Ground Vehicle?

For the purposes of this dissertation, a ground vehicle is any vehicle which traverses a straight and level surface. The surface may be any existing road, highway, runway, railway or

the floor of a large warehouse or hall. It is also possible to assemble a set of rails specifically for testing. This is commonly done for tracking cameras in the film industry. An example of a low-cost camera dolly using PVC piping as rails is shown below in Fig. 3.1.

Fig 3.1: An example of a low-cost camera dolly [*24*]

The ground vehicle may be specially constructed, or mounted to an existing vehicle. Specially designed vehicles could be self-propelled vehicles or trailers. Options for road vehicles include passenger cars, utility vehicles and trucks. Road vehicles and trailers have specified load limits which must be considered, as well as regulatory requirements if they are to be used on public roads. The regulations are discussed in the next section.

3.1.2 What can be Mounted to A Ground Vehicle?

Unless a purpose built vehicle is designed and built, any apparatus would be required to attach to an existing road vehicle. Options for mounting points include roof racks, tow brackets, bull-bars and roll bars. In addition to these, large custom made roof racks are also now commonly seen on light commercial vehicles. Examples of these are shown below in Fig. 3.2. Note that one of the vehicles pictured is a UCT vehicle.

Fig 3.2: Examples of large, customised roof racks.

The loads transferred to the vehicle must be within both the specifications of the vehicle and load carrying accessories, and within the limits defined by the road traffic regulations. Vehicle manufacturers specify the maximum roof load for their vehicles which is typically 75 kg or 100 kg for passenger vehicles. This corresponds to the load rating of commercially available roof rack components [*25*]. Tow bars have individual specifications for different types of vehicle and hitching which vary greatly. The most important specification for the mounting of an apparatus is the maximum tongue load, defining the maximum vertical load. Bull bar mounting points, roll bars, canopies and other frames fitted to utility vehicles will also have individual load limits. The specifications of these must be checked as they vary from vehicle to vehicle.

If the vehicle is to operate on public roads, it will be subject to the requirements of the National Road Traffic Regulations [*26*]. The requirements for testing on public roads are considered here. If the apparatus is to be operated off public roads, road regulations should still be considered as the vehicle will be required to travel to the testing sites.

Chapter VI of the regulations, referring to the fitness of road vehicles, define the requirements of the vehicle to permit its use on public roads. In Part II, equipment on or in respect of vehicles, regulation 216 states that the vehicle must comply with the requirements of SABS 047 (now SANS 10047) in order to be roadworthy. The only additional requirement found in this standard were those for bumper bars, protective devices (bull bars), bonnets, roof carriers and similar fittings [*27*]. The requirements are simply that the fitting be secure, have no sharp edges and that lights, retro reflectors or number plates must not be obscured.

In studying the regulations relevant to the design of the apparatus, the supporting structure of the apparatus was considered to be a roof rack and the aircraft and balance to be a carried load. Part III of Chapter VI, describing the allowed dimensions of vehicles, is of particular importance to this system. These regulations require the following:

- The highest point on a vehicle, including any load carried, may not exceed 4.3 m.
- The structure of the apparatus may not overhang the front or rear axle by 60% of the wheelbase of the vehicle.
- The apparatus may also not extend sideways from the centre line of the vehicle by more than 1,25 m. Note that this includes the aircraft.

- If the apparatus extends more than 150 mm from the sides, or 300 mm from the rear of the vehicle, the requirements of regulation 229 for increasing the visibility of the apparatus must be adhered to.

As long as the vehicle to which the apparatus is mounted is road worthy and meets these requirements, there is no indication that such a system would be illegal. For safety, the system must not exceed the maximum loads specified for the vehicle, which fall within the limits of the regulations. This does limit the wingspan of the test aircraft to 2.5 m when testing on public roads. Testing would also be limited to 120 km/h. This is the maximum legal speed limit on South African highways defined in Chapter IX, part II, regulation 292 on speed limits.

It is possible that the aircraft mounted to the apparatus could be deemed unsafe by officials despite adhering to the aforementioned regulations. For these reasons airstrips, runways and private roads would need to be used in order to get full use of a ground vehicle mounted testing apparatus.

3.1.3 What Types of Aerodynamic Testing are to be Conducted?

Obtaining the aerodynamic coefficients for a model aircraft and UAVs is the aim of the system. Of initial interest are the longitudinal aerodynamic characteristics, in particular: C_L, C_D, C_M, $dC_L/d\alpha$ and $dC_m/d\alpha$. These aerodynamic characteristics are of increased importance because the lateral dynamics of most aircraft are usually more stable than the longitudinal. They can also be used to determine the range, speed and payload capability of the aircraft as well as the power requirements and other performance characteristics.

In order to obtain these characteristics, the system must be capable of inclining the aircraft at a known angle to a measured air velocity and of sensing the forces moments acting on the aircraft. While it is possible that the aerodynamic coefficients may be obtained at any reasonable speed, it would be desirable to test up to, and at, full speed. Testing with gradually changing speeds may also be possible but is undesirable as the acceleration will cause additional forces which will have to be accounted for.

Additionally, there are other types of testing which may be conducted with such an apparatus:

- The angle of attack may be increased up to and beyond stall to find C_{Lmax} and to investigate flow separation. C_{Lmax} typically occurs between 10° and 15° for low speed aircraft. The zero lift angle of attack may also be studied and typically occurs at a few degrees of negative angle of attack.
- By mounting the aircraft on gimbals, the static stability may be tested. A qualitative evaluation of the control effectiveness may also be obtained. The change in trim angle due to the deflection of trim tabs, elevators, flaps and landing gear may also be investigated. If the aircraft is made to oscillate by being deflected from trim and released, it would be possible to investigate dynamic stability and damping.
- The structure of the aircraft may also be tested under aerodynamic loading. This would allow for the testing of different types of materials and construction methods as well as testing structural monitoring systems.

3.1.4 What is Sufficiently Accurate?

Obtaining the aerodynamic coefficients of model aircraft is the intended application of the proposed system. To this end, the accuracy of the system is defined in terms of its ability to obtain the aerodynamic forces and moments acting on the test aircraft.

The requirements defining sufficient accuracy of the system depend greatly on desired outcomes of the testing. For example: determining if a modification to an aircraft will improve its performance has different accuracy requirements to that of obtaining aerodynamic coefficients for a UAV control system.

Specifying the accuracy required by the system using a specific UAV and its control system requirements was considered. It was realised that, within the scope of the current work, the system could not be modelled with sufficient accuracy and completeness to determine if such requirements could be met. Instead, the major error sources associated with the ground vehicle system are studied and quantified using approximate models. The potential accuracy of the system is assessed based on the magnitude of the errors.

3.1.5 How are Forces and Moments Measured?

Forces and moments on the aircraft are measured using a balance such as those found in wind tunnels. Balances orient the test aircraft in pitch and yaw for testing the longitudinal and lateral aerodynamic coefficients respectively. Forces and moments are transmitted through the balance to load cells in order to be sampled and analysed by a computer. In the case of a spring balance, the loads are transmitted to spring scales for reading.

3.1.6 What is a Model Aircraft?

The limiting specifications of a model aircraft, as defined by the SAMAA, were presented in section 2.2. The most important specifications for a powered aircraft are a maximum wingspan of 5000 mm and a maximum weight of 30 kg. Since the majority of unmanned aircraft developed in South Africa fall within the limits of this category, these specifications will be used to evaluate the system.

3.1.7 What is Meant by Accessible?

In order for the proposed aerodynamic measurement system to be used effectively, it must be available for use within reasonable time, without significant logistical issues and costs. Unless the vehicle can be safely and legally operated on public roads, other sites will be required for testing. Obtaining permission to access these sites would present a hurdle to the operation of the system.

Fair weather with low wind will be required for testing unless the chosen system operates indoors. The problem of testing in good weather conditions is compounded if permission to access a site must be arranged in advance, owing to the changeable nature of the wind. The system must be capable of being prepared at short notice to take advantage of good weather opportunities.

The system is intended to provide an alternative to wind tunnel testing while offering a useful testing platform preferable to flight testing. As long as the testing site can be accessed without difficulty, the vehicle mounted system will be more accessible than any large wind tunnel.

3.1.8 What is Low-cost?

The costs are of key importance to the feasibility of such a system. The system must provide useful experimental results for the model aircraft at a significantly lower cost than basic wind tunnel testing. Without detailed specifications, a cost analysis would be arbitrary at this point. Instead, the costs are discussed in general here. The costs can be grouped as follows:

- The cost of the equipment,
- The cost of housing the equipment
- The power cost of conducting individual tests

First equipment costs were considered. Low-speed wind tunnels and the proposed system share common sensors in the balance and air speed sensor. Although the specifications of these would be different, the costs of these sensing systems have been considered comparable. The base vehicle would represent a significant cost for the vehicle mounted system. However, the intention is that base vehicle would not be used solely for aerodynamic testing and that the apparatus be mounted with only slight modifications to the vehicle. The capital cost of the vehicle would, therefore, not be solely attributed to the testing system. Additionally, the cost of constructing a wind tunnel with equivalent wingspan and speed capabilities to the proposed system could exceed that of an appropriate second-hand vehicle. The cost of equipment has therefore been considered to be significantly lower for the proposed system.

The most significant cost saving with the proposed system would likely originate from the facilities required to house the equipment. An open or closed circuit wind tunnel with even a 1 meter wide test section requires a significant amount of floor space. This space would be permanently occupied by the wind tunnel, requiring large dedicated space. A vehicle mounted apparatus would require, at most, a garage sized area to house, owing to the regulations defining the allowable size of the apparatus.

Next considered were the operating costs. In order to get a rough idea of the cost of a vehicle mounted system, some reasonable examples were considered. Using the price of 93 unleaded petrol as of the 5th of January 2011, the running cost of a 2.0 litre light commercial vehicle is given by the AA as approximately R1.11 per kilometer [*28*]. This corresponds to approximately R133.32 per hour at 120 km/h. While this cost will be increased by the

aerodynamic load on the vehicle and other factors, it is lower than can be expected for operating a large low speed wind tunnel.

For comparison, some basic mechanical power calculations were made for a vehicle and an equivalent wind tunnel. A Toyota Hilux 2.0 VVT-i was chosen as a benchmark medium sized utility vehicle that would be suitable for the proposed system. The vehicle qualifies as a light commercial vehicle (LCV), matching the running cost calculation done previously. The gross vehicle mass (GVM) is 2625 kg, the height and width are 1720 mm and 1760 mm respectively with a ground clearance of 181 mm [*29*]. The drag coefficient of a pickup truck is approximately 0.42 to 0.46 [*30*]. Using these values with a drag coefficient of 0.46, the aerodynamic drag on the vehicle at 120 km/h at sea level is approximately 850 N.

The rolling resistance was calculated using the approximate model given in equation 3.1 below.

$$f_r = 0.01\left(1 + \frac{V}{160}\right) \qquad \textit{Ref [31]} \quad \textit{Eq. 3.1}$$

Here is f_r is the coefficient of rolling resistance and V is the speed in km/h. This gives an approximate coefficient of rolling resistance of 0.0175 at 120 km/h. Multiplying this with the weight of the Toyota Hilux, the rolling resistance is found to be approximately 450 N. Adding the drag force and the rolling resistance and multiplying by the vehicle speed, one finds the power required to maintain the vehicle at 120 km/h is approximately 43.3 kW.

Using $P_t = \frac{1}{2}\rho_t A_t V_t^3$, the jet power for a 5 m^2 wind tunnel at 120 km/h is 113.43 kW at sea level. This is the mechanical power of the air in the test section. The energy ratio is defined as the ratio of the jet power to the power losses in a wind tunnel and it is these losses which the fan must overcome. For closed circuit wind tunnels the energy ratio is typically from 3 to 7, while for an open circuit wind tunnel it is usually closer to 1 [*32*]. This means that, excluding motor and fan losses, the power required for this example wind tunnel could be between 113kW to 16kW depending on the tunnel configuration.

By comparing these approximate power requirements for the two systems, it can be seen that, for the speed considered, the vehicle will most likely require significantly less mechanical power. There is also far less complication in obtaining the required power from the vehicle, as the design of the wind tunnel significantly impacts the power required.

3.2 Constraining the Concept and Layout of the Ground Vehicle Apparatus

With the research problem more clearly defined, the basic concept and layout of the ground vehicle mounted aerodynamic testing apparatus is now presented. At the early stages of this dissertation, it was clear that this topic would be difficult to cover due to the broad range of topics involved. Several decisions were taken to narrow the scope of the investigation. Every effort was made to ensure that the decisions were justified. These decisions are listed and motivated below:

- Limit testing to the longitudinal coefficients

  It was decided to limit the scope of the testing to the measurement of the longitudinal coefficients. This is chiefly because of their increased importance as described in section 3.1.3. Also, designing or acquiring a full six-component balance would likely be too complicated and expensive for a low cost system. Factors influencing the measurement of the lateral characteristics of the aircraft will be noted but not modelled in any detail.

- Utilize a passenger vehicle or utility road vehicle

  A passenger road vehicle or utility vehicle is to be used. This removes the need to design and construct a vehicle capable of powering an aircraft to desired speeds and reduces equipment costs. The merits of using specifically designed vehicles are discussed in chapter 8 but only once the use of a road vehicle has been studied. Light and heavy trucks are not as commonly available and are more expensive to operate and so the focus is on smaller passenger vehicles and light commercial vehicles.

- The apparatus must be road legal

  The vehicle is intended to operate on public roads. This is to allow the greatest flexibility in the use of the apparatus. However, the aircraft wingspan will be limited to 2.5 m and the test speed to 120 km/h. Access to a runway or similar site will be required for larger aircraft or higher speeds. If the apparatus with the aircraft is deemed unsafe, the apparatus without the aircraft must still be road legal to allow transportation to test sites.

After considering these restrictions, the basic layout of the system could be defined. The system in Fig. 3.3 shows a passenger road vehicle with the test aircraft mounted some distance, z_A, above and some distance, x_A, ahead of the vehicle's centre of gravity. The vehicle travels at speed on a road or runway while data from sensors is captured.

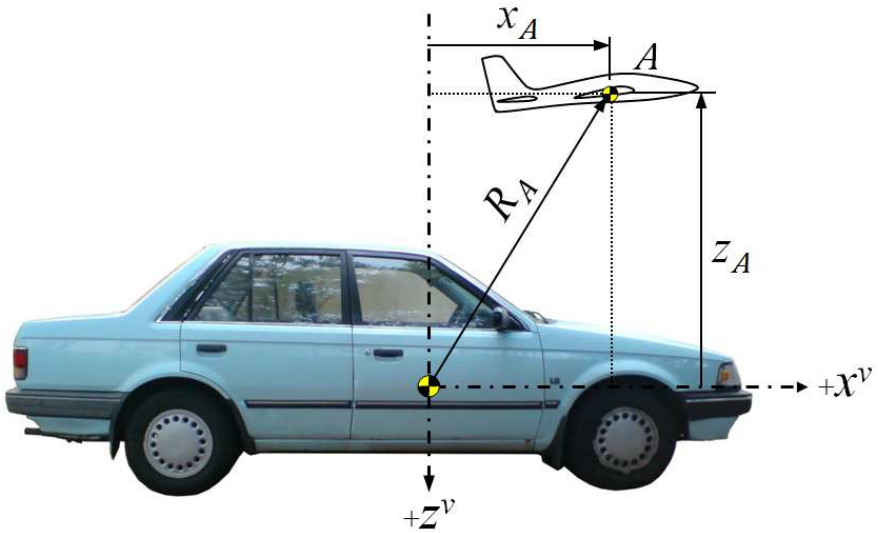

Fig 3.3: Initial concept layout of a ground vehicle mounted system

This concept demonstrates all the main dynamics and errors of a ground vehicle mounted system while offering the potential to test full-scale model aircraft at full speed. Other concepts and modifications to this concept are discussed at the end of this dissertation.

3.3 Summary of System Requirements

The functional requirements and main specifications for the testing system are:

- The system must be capable of supporting large model aircraft.
- The vehicle must reach and maintain a suitable constant speed
- The lift, drag and pitching moment must be measured.
- The balance must actuate the aircraft pitch.
- The aerodynamic forces must be isolated.
- The angle of attack of the aircraft and the airspeed must be measured or inferred.
- The system may not over load the specified limits of the vehicle attachment points.
- The system must fall within the requirements of the national road traffic regulations.

Desirable maximum and minimum specifications of the system identified thus far are given in table 3.1.

Table 3.1: Desired Main Specifications of the System

Specification	Value
Max Aircraft Wingspan	5 m
Max Aircraft Weight	30 kg
Max Balance Pitch Angle	±30°
Max Speed	120 km/h
Max Vehicle Roof Load	100 kg
Maximum Height of Apparatus & Aircraft on Public Road	4.3 m
Maximum Width of Apparatus & Aircraft on Public Road	2.5 m

Note:

- The specifications for the aircraft are the maximum defined by the SAMAA. Most UAVs are smaller than this definition and so this represents a desired maximum. Road regulations limit the maximum allowed wingspan to 2.5 m on public roads. This is still larger than most of the wind tunnels in South Africa can accommodate.
- A maximum angle to the relative wind of 30° is useful for investigating stall and separation. This range is not necessary for determining the aerodynamic coefficients. If the balance can provide this in both directions, it would be possible to do testing with the aircraft inverted.
- The speed of 120 km/h is guided by the dash speed of the CSIR's modular UAV and the maximum speed limit on South Africa's roads. No minimum speed is specified as the aerodynamic coefficients may be obtained at any reasonable speed.
- The vehicle roof load is based on the maximum load typically specified for vehicles and for roof rack components. The weight of the aircraft, balance and structure will be combined with potentially high aerodynamic forces.
- If the apparatus extends more than 150 mm from the sides, or 300 mm from the rear of the vehicle, the requirements of regulation 229 for increasing the visibility of the apparatus must be adhered to.

In order to model the system and quantify the errors, the sources of error are now identified.

3.4 Identifying the Sources of Error in the Basic Layout of the System

The conceptual layout defined in section 3.2 was examined to identify the sources of error and variability in the system. Figure 3.4 summarizes the main areas of concern that have been identified.

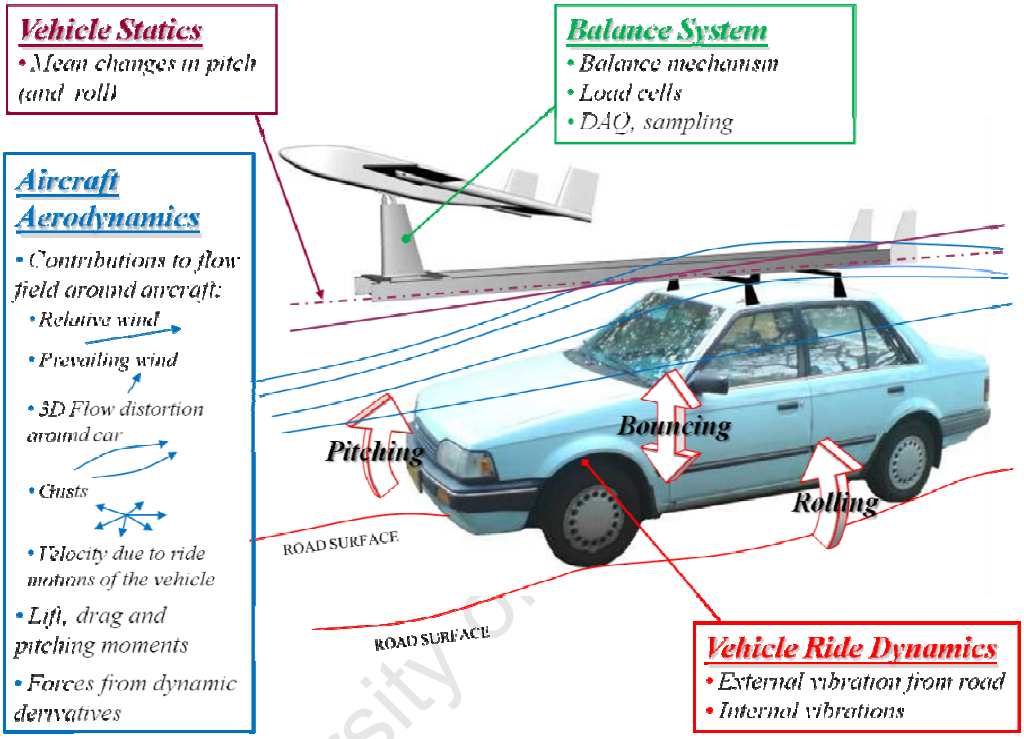

Fig 3.4: Identifying sources of error and variability

The areas identified are: The disturbance of the airflow in the region of the model aircraft, the dynamic ride motions of the vehicle, the mean changes in the orientation of the vehicle and the balance and associated electronic sampling systems. A block diagram of the system was created to investigate how the errors are transferred to the final measurements of the system. Some of the smaller or less significant effects on the system have been omitted in order to focus on the main parts of the system. This is shown on the following page in Fig. 3.5.

The diagram shows how the various inputs affect the inertial and aerodynamic forces transferred to the balance. The four main areas shown in the previous figure have been highlighted in the diagram. The system is clearly quite complicated with several interactions between the different parts of the system. Beginning with the relevant subsection of the block diagram, each of the areas is discussed in the following sections. The final section describes possible sensors to be used to measure some of the undesired effects in the system.

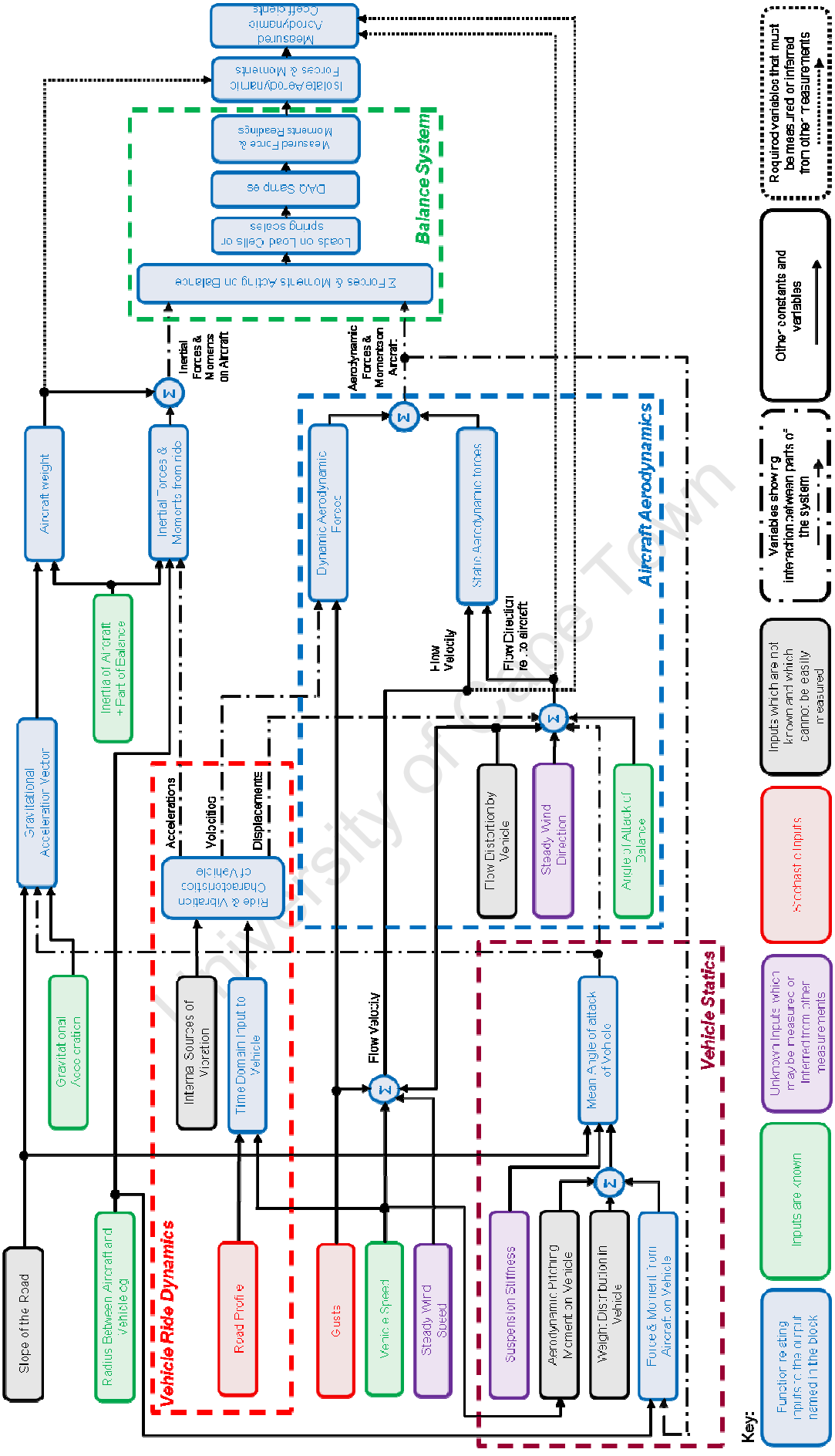

Fig 3.5: Block diagram of the system

3.4.1 Aircraft Aerodynamics

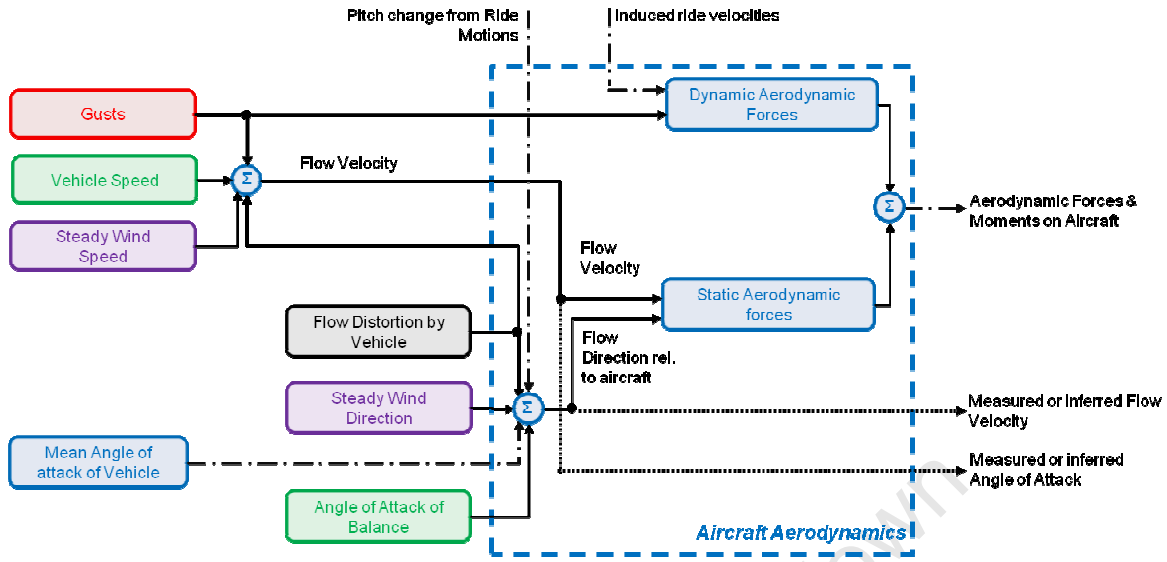

Fig 3.6: Aircraft aerodynamics subsection of the main block diagram

The main aerodynamic characteristics, together with other parameters, predict the forces generated on the aircraft in a straight flow field. The flow field seen by the aircraft in this apparatus is distorted, changing the forces which will be generated. There are at least seven influences on the velocity field seen by the test aircraft which can be identified in Fig. 3.6: The vehicle speed added to the steady wind and the flow distortion by the vehicle combine to produce the main steady part of the flow. The flow deflected over and around the body of the road vehicle causes a change in the direction of the flow which varies within the test area. The overall angle of the flow field is changed by the setting of the balance and the mean angle of attack of the vehicle. Stochastic fluctuations in the flow field are caused by wind gusts and the relative velocity of the aircraft cause by ride motions of the vehicle, which also change the angle of attack of the aircraft.

It is clear that in windy and gusty conditions the system will not be usable. Unpredictable winds will complicate the analysis of the data and will pose a risk to the aircraft. Although it is a major drawback to the system, it is assumed that testing will be conducted in nearly windless conditions which most frequently occur in the early morning. Because of this, gusts and wind have been ignored in the analysis of the system. It should be noted here that by increasing the speed of the testing, the relative influence of gusts and the steady wind will be reduced.

As the vehicle pitches, bounces and rolls due to the ride dynamics of the vehicle, the aircraft will gain small vertical, sideslip and pitch velocities. The magnitudes of the velocities and displacements caused by the pitching and bouncing were investigated with the study of the vehicle ride. One could assume that these velocities would be insignificantly small for a smooth road.

The interaction of the aerodynamics of the aircraft and the aerodynamics of the car is of primary importance. The deflection of the air and the pressure gradient in the flow may be significant if the aircraft is improperly situated. The wake of the aircraft and the wingtip vortices will interact with the complicated flow that exists around the road vehicle. This area has been identified as a key area to be investigated in more detail.

3.4.2 Vehicle Ride Dynamics

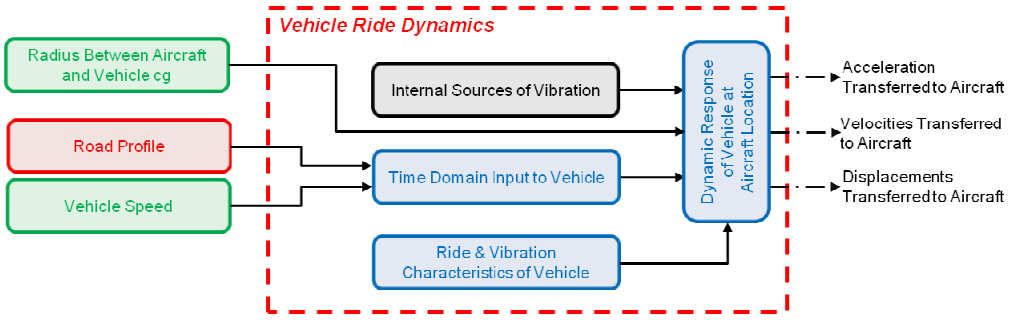

Fig 3.7: Vehicle ride dynamics subsection of the main block diagram

The vehicle ride dynamics subsection of the system is shown above in Fig. 3.7. As a vehicle moves at speed over the road (or runway) variations in the surface will cause the vehicle to pitch, bounce and roll. These displacements, velocities and accelerations will be transmitted to the aircraft through the structure of the apparatus. The acceleration of the mass of the model aircraft will result in inertial forces and moments measured by the balance. The inertia of the components of the balance itself will also contribute to these forces. Additionally, there are internal sources of vibration from the engine, wheels and drive train of the vehicle. These will be transmitted to apparatus to the load cells which will appear on the output as high frequency noise.

The random, oscillating nature of the ride and vibrations in the vehicle will cause variability in the load cell readings, which must be filtered out. More significant ride motions may also affect the aerodynamic forces on the aircraft, as mentioned in the previous section.

Understanding the ride dynamics of a road vehicle was identified as a key area for further study.

3.4.3 Vehicle Statics

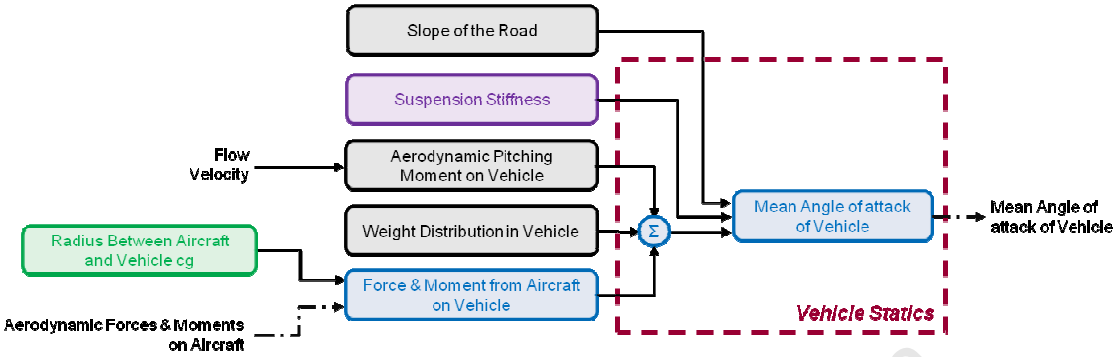

Fig 3.8: Vehicle statics subsection of the main block diagram

The forces and moments measured by the system must be plotted against the orientation of the aircraft to the free stream in order to be translated into useful aerodynamic data. The weight of the aircraft must also be subtracted from the resultant forces and moments measured in order to isolate the aerodynamic forces. This is a problem for this type of system since the mean angle of incidence of the air velocity to the aircraft is not necessarily equal to the angle of the aircraft to the vehicle. Additionally, since the free stream is parallel to the surface of the road which may have some incline, knowledge of the direction of gravity is not sufficient to determine the angle of attack of the aircraft. The factors influencing the angle of attack of the vehicle are shown in Fig. 3.8 above.

There are three main contributions to the difference between the incidence angle of the air velocity to the aircraft and the angle of the aircraft to the vehicle. These are: the flow distortion by the vehicle, the prevailing wind and the mean change in the orientation of the vehicle to the ground. The orientation of the vehicle depends on forces acting on the vehicle which are not constant and vary with speed.

The main forces on the vehicle are: the aerodynamic forces and moments from the vehicle and aircraft, the weight of the vehicle, and the upward normal forces acting through the tyres and suspension. Because of the definition of the aerodynamic pitching moment, there is no need to consider the moment of the tractive force required to maintain the vehicle speed in order to determine the pitch from known data.

The distribution of mass within the vehicle will change as fuel is used, and will depend on the number of passengers and their position in the vehicle. The direction of gravitational acceleration vector relative to the vehicle also changes with the orientation of the vehicle to the road and with the camber and slope of the road. The effect of the changes in mass distribution and the road slope may be small, resulting in only a change of only a few degrees of pitch. This cannot be ignored when determining the angle of attack of the aircraft.

The mean orientation of the vehicle to both gravity and the road are significant variables in the system which must be accounted for. It would be difficult to accurately infer these from other measurements owing to the unknown slope of the road and weight distribution changes during a test. It is therefore suggested in section 3.4.5 that these be measured or avoided though other measurements.

3.4.4 Balance System

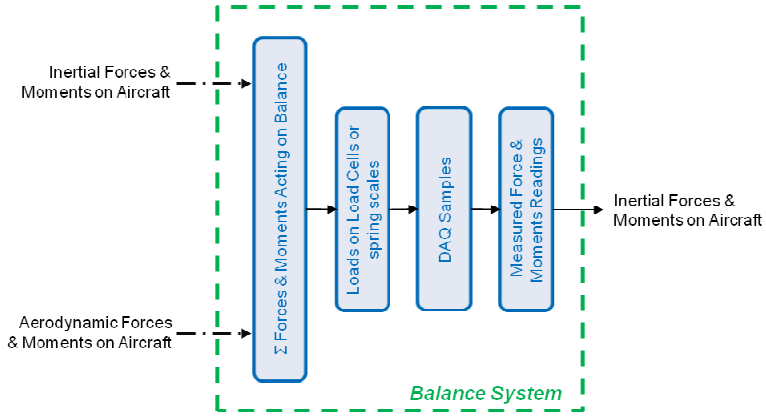

Fig 3.9: Balance system subsection of the main block diagram

The basic block diagram of the balance system is shown above in Fig. 3.9. The vibrating environment in which the balance must operate presents a significant challenge to the design of the balance system. Unless a special spring balance is designed for the system, load cells would be used to measure the loads transmitted through the balance. Load cells have specified ranges in which they are accurate and are sensitive to overload and shock overload. Load cells suffer from several types of errors including: hysteresis, non-linearity, non-repeatability and temperature errors [*33*].

Errors in the accuracy of the load cells are usually small and calibration may be used to correct for some of these errors. Further design of the balance system requires a more detailed understanding of the loads it may experience. Owing to the limited scope of this dissertation,

the details of the balance and load cells are not considered further. The loads likely to be seen by the balance are modelled, as the first step to assessing the feasibility of designing a balance for the system.

3.4.5 Discussion of Additional Sensors for Possible Error Compensation

In order to determine the desired coefficients from the system, more variables are required than only the forces and moments on the aircraft. These are: the air speed, angle of attack and the weight vector of the aircraft. Since the vehicle speed, balance angle and mass of the aircraft are known for a test, one may infer and approximate values for these unknowns. However, additional sensors could be used to obtain more accurate values. The block diagram of the system was studied to evaluate the possibility of measuring each of the variables. The following variables may be measured to improve the system:

3.4.5.1 Flow Velocity

The flow speed and angle may be measured directly using flow sensors. A pitot tube may be used to obtain the speed, so long as it is positioned correctly in the flow. For flow direction, sensors with fast response and high accuracy will be required. Sensors used for flow measurement in wind tunnels are described by Barlow, et al [*34*]. Yaw heads and vane-type angularity probes may be employed for this system. These sensors are extremely accurate but require careful calibration and are not widely available. Simpler wind vanes are not ideally suited to this system because of their limited accuracy.

3.4.5.2 Vehicle Speed

The flow velocity is related to the vehicle speed and is affected by the wind speed and the distortion of the flow around the vehicle. If the distortion of the flow is small and the wind speed negligible, the flow speed can be approximated as the speed of the vehicle. The vehicle speed reading from the speedometer is not an accurate reading of the actual speed. The average speed of the vehicle can be accurately and easily measured using GPS.

3.4.5.3 Vehicle Orientation

If flow distortion by the vehicle is known or insignificant, the angle of attack of the aircraft can be found by adding the angle of the balance to the angle of the vehicle relative to the road. If the road is level, the orientation of the vehicle will also determine the direction of the gravitational acceleration vector relative to the vehicle.

It was noted in section 3.4.3 that the simplest way to deal with vehicle orientation is to measure it directly. This would be possible using range sensors underneath the vehicle or tilt sensors (as long as the vehicle does not have a significant mean acceleration). Measuring the orientation of the vehicle is only required if the angle of attack cannot be easily measured.

3.4.5.4 Inertial Forces

To address the overall problem of undesired inertial forces being transferred to the balance measurements, accelerometers or an IMU may be used. If these are positioned close to, or within, the aircraft, they would allow the inertial forces to be removed from the readings.

Although this would provide excellent additional data for analysis of the output readings, an IMU is an expensive piece of equipment. It may effectively only be used to remove the weight of the aircraft if other effects are minimal or can be averaged or filtered out. Its use must therefore be carefully considered.

3.5 Approach to Further Investigation

The full scope of the problem of modelling a vehicle mounted aerodynamic testing apparatus is now more apparent. From the description of the system in this chapter, and the error sources identified, the approach to further investigation of the system was laid out.

It was decided to limit the scope to evaluating the potential performance of the system by investigating the two main physical problems. These are the ride dynamics of the system, and the influence of the flow around a vehicle on the test aircraft. This focus is justified since the specifications of other components first require a quantitative understanding of these two areas. In the next two chapters the investigation and modelling done in each of these areas is presented. Following this, these two areas are looked at together in order to understand the effect of the position of the aircraft.

4 Vehicle Ride

A vehicle mounted aerodynamic testing apparatus, as proposed in this project, must traverse a real, imperfect road or track at a desired speed. As a result of internal and external influences, the vehicle will be subjected to a wide range of oscillating forces over a broad spectrum of frequencies. These forces result in motions and vibrations that will be transmitted to the testing apparatus, and will cause variation in the measurements obtained. A key aim of this project is to understand and quantify these errors which are determined by the ride properties of the vehicle and by the road surface.

In this chapter, established techniques for investigating and modelling vehicle ride are used to answer the following questions:

- What are the expected accelerations at a chosen location on the vehicle?
- What is the expected variation in the pitch of the vehicle?

The answers to these questions provide a basis from which to assess the feasibility of the use of a balance to measure aerodynamic loads on a model aircraft. To this end, two approaches were followed: Firstly, road roughness models approximating the power spectral density (PSD) curves of roads were used in combination with basic vehicle models to obtain approximate spectral data for the pitch and bounce responses of the vehicle. Secondly, the PSD models were used to generate random road signals which were then used as the input to a dynamic model of the vehicle in SIMULINK.

For simplicity analyses were done using two types of linear, 2-DOF models for the vehicle investigating only the longitudinal ride dynamics. This means only single track road profiles were used which significantly simplified the road modelling.

This chapter begins with a description of the basic concepts of ride. The characterisation and modelling of roads is then introduced. The statistical description of roads is discussed in some detail as it is required as a starting point for the method used to generate random road signals in the time domain. The method used to obtain the PSD curves of the outputs from road inputs is also described. Following this, the two ride models used for this analysis are presented, giving both the frequency transfer functions and block diagram models for each. The results from the ride modelling are then presented followed by discussion.

4.1 Vibration in Vehicles

Vehicle ride is a part of the study of the vibration response of vehicles to oscillating inputs. A road vehicle is subjected to excitation at a broad range of frequencies from both internal and external sources. The vibrations are divided into two categories based on their influence on passengers. High frequency vibrations of the vehicle, from 25 - 20 000 Hz, are audible to passengers and are categorized as noise. Ride is mostly influenced by lower frequency vibrations (0-25 Hz). [*35*]

The audible noise originates from the external influence of the road and from internal sources such as the wheels, engine and drive train. These vibrations cause insignificant displacement of the vehicle, but the forces are transmitted though the vehicle chassis and will therefore be transferred to the testing apparatus. The internal sources of noise are of limited concern for the proposed system as they originate from components which have a fixed frequency at a given speed. This means they may be easily filtered out of the output data. The noise may, however, cause problems for the specification of load cells.

The lower frequency ride motions are caused by forces transmitted through the tyres and suspension to the chassis as the vehicle passes over undulations in the road or track. The magnitudes of the resulting movements and accelerations are of greater concern for a vehicle mounted load measurement system. In order to model these outputs, standard vibration theory is used. The remainder of this chapter deals with the modelling and simulation of these vibrations.

4.2 Characterisation and Modelling of Roads

As a vehicle traverses a road, the wheels move along two parallel tracks which have different, randomly varying profiles. This is interpreted as a displacement input at each wheel causing pitching, bouncing and rolling motions of the vehicle. In order to study vehicle ride, the road must be characterised and modelled to describe different roughness levels of roads. Numerous road models have been developed which are based on decades of road profile measurement and analysis.

Sayers and Karamihas [*36*] have given an overview of road profiling and analysis. A road profile may be measured directly by profilometers or may be measured using a response type road roughness measurement system (RTRRMS). The measurements from these systems are

processed to obtain PSD curves for the roads. This typically involves filtering and corrections, to compensate for systematic errors, and smoothing the curves. The road roughness may then also be expressed in terms of roughness indices such as the IRI (International Roughness Index), RN (Ride Number) or others roughness indicators.

Spectral density curves of road elevation and roughness indices are important for highway engineers and vehicle designers. They allow the roughness levels roads to be compared, and allow the ride isolation of a vehicle to be evaluated and simulated. For this dissertation, only the PSD curves are of importance. The following subsections describe the treatment of the road as a random function and its statistical properties, the roughness models used in the literature, how PSD curves of the slope and acceleration of roads may be obtained, and how road profiles may be simulated.

4.2.1 Statistical Description of Roads

The road profile is defined in Fig. 4.1 below. The earth axis system is defined as positive downwards for consistency with the standard definition of the vehicle axis system.

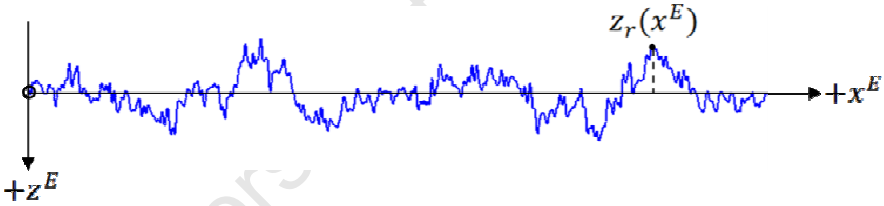

Fig 4.1: Definition of random road function

Road surfaces may be approximately modelled as a two dimensional random function with zero mean and a Gaussian distribution. This function is also commonly assumed to be ergodic, homogeneous, isotropic and stationary. In this case, the statistical properties of roads may be fully described by the spectral densities of the profiles as long as large irregularities such as potholes are ignored [*37*]. This treatment of road allows the statistical properties of a limited section of the profile to be assigned to any track on the entire length of the road [*38*].

The assumptions made in treating a road in this manner are quite significant. Roads have been found to be non-Gaussian and non-stationary, exhibiting characteristics such as high kurtosis and skewness, suggesting that the spectral density may be insufficient for vehicle simulation [*39*]. These deviations are important as the statistical properties of the road profile will affect the properties of the output of the proposed system.

In the literature, the non-stationary and non-Gaussian properties of roads are treated separately [*40*]. The roads in this work will be described using published models which ignore non-Gaussian and non-stationary behaviour. Under these assumptions, the PSD curve of the road elevation of roads is all that is required to fully describe and model the roads. The assumptions are acceptable for the current work as they provide a sufficient qualitative and quantitative assessment of the expected dynamic behaviour of the proposed system.

4.2.2 PSD Functions in the Time and Space Domain

As mentioned in the previous section, the elevation PSD curve of a road is used to describe the statistical properties of a given road. It is important to understand what the elevation PSD curve is and what it means. Stated simply, the area under the elevation PSD of a road between any two frequencies in the band, is equal to the variance of the road signal in that band. This means the curve describes the intensity of the vibrations of the road at different frequencies. The mathematical definition of the PSD is explained in appendix A and is repeated below for the spatial frequency Ω.

$$\bar{z}^2_{\Omega_1 \to \Omega_2} = \int_{\Omega_1}^{\Omega_2} G_{z_r}(\Omega) d\Omega \qquad \textit{Eq. A.7}$$

Here, $G_{z_r}(\Omega)$ is the continuous PSD function and $\bar{z}^2_{\Omega_1 \to \Omega_2}$ is the mean square value of the road profile (equal to the variance) within the band Ω_1 to Ω_2.

The elevation, slope and acceleration PSD curves, given in terms of the spatial frequency, are useful for studying and comparing roads and highways. For ride analysis however, the road must be converted to a time domain input signal. Furthermore, in order to obtain velocity and acceleration outputs for the vehicle, the first and second time derivatives of the road input are used. This means that there are six different PSD functions which are used for describing the road. In appendix A the PSD functions are defined and simple relationships between the different PSD functions are found. This is summarized in Fig. 4.2.

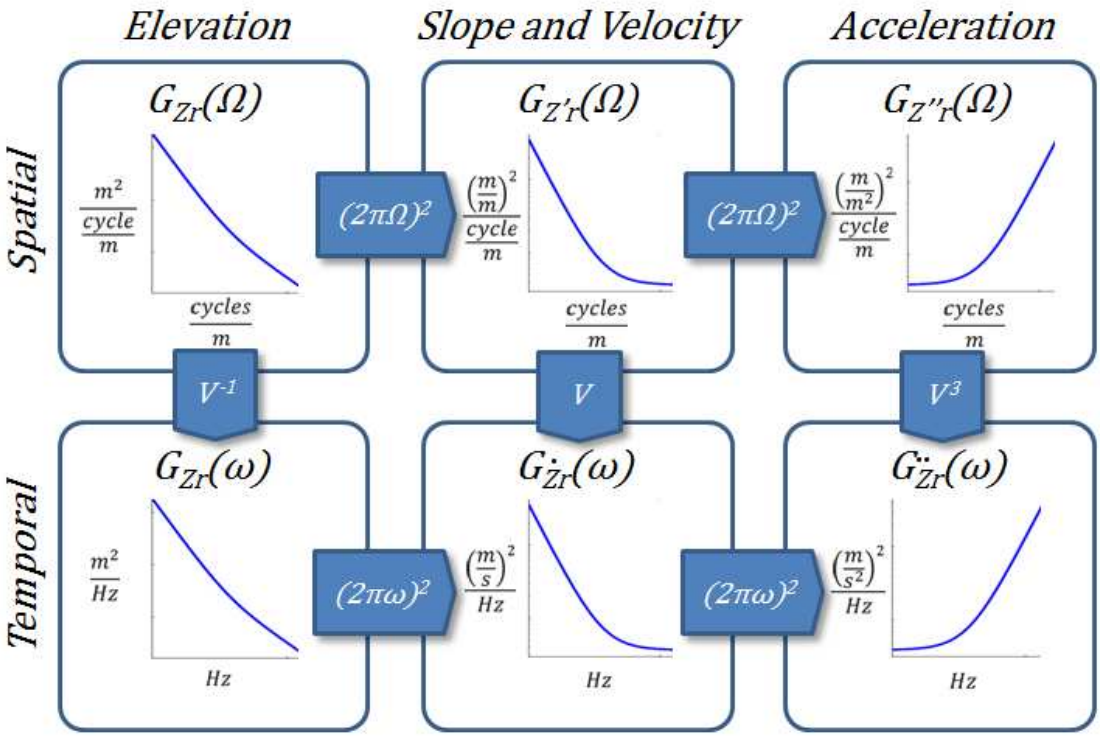

Fig 4.2: Converting between the different PSD functions of the road

In the figure, Ω is the spatial frequency $cycles/m$ and ω is the temporal frequency in Hz. The plots indicate a generic shape of the resulting PSD curves with the vertical axes showing the units of the PSD and the horizontal axes showing the units of frequency. In order to convert between the different forms one must multiply by the factors shown in the blue arrows.

4.2.3 Road Roughness Models

The elevation PSD estimates of roads, highways and runways of different types and roughness levels exhibit a characteristic drop in magnitude with wavenumber. This is because short wavelength deviations have smaller amplitudes than long wavelength deviations in road surfaces [*35*]. Numerous road roughness models have been developed to approximate the average PSD curves found through extensive profile measurement.

In order to draw conclusions about the likely magnitudes of the pitching and bouncing motions of the proposed vehicle apparatus, a set of benchmark road models was required. Three widely used types of road roughness models found in the literature were selected for study and comparison. These are the inverse power type, split power type and a rational function proposed by T. D. Gillespie (referred to from this point on as the Gillespie type). Examples of these are shown in Fig. 4.3 together with the basic forms of the equations.

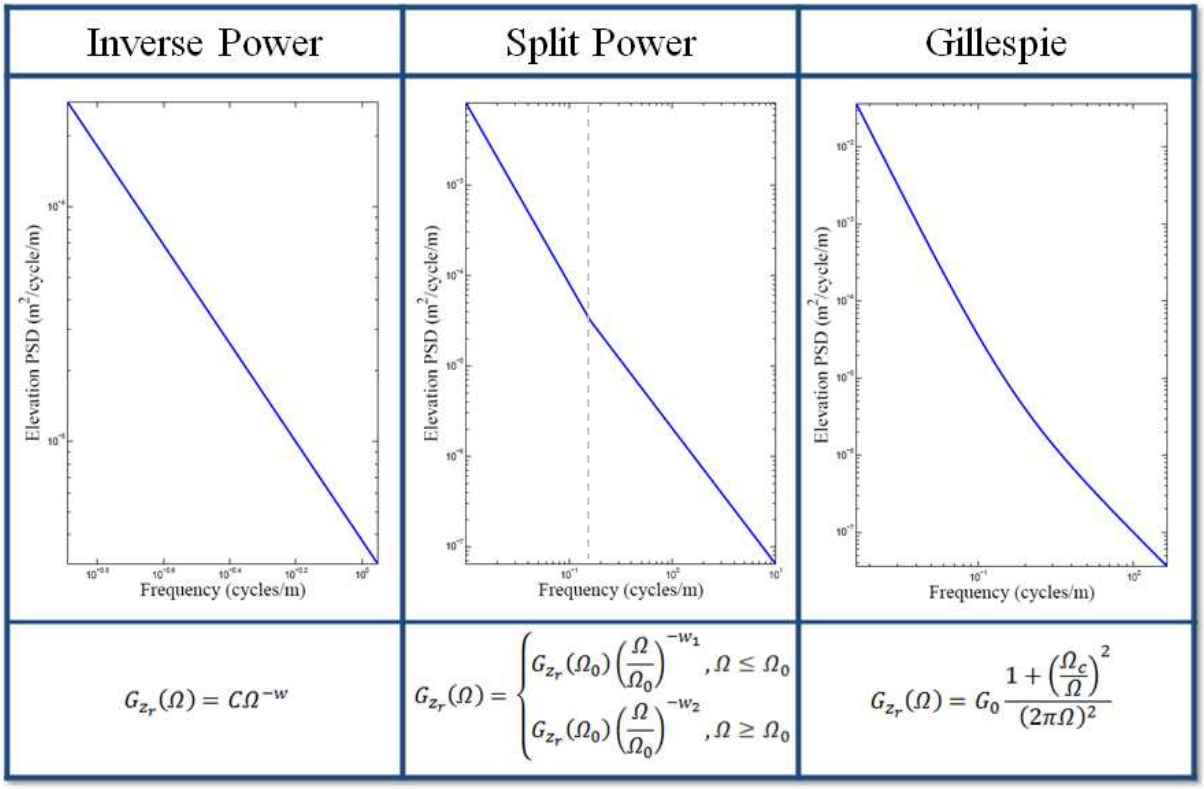

Fig 4.3: Example plots of three road models found in literature with equations

The models contain parameters (C, w, w_1, w_2, Ω_0 and Ω_c) which are used to generate PSD curves for different types of roads with different roughness levels. These are explained in greater detail in appendix B.

Upper and lower wavenumber limits define the bandwidth over which the models are applicable. This band encompasses those vibrations which affect passenger perception of ride, or are defined by the limitations of the measurement system or method. The limited bandwidth does not indicate that there are no other frequencies present in the profile. The omitted frequency components should have limited effect on the system, however, this claim can only be verified with testing.

The models showed wide variation in both the magnitude of the spectral densities and the frequency bands. Of the models investigated, three of the split power models were chosen as benchmarks for investigating the output responses of the system. These were first presented by Dodds and Robson [*37*], and are used in the current ISO standard. The “very good”, “good” and “average” data have been selected as representing appropriate roads for testing and are shown in Fig. 4.4.

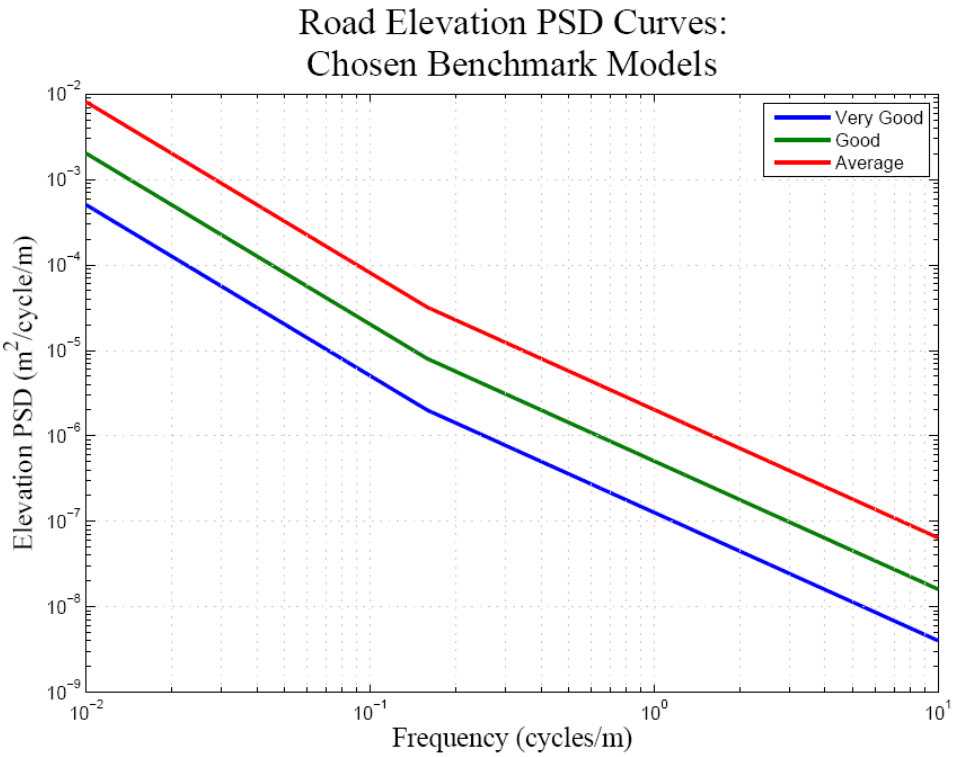

Fig 4.4: Benchmark road roughness models [*37*]

These models also covered the broadest frequency spectrum. The identical shapes and equal bandwidths for the different roughness levels also provides a useful means of finding a range of values at different frequencies. The considerations leading to this choice are explained in more detail in appendix B.

4.2.4 Obtaining Output PSD Curves Using Road Roughness and Vehicle Models

The desired outputs from ride modelling are obtained using the road roughness models defined in the previous sections and vehicle ride models. There are a range of vibration models for vehicles used of varying complexity and detail and in this dissertation only relatively simple models were used. No matter the detail of the model though, the procedure for obtaining the PSD of the output, from the PSD of the road, is the same.

Firstly one obtains a frequency transfer function relating the road input to some desired output. Finding the magnitude squared of this function determines a gain which can be used to find the output PSD according to equation 4.1 that follows.

$$G_{out}(f) = \left|H_{out/in}(f)\right|^2 G_{in}(f) \qquad \textit{Ref [38]} \quad \textit{Eq. 4.1}$$

Where f is the frequency which may be in any consistent units and $H_{out/in}(f)$ is the frequency transfer function relating the inputs to the outputs. However, as long as the input and output functions are both of acceleration, both of velocity or both of displacement, the gain function, $\left|H_{out/in}(f)\right|^2$, is the same. Therefore, once the frequency transfer function relating the input displacements to the output displacements has been found, Fig. 4.2 and the road input model can be used to obtain the output accelerations, velocities and displacements.

4.2.5 Generation of Random Road Signals for Simulation

A dynamic simulation of the vehicle was developed as a means to investigate the behaviour of the system in the time domain. For this simulation, generating a representative road elevation input for the vehicle was the most challenging problem. Since only the longitudinal dynamics of the vehicle were to be modelled, only a single track of the road was required. This is a simpler process than generating correctly correlated signals for the left and right tracks.

The random road signals are generated using the elevation PSD models. All of the statistical assumptions made about the road in defining the roughness models are applied when generating the signal. There are two approaches which can be used to generate a random signal with prescribed statistical properties: The first involves filtering white noise to produce a signal with the same spectral properties as the road model. The second is to perform an inverse Fourier transform using the definition of the PSD. to generate a number of sinusoids which are summed at random phases to produce the desired output.

There are two main problems with the former method. Firstly, the split power type cannot be generated by linear shape filters [*41*]. Since the split power type has been chosen for the representative road models, this would require more complex filters to be developed. Secondly, it was found that smooth and differentiable inputs performed better in the SIMULINK models than the discontinuous signal generated by white noise. Discontinuous signals resulted in larger discrepancies between the outputs found using transfer function blocks and that found with a block diagram. Therefore, the second method was chosen for generating the road signals.

Several approaches to the inverse Fourier transform were found in the literature. The most widely referenced approach was presented by Shinozuka [*42*]. The series used to generate the signal is given below in equation 4.2.

$$z_r(t) = \sigma\left(\frac{2}{N}\right)\sum_{n=1}^{N} cos(\omega_n t + \varphi_n) \qquad \textit{Ref [42]} \quad \textit{Eq. 4.2}$$

Where:

$$\sigma = \sqrt{\int_{-\infty}^{\infty} G_{z_r}(\Omega)d\Omega}$$

In this formulation, σ is the standard deviation of the road signal. ω_n and φ_n are random variables where φ_n is a uniformly distributed phase shift. ω_n is the frequency of each component of the series and is identically distributed with the density function obtained by normalising the spectral density function of the road with its mean square value.

The implementation of this road generation series itself requires a set of correctly distributed random numbers. This was undesirable since it would require the use of another random signal generator, again requiring complicated shape filters to generate the split power type of road model. For this reason a variation of this method was developed using the definition of the PSD function more directly.

In this method, the PSD plot is divided into a number of contiguous frequency bands. Each of these bands is then used to generate a harmonic component of the road signal. The harmonic components are sinusoidal functions of the distance travelled, x, with the mean frequency of that band, Ω_n, and an amplitude, z_n. The amplitude is determined using the definition of the continuous PSD function. By rearranging equations A.2 and A.7 one can easily obtain the result shown in equation 4.3.

$$Z_n = \sqrt{2\int_{\Omega_n - \Delta\Omega_n/2}^{\Omega_n + \Delta\Omega_n/2} G_{z_r}(\Omega)d\Omega} \qquad \textit{Eq. 4.3}$$

Here, Z_n is the magnitude of the harmonic component, Ω_n is the mean frequency of the band whose bandwidth is $\Delta\Omega_n$ and $G_{z_r}(\Omega)$ is the continuous elevation PSD function. The phases of the harmonic components are uniformly distributed between 0 and 2π in accordance with the

previously mentioned method and those presented by several authors. Finally, the harmonics are summed to produce the random road signal as follows in equation 4.4.

$$z_r(x) = \sum_{n=1}^{N} Z_n sin\,(\Omega_n x + \varphi_n) \qquad \textit{Eq. 4.4}$$

Using this method, it can be seen that the number of harmonic components used does not affect the statistical properties of the generated signal as long as the entire PSD is used in creating the signal. Over an infinite length of road, the mean of the sinusoidal harmonic components and their sum are zero. The harmonics each have Gaussian distributions and, therefore, the summed signal is also Gaussian. Further, the sum of the integrals for obtaining the mean square value of each component is equal to the integral for obtaining the mean square of the entire signal. This means the mean square is also preserved. The number of harmonics (N) used to generate a road is therefore not constrained by the basic statistical properties of the generated signal. Instead, practical and computational issues are the limiting factors. Owing to the large bandwidth of the road signal and the fact that the majority of the power of the signal lies in the low frequency range, linearly distributing the harmonic components of the signal is undesirable. Instead a logarithmic distribution of the harmonics was used.

Since different forms of the PSD function may be used, it was not suitable to determine an exact form of the integral in equation 4.3. A basic numerical integration was implemented using a simple trapezoidal rule. More elegant forms of integration may be used to speed up the simulation and to minimize errors, however, the approximate nature of the simulation and the speed of the simulation did not necessitate any improvement for the current work.

4.2.6 Note on Obtaining Roll Inputs

A brief mention is made here regarding the roll input from the road to the vehicle. To investigate the roll behaviour of a vehicle the spectral properties of the difference between the left and right tracks are required. Dodds and Robson [*37*] describe how the cross track spectral density can be obtained from the PSD function of the road. This is achieved by multiplying the single track PSD function with a coherency function which takes into account the track of the vehicle. Although this is not difficult to implement it has not been carried out due to the limited scope of this work.

4.3 Vehicle Ride Models

The desired output of the vehicle modelling is the response of the overall vehicle to the road input. This can then be translated to dynamics of the test aircraft attached to the vehicle. The process requires that a vibration model of the vehicle be developed from which frequency transfer functions are calculated for the various desired outputs. These are then used to obtain the spectral data of the output from the road models. The same models were also used to create dynamic models in SIMULINK, allowing a time domain response to be simulated.

Established vibration models of vehicles were derived from first principles. The accelerations and motions are described in a vehicle-fixed coordinate system which is conventionally defined with the positive z-axis, z^v, pointing downward as in Fig. 4.5.

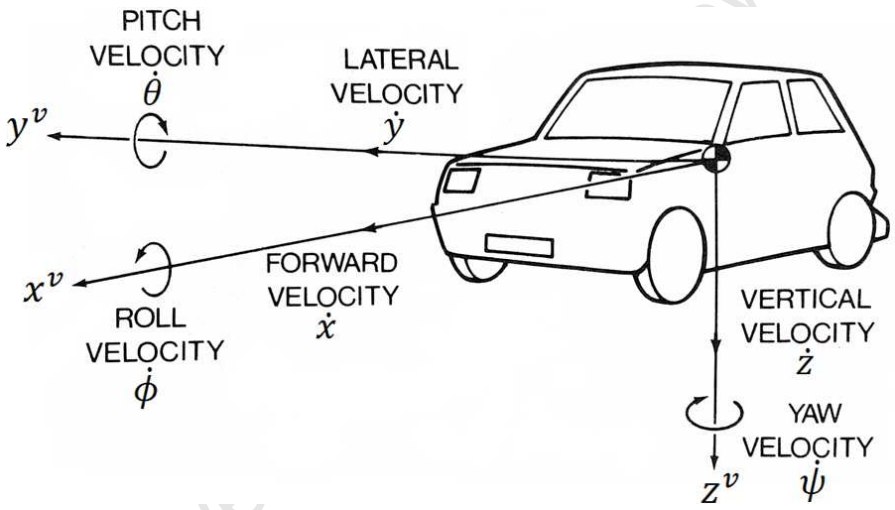

Fig 4.5: Vehicle fixed axis system [modified image from Wong [*43*]].

Two linear vibration models for the vehicle were developed: A pitch-bounce model was used to provide all of the longitudinal outputs for the vehicle, and to note other effects such as wheelbase filtering. A quarter car model, which includes the effect of the unsprung masses at the wheels, was also created to reveal the wheel hop frequency and hence show where the pitch bounce model may be inaccurate.

In the following subsections the approximations made for the ride models are discussed before each is presented. For each, a diagram of the models is given in which the axis systems are defined. The parameters in the models are named and the frequency transfer functions for each are given. Block diagrams used to generate the SIMULINK models are also shown.

4.3.1 Approximations Made in Vehicle Ride Models

The models are assumed to be linear and time invariant (LTI) since more detailed modelling is unnecessary for this feasibility study. For this reason, the models used here are basic approximations which are commonly used in ride studies. The assumptions are consistent with those made in the literature. The following important approximations have been made:

- The vehicle chassis and drive train form a perfectly rigid body.

The vehicle chassis and drive train have been assumed to be a single rigid body. The effect of passengers has also been ignored. These assumptions will affect the accuracy of the vibration response obtained. However, since detailed specifications of the vehicle and aircraft are unknown at this stage, more accurate models would be inappropriate.

- Tyres are stiff, linear springs with no damping and make point contact with the road.

Tyres are known to be non-linear and produce different load-deflection curves depending on the tyre type, inflation pressure and on whether the tyre is static or rolling [*31*]. Wheel and tyre imbalance and the harmonic modes of the tyres have been ignored in these models. The effect of the radius of the tyre in filtering out small variations in the road surface has also not been taken into account. Tyre damping has been ignored in the quarter car model and the tyres are treated as stiff linear springs which make point contact with the road.

- Shock absorbers are viscous dampers with the same damping coefficient in the jounce and rebound directions

Modern shock absorbers have different damping performance in the compression (jounce) and extension (rebound) directions [*35*]. The ratio between the rebound and jounce directions is typically in the region of three-to-one. The damping force is assumed to be proportional to the velocity, though there is some variation from this in real shock absorbers. The performance of the shocks also deteriorates with time. The dampers in the models that follow have been assumed to be ideal viscous dampers with no bump stops or end rubbers.

- The suspension springs are perfectly linear

A linear spring rate has been assumed for the ride models. It is known that springs do not behave linearly at high speeds and with high frequency vibrations. It is therefore accepted that at high frequencies the results of the model may be unrealistic. No special considerations have been made for leaf springs which are often fitted to the rear of light commercial vehicles.

4.3.2 Quarter Car Model

This simple model is used in vehicle ride studies to investigate the effect of the unsprung mass on the ride behaviour of the vehicle. The model is referred to as the quarter car model as it appears to represent only one wheel with a sprung mass above. For approximate models of the bounce behaviour of a vehicle, the unsprung masses may be combined into a single mass and the total vehicle mass to the sprung mass. In order to investigate the hop frequency of the unsprung mass, as is desired here, the sprung mass can be divided according to the weight distribution at each wheel. The model is defined below in Fig. 4.6.

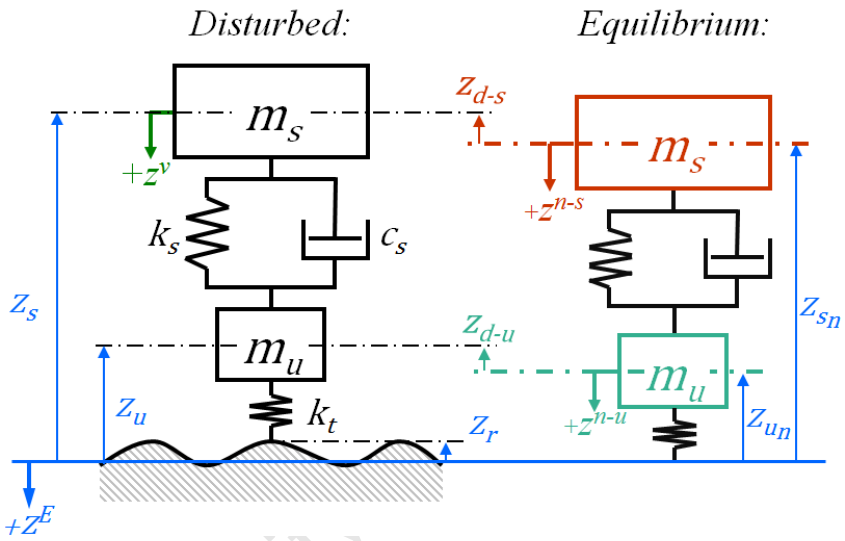

Fig 4.6: Quarter car model definition.

In the figure, the earth axis, $+z^E$, and the vertical vehicle fixed axis, $+z^v$, are defined. For the vibration analysis, the neutral equilibrium axes for the sprung and unsprung masses are defined as $+z^{n-s}$ and $+z^{n-u}$ respectively. Note that in the figure all the displacements shown are negative in their axis systems and are all functions of time. In table 4.1 the parameters used in the model are defined.

Table 4.1: Definition of quarter car model parameters.

Symbol	Description	Units
m_s	Sprung Mass	kg
m_u	Unsprung Mass	kg
k_s	Suspension Spring Constant	N/m
c_s	Suspension Damping Coefficient	$N/m/s$
k_t	Tyre Spring Constant	N/m

Using Newton's laws and applying Laplace transforms for LTI systems, two frequency transfer functions were derived for the above system. This is shown in detail in appendix C. These relate the road displacement input to the displacements of the unsprung and sprung masses. The frequency transfer functions, $H_{u/r}(j\omega)$ relating the road input to the unsprung mass and $H_{s/r}(j\omega)$ relating the road input to the sprung mass, are repeated below in equations C.11 and C.12.

$$H_{u/r}(j\omega) = \frac{z_{d-u}(j\omega)}{z_r(j\omega)} = \frac{m_s k_t (j\omega)^2 + c_s k_t (j\omega) + k_s k_t}{m_u m_s (j\omega)^4 + (m_u + m_s) c_s (j\omega)^3 + [(m_u + m_s)k_s + m_s k_t](j\omega)^2 + c_s k_t (j\omega) + k_s k_t} \quad \textit{Eq. C.11}$$

$$H_{s/r}(j\omega) = \frac{z_{d-s}(j\omega)}{z_r(j\omega)} = \frac{c_s k_t (j\omega) + k_s k_t}{m_u m_s (j\omega)^4 + (m_u + m_s) c_s (j\omega)^3 + [(m_u + m_s)k_s + m_s k_t](j\omega)^2 + c_s k_t (j\omega) + k_s k_t} \quad \textit{Eq. C.12}$$

Further, a block diagram of the system was drawn to assist with the development of the SIMULINK model. This is shown in Fig. 4.7. The actual SIMULINK models are presented in appendix D.

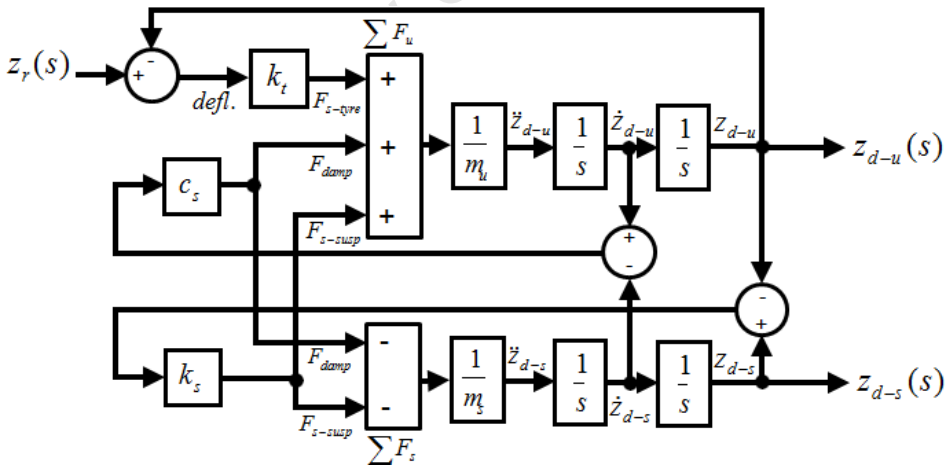

Fig 4.7: Block diagram for quarter car model.

4.3.3 Pitch Bounce Model

In order to investigate the pitching response of a vehicle, a model excluding the unsprung masses was used. Although a simpler model excluding the dampers is often used to note the important pitch dynamics of a vehicle, this model performs more realistically in the time domain simulation. Pitch response is particularly important to this work as the angle of attack

of the aircraft is the main variable determining in the longitudinal dynamics of the aircraft. The model is defined in Fig. 4.8.

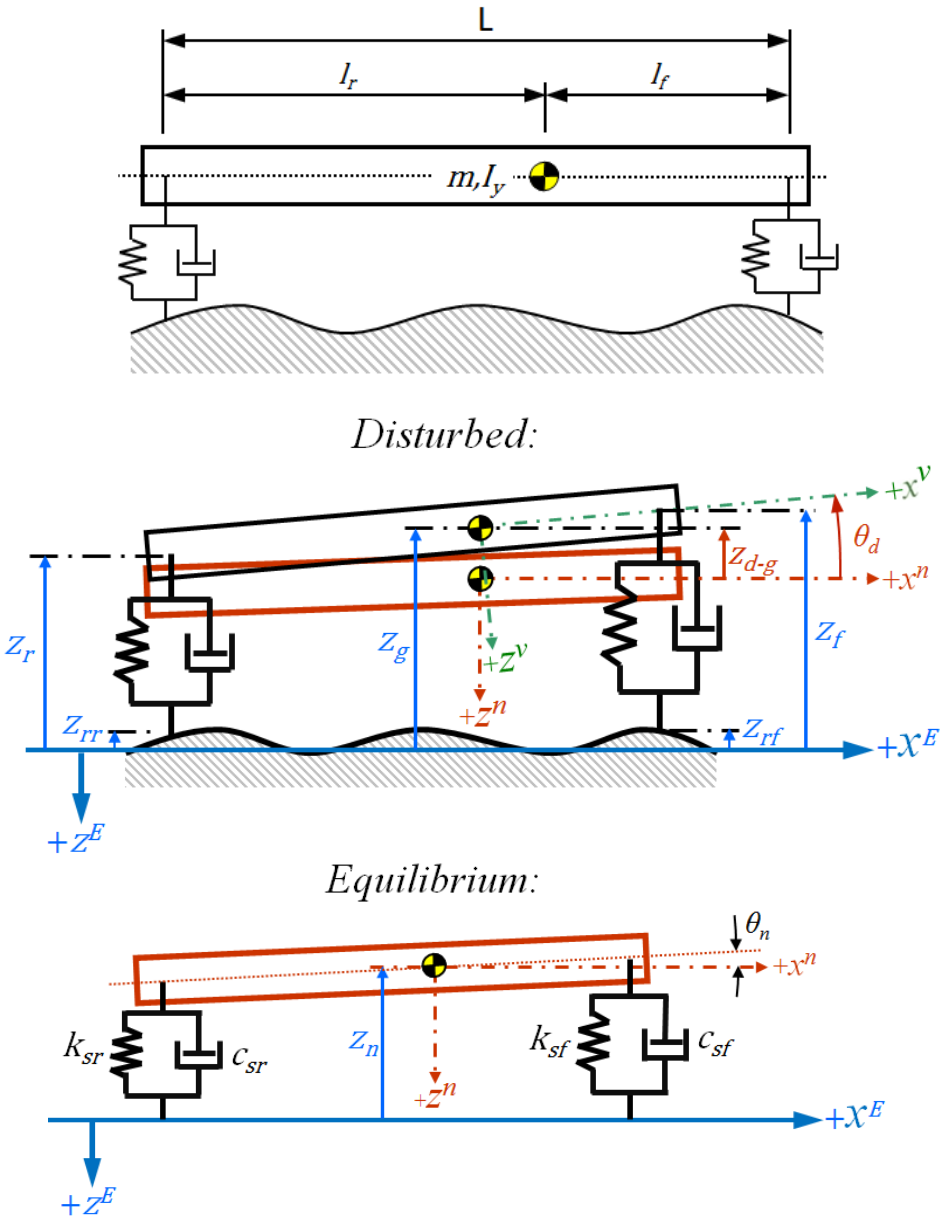

Fig 4.8: Definitions of the pitch bounce model.

The vehicle fixed axis system, $\langle x^v, z^v \rangle$, and earth fixed axis system, $\langle x^E, z^E \rangle$, are defined above. The equilibrium axes, $\langle x^n, z^n \rangle$, are defined showing a small angular difference, θ_n, between them and the centreline of the body. This angle is included to indicate that the equilibrium pitch angle of the vehicle will change. In this work, however, the angle has been assumed to be zero but is noted as potentially significant.

Table 4.2: Definition of pitch bounce model parameters.

Symbol	Description	Units
$\boldsymbol{m}$	Vehicle Mass	kg
$\boldsymbol{I_y}$	Pitch Moment of Inertia	$kg.m^2$
$\boldsymbol{k_{sf}}$	Front Suspension Spring Constant	N/m
$\boldsymbol{c_{sf}}$	Front Suspension Damping Coefficient	$N/m/s$
$\boldsymbol{k_{sr}}$	Rear Suspension Spring Constant	N/m
$\boldsymbol{c_{sr}}$	Rear Suspension Damping Coefficient	$N/m/s$
$\boldsymbol{L}$	Wheelbase	m
$\boldsymbol{l_f}$	Distance from c.g. to Front Wheels	m
$\boldsymbol{l_r}$	Distance from c.g. to Rear Wheels	m

Again applying Laplace transforms for LTI systems to equations derived from Newton's laws for the bounce and pitch motions, two frequency transfer functions were obtained. The two frequency transfer functions relate the road displacement input to the pitch and bounce displacements. The results of the derivations shown in appendix C are repeated in equations C.23 and C24 below. Coefficients A through U are calculated from the parameters of the system and are given in the appendix.

$$\frac{z_{d-g}(j\omega)}{z_r(j\omega)} = H_{z/r}(j\omega)$$

$$= \frac{F(j\omega)^3+G(j\omega)^2+H(j\omega)+I}{A(j\omega)^4+B(j\omega)^3+C(j\omega)^2+D(j\omega)+E} + e^{-\tau(j\omega)}\left(\frac{N(j\omega)^3+O(j\omega)^2+P(j\omega)+Q}{A(j\omega)^4+B(j\omega)^3+C(j\omega)^2+D(j\omega)+E}\right) \quad \textit{Eq. C.23}$$

$$H_{\theta/r}(j\omega) = \frac{\theta_d(j\omega)}{z_r(j\omega)}$$

$$= \frac{J(j\omega)^3+K(j\omega)^2+L(j\omega)+M}{A(j\omega)^4+B(j\omega)^3+C(j\omega)^2+D(j\omega)+E} + e^{-\tau(j\omega)}\left(\frac{R(j\omega)^3+S(j\omega)^2+T(j\omega)+U}{A(j\omega)^4+B(j\omega)^3+C(j\omega)^2+D(j\omega)+E}\right) \quad \textit{Eq. C.24}$$

In the model, the elevation profile is first passed over by the front wheels and then the rear with a time delay, τ, determined by the wheelbase, L, and vehicle speed, V. This results in the time delay in the frequency transfer functions.

Also of interest are the accelerations at a point, A, away from the c.g., indicating the position of the aircraft. The acceleration at a, $\vec{a}_A$, is made up of three vector components shown in Fig. 4.9 below.

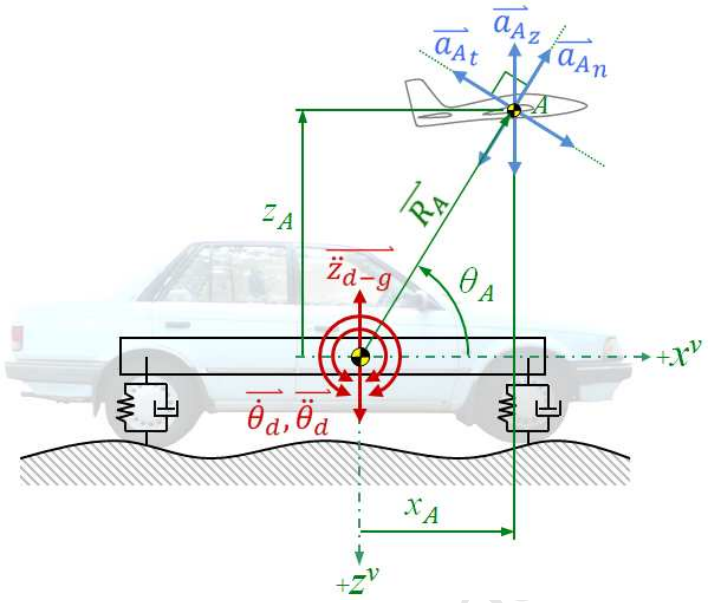

Fig 4.9: Components of aircraft acceleration due to ride motion.

The accelerations of the aircraft are related to the accelerations of the vehicle according to equation 4.5.

$$\overrightarrow{a_A} = \underbrace{\overrightarrow{a_{A_z}}}_{\overrightarrow{\ddot{z}_{d-g}}} + \underbrace{\overrightarrow{a_{A_n}}}_{\overrightarrow{\dot{\theta}_d}\times\left(\overrightarrow{\dot{\theta}_d}\times\overrightarrow{R_A}\right)} + \underbrace{\overrightarrow{a_{A_t}}}_{\overrightarrow{\ddot{\theta}_d}\times\overrightarrow{R_A}} \qquad \textit{Eq. 4.5}$$

However, since the pitch velocity of a vehicle, $\dot{\theta}_d$, will be very small, the normal component of the acceleration, $\overrightarrow{a_{A_n}}$, will be insignificant. Two important observations can be made from this. The first is that reducing the distance from the c.g of the vehicle to the aircraft will reduce the tangential component of the acceleration. Secondly, it is noted that if one wished to minimize the vector sum of the acceleration components, one should place the aircraft vertically above the centre of gravity.

A block diagram was also drawn for the system in order to aid the SIMULINK modelling. This is shown in Fig. 4.10. Included in the block diagram are outputs for the acceleration components of the aircraft location. Refer to appendix D for the implementation of this block diagram in SIMULINK.

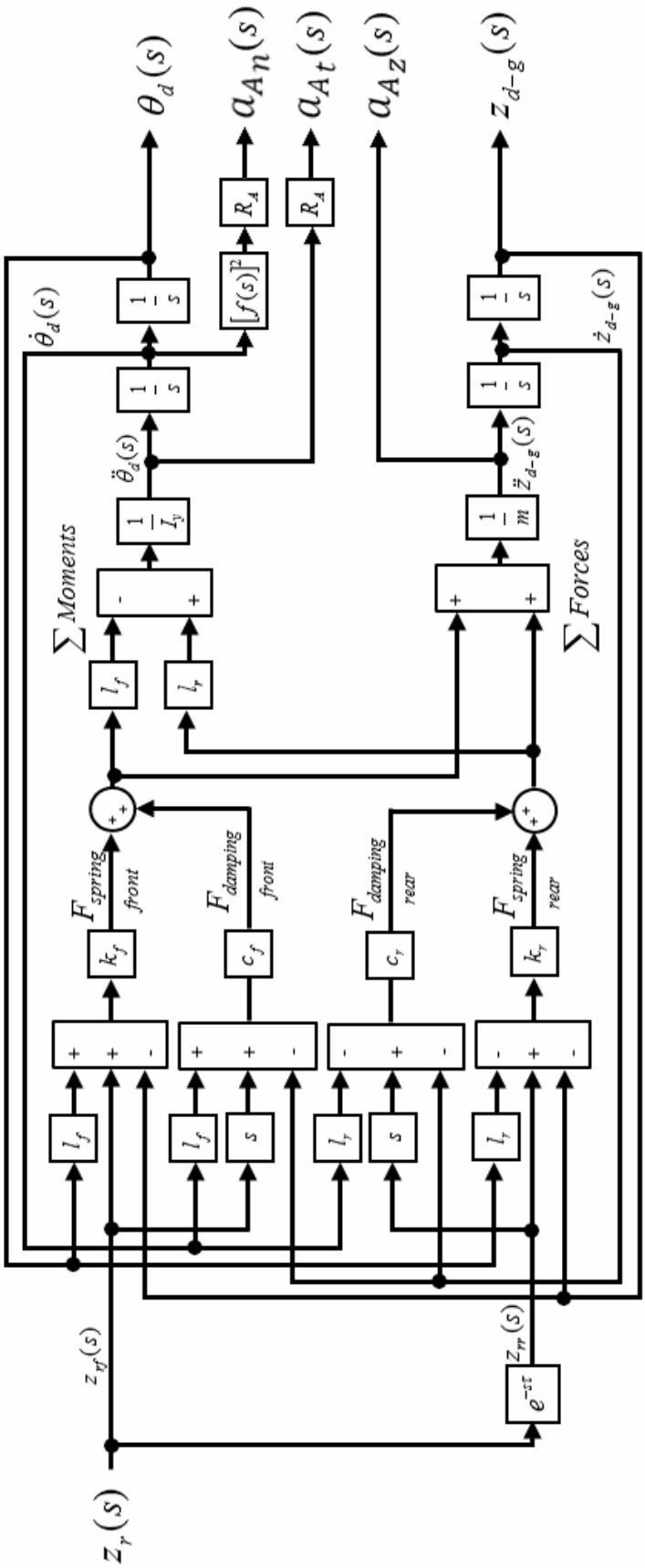

Fig 4.10: Block diagram for pitch-bounce model.

4.4 Results from Ride Modelling

With the theory behind the ride modelling laid out, the results from the modelling are now presented. The results below were generated for only one vehicle described by parameters presented in the first subsection. Additionally, only the benchmark road models were used to obtain the outputs. However, the code used to generate these results is capable of modelling vehicles with other parameters and any of the road roughness models shown in appendix B can be selected.

4.4.1 Inputs for Ride Modelling

The kind of detailed parameters required to perform ride modelling on vehicles is not easily found from vehicle manufacturers. Instead of using a benchmark vehicle model, such as that used in the operating cost calculations, parameters quoted by J. Marzbanrad et al. [*44*] were used. The parameters are presented in table 4.3.

Table 4.2: Definition of pitch bounce model parameters

Symbol	Description	Value	Units
m	Total Vehicle Mass	1460	kg
m_s	Sprung Mass: Per Front Wheel Per Rear Wheel	467.5 262.5	kg
m_u	Unsprung mass: Front Wheels Rear Wheels	40 35.5	kg
I_y	Pitch Moment of Inertia	2460	$kg.m^2$
k_{sf}	Front Suspension Spring Constant (Single Wheel)	19960	N/m
c_{sf}	Front Suspension Damping Coefficient (Single Wheel)	1290	$N/m/s$
k_{sr}	Rear Suspension Spring Constant (Single Wheel)	17500	N/m
c_{sr}	Rear Suspension Damping Coefficient (Single Wheel)	1620	$N/m/s$
k_t	Tyre Spring Constant	175500	N/m
L	Wheelbase	2.814	m
l_f	Distance from c.g. to Front Wheels	1.011	m
l_r	Distance from c.g. to Rear Wheels	1.803	m

These values are used to generate all the results that follow. The sprung masses used for the front and rear wheels were 467.5 kg and 262.5 kg respectively, split according to the weight distribution between the front and rear wheels and assuming a 50/50 weight distribution

between the left and right tracks. It is noted that the parameters of actual vehicles will cause significantly different ride behaviour. The parameters also will be affected by the addition of the apparatus. The parameters such as the mass and pitching moment of inertia may also be purposefully changed to improve the vehicle ride.

4.4.2 PSD Curves of Ride Outputs

The PSD curves obtained from modelling are presented here and important features of the curves are discussed. For each plot the gain obtained for the ride model is presented along with the calculated output using the three benchmark road curves.

First modelled are the outputs for the quarter car model. Two sets of responses were calculated, one for the front wheels and one for the faster rear wheels. The front and rear wheels in vehicles are tuned to have different natural frequencies which allow the vehicle to exhibit 'flat ride' where the pitching motion of the vehicle is minimised. The displacement responses are shown in Fig. 4.11 and 4.12.

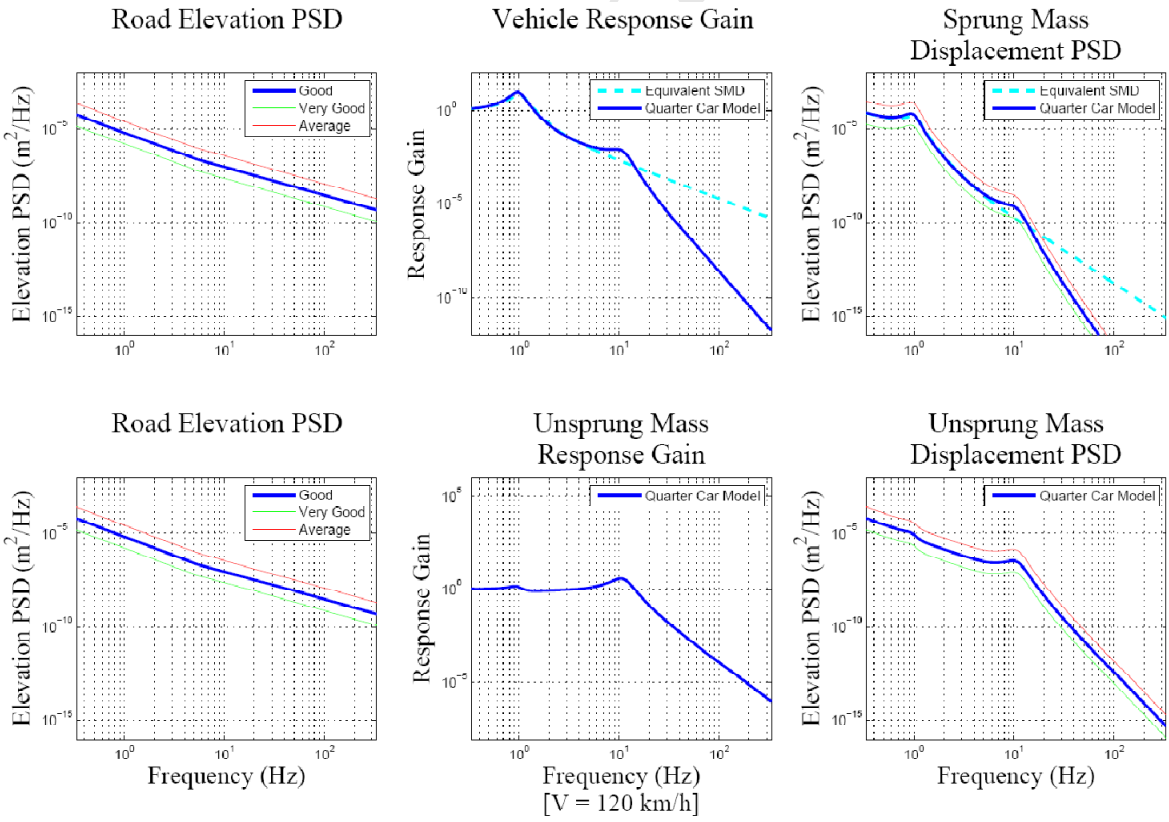

Fig 4.11: Quarter car model displacement outputs for front wheels

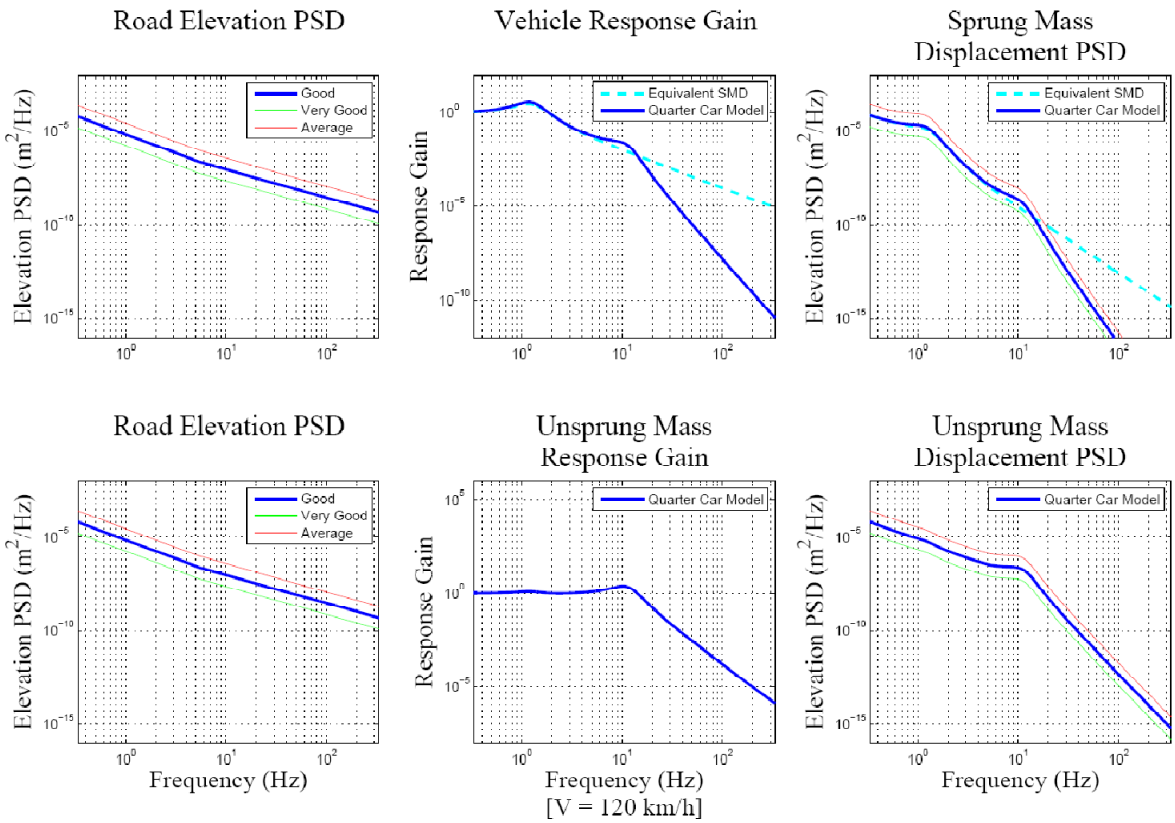

Fig 4.12: Quarter car model displacement outputs for rear wheels

In the figures above, the responses of equivalent spring-mass-damper (SMD) systems (ignoring the unsprung mass and tyre spring) have been shown for comparison. The differences are important to note as the pitch-bounce model does not include the effect of the unsprung mass on the ride. At low frequencies, the gains for both the SMD and quarter car are near unity for the front and rear wheels. The resonant frequencies are both at around 1Hz with the peak gain of the rear wheels being lower and at a slightly higher frequency.

The main differences which can be identified are the wheel hop frequencies, which are the second peaks visible in the curves. These are where the unsprung mass is resonating causing an increase in the gain over the SMD system. Also, the gain of the quarter car model drops off more rapidly than the SMD system, causing a significant difference in the gains at high frequencies (approximately five orders of magnitude difference in response gain). It is therefore important to note that the pitch-bounce model will significantly exaggerate the displacements at high frequencies and will predict higher accelerations as seen in Fig. 4.13.

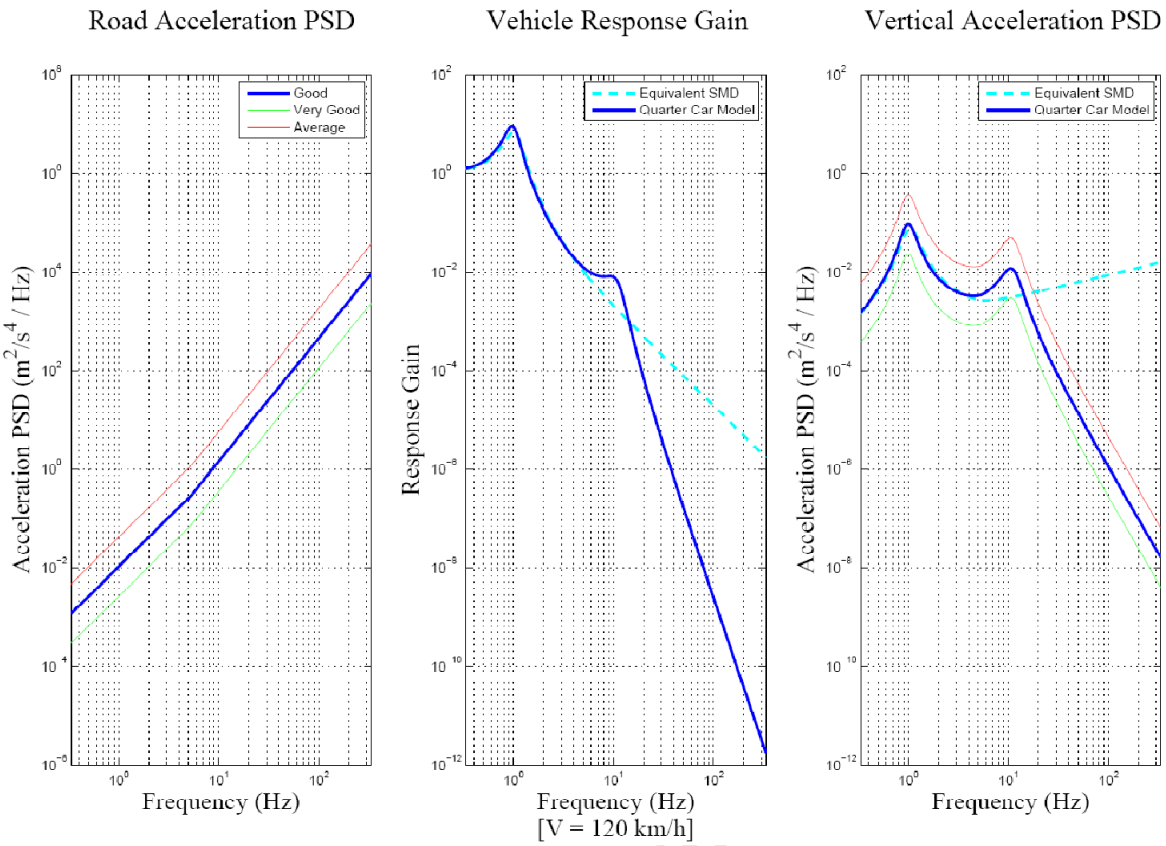

Fig 4.13: Quarter car model acceleration output for front wheels

It is important to note that the curve above was calculated for a high speed of 120km/h which may not be necessary for testing. Note that at the upper limit of the frequency band, there is a large difference between the gain predicted by the models.

Noting the shortcomings uncovered in the analysis of the quarter car model, the pitch-bounce model was studied with some scepticism for the results at high frequencies. The parameters for the model are as per table 4.2. However, the suspension damping and spring coefficients have been doubled since the pitch bounce model essentially assumes a vehicle with zero track. Figure 4.14 shows the pitch and bounce gains with predicted outputs for the displacements of the vehicle. The equivalent SMD system in the figures below essentially assumes a zero wheelbase and track. The spring constants and damping coefficients are added together.

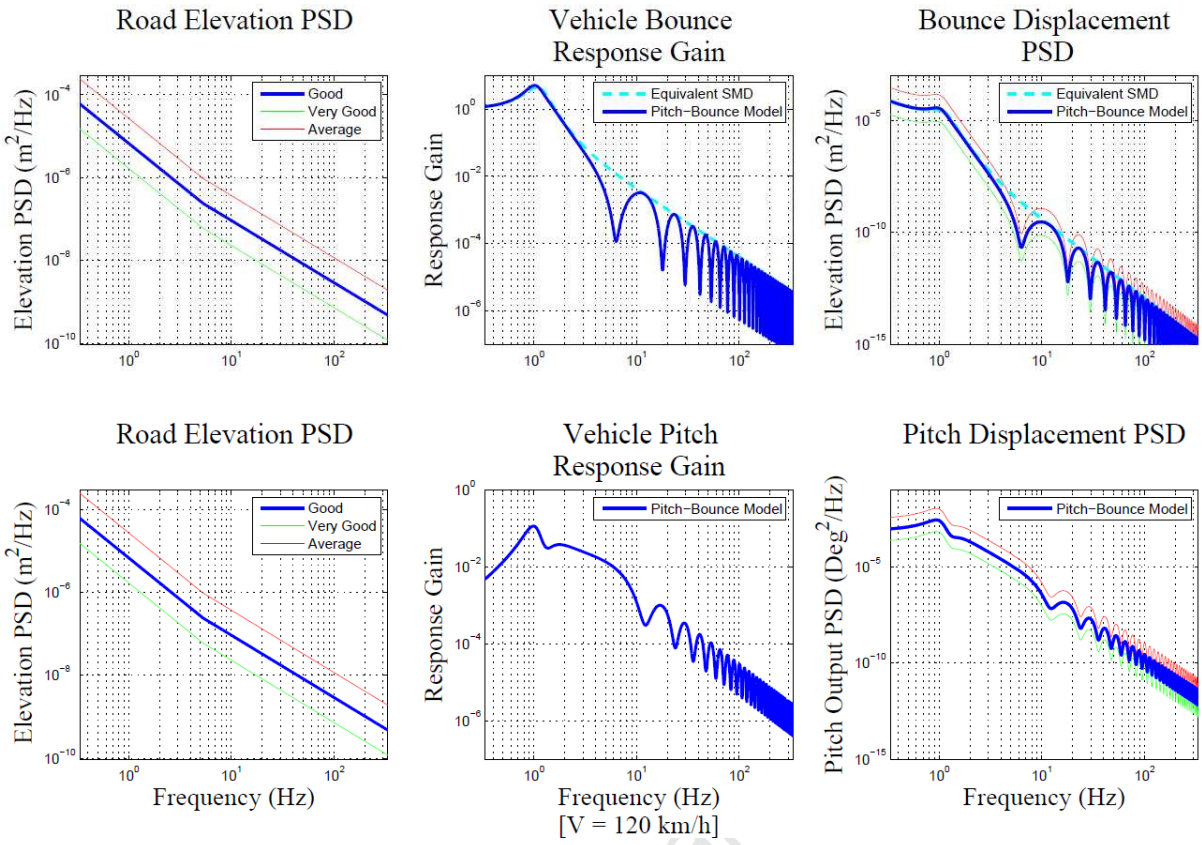

Fig 4.14: Pitch-bounce model displacement outputs

Interesting features to note in the response gain curves are the periodic drops in gain falling away from the gain for the SMD system, which forms an upper boundary to the bounce gain. The dips are caused by a phenomenon called wheelbase filtering. When a vehicle is passing over disturbances where the wavelength is such that while one wheel is on a crest, the other is in a dip, the vehicle is being made to pitch more than it is made to bounce. If the wheels are both on crests, the vehicle is being made to bounce, and not pitch. This explains why the dips in the bounce gain are in between the dips in the pitch gain, and it explains why there are multiple dips occurring each time the wavelength of the road signal is a multiple of the wheelbase.

The quickly oscillating nature of the gain at high frequencies also suggests there may be some unrealistic responses to the random road generated for the model, as the random road lumps parts of the road PSD into windows with a single frequency which may correspond to a response gain anywhere between the upper and lower limits of the response gain in that band. Figure 4.15 shows the acceleration responses.

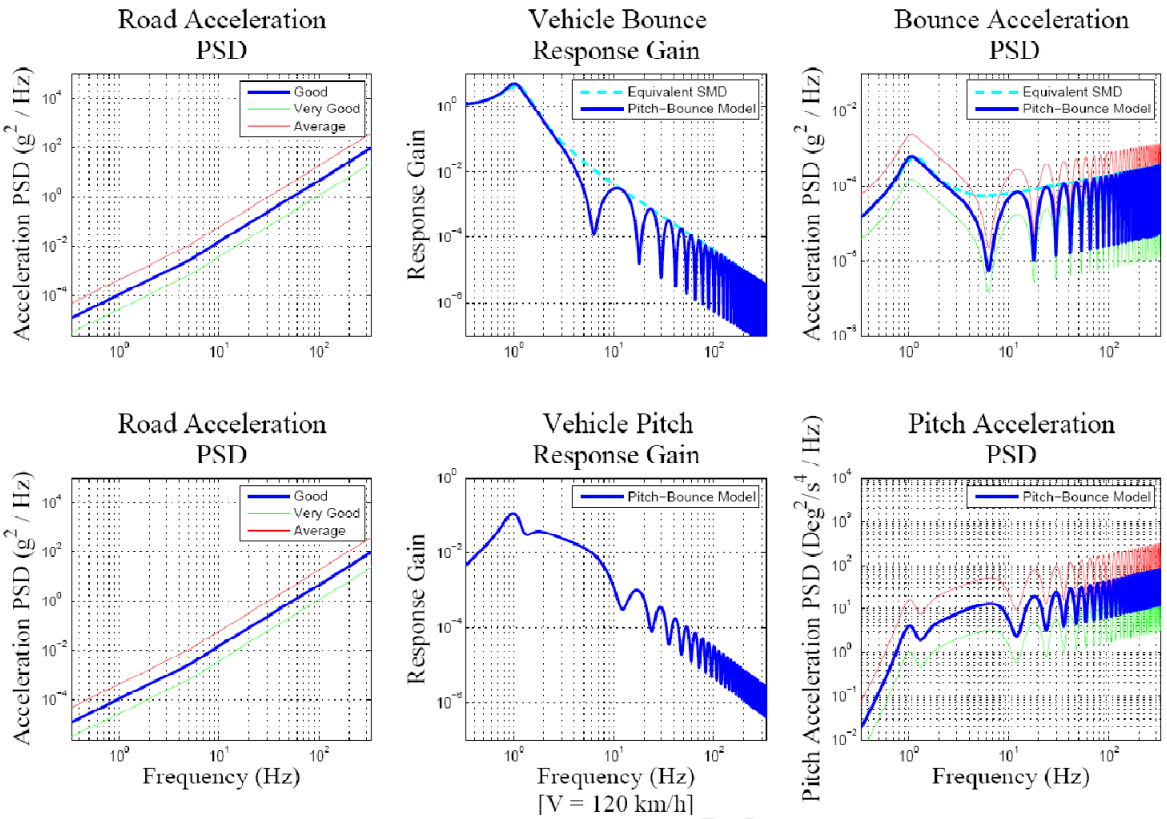

Fig 4.15: Pitch-bounce model acceleration outputs

Note again that the acceleration tends to increase at higher frequencies, which does not occur when the unsprung masses are taken into account in the quarter car model.

4.4.3 Simulation Outputs

The spectral data obtained in the previous subsection is useful for identifying some of the vibration phenomena, for identifying the short-falls of the vibration models and for noting the effect of various parameters on the gain of the system. However, in order to get a feeling for the outputs of the system in the time domain, the system was modelled in the time domain.

First it was necessary to check the validity of the random road generator. The statistics of the road inputs were checked in order to see how effective the implementation was. It is known that the road signal must have zero mean and have a Gaussian distribution. In this case, the variance is equal to the mean square and must be equal to mean square obtained for the road model by integrating the PSD over the bandwidth. It can be seen in Fig. 4.16 that there was good agreement between the theoretical normal distribution calculated from the road model, and the normalised histogram of the generated road signal. This was true for any road model selected but the figure shows only the ‘good’ road from the chosen benchmark models. This model has been used for all of the simulation outputs shown in the remainder of this chapter.

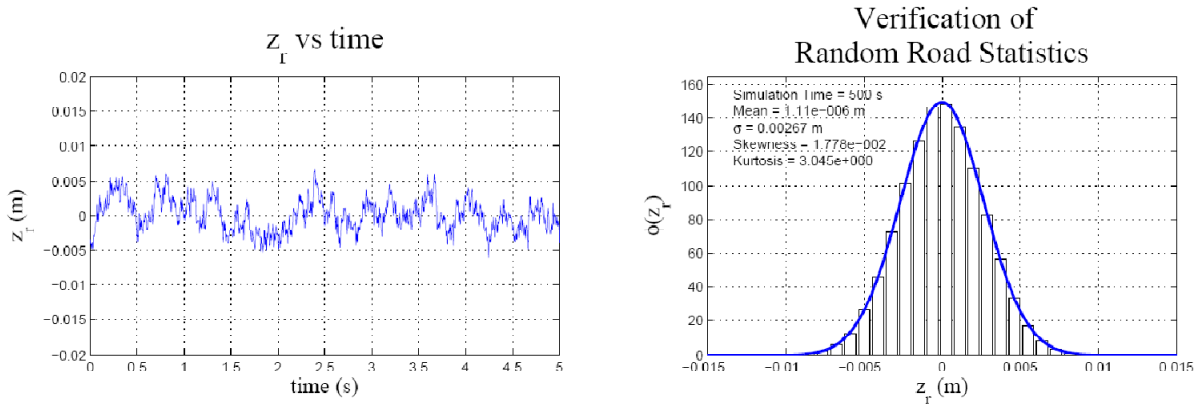

Fig 4.16: Verification of random road generator.

As long as the simulation was run for an appropriate length of time (>200 seconds), the errors in the mean and variance were insignificantly small. For example, the error in the variance for the above data was less than 0.03%. The skewness and kurtosis were also acceptable, though the skewness was significant in shorter simulations. Even though this method of generating the road makes use of only 100 harmonics, with fewer high frequency components than low, the shortfalls in the fidelity of the high frequency components is acceptable. This is because the vehicle models used are known to be inaccurate at these frequencies.

With the road input being deemed satisfactory, the simulations using the two ride models could be conducted. The quarter car model was used for comparison to note the differences incurred by ignoring the unsprung masses in the pitch-bounce model. The figures that follow show a limited period of the time domain signal shown followed by histograms showing the probability density functions and basic statistics of the outputs.

It should be noted that the normal Gaussian distribution curves shown on the histograms are calculated using the mean and variance determined from the random data generated, and not by integrating the output response curves as was done in verifying the road generator. The curves are intended to show that the data exhibit normal distributions. The outputs are all generated at a speed of 120km/h and use the parameters described in chapter 4. The simulation time is 500 seconds with the gain of the road signal smoothly increased from 0 to 1 over the first 3 seconds.

In Fig. 4.17, the time domain outputs for the quarter car model, using the parameters for the front wheels, are shown. From top to bottom, the plots show the road input, the displacement of the unsprung mass and sprung mass followed by the acceleration of the sprung mass.

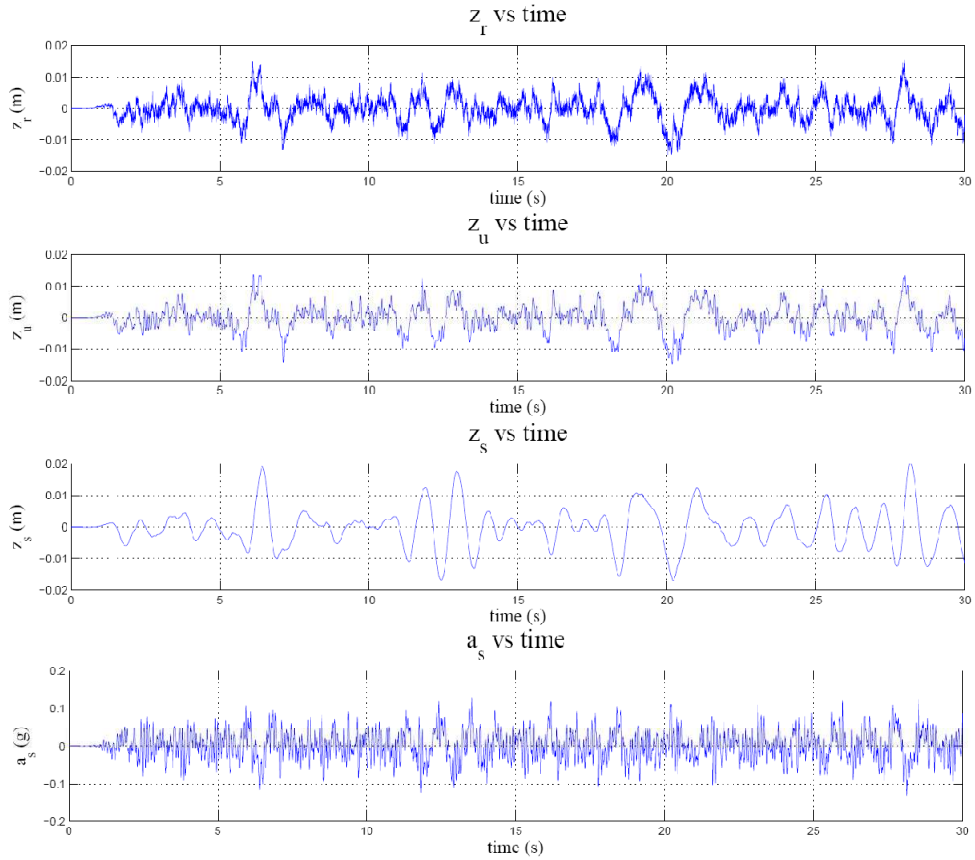

Fig 4.17: Time domain outputs for the quarter car model (front wheels)

It can be noticed that the displacement of the unsprung mass closely follows the road input, with some of the high frequency displacements filtered out. The sprung mass displacement then shows even more of the higher frequencies removed. The sprung mass shows similar displacement magnitudes as the original signal but tends to overshoot the maximum displacements in some places. This is expected since the frequency response gain is greater than 1 for low frequencies. This results in the larger standard deviation shown on the histogram given in Fig. 4.18. It is noted that the vertical acceleration is promisingly small at less than 0.2g with a standard deviation of 0.0381g and seems amenable to low pass filtering and damping owing to its high frequency content.

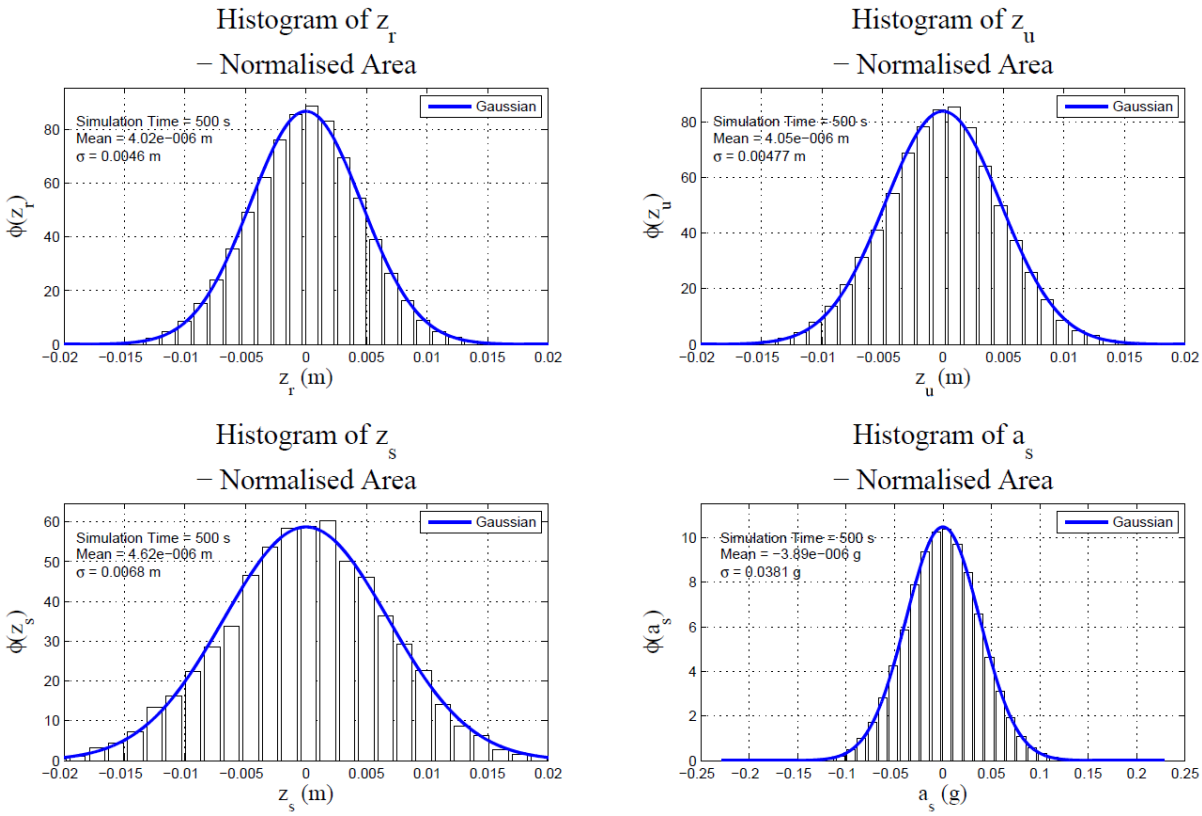

Fig 4.18: Normalised histograms of simulation outputs for the quarter car model (front wheels)

Next, the pitch bounce simulations were conducted. The displacements are shown in Fig. 4.19 followed by the accelerations in Fig. 4.20. Here again it can be seen that the high frequencies in the road signal are reduced in the vertical displacement of the vehicle. The pitch motion is also relatively smooth and remains small, within ±0.2°.

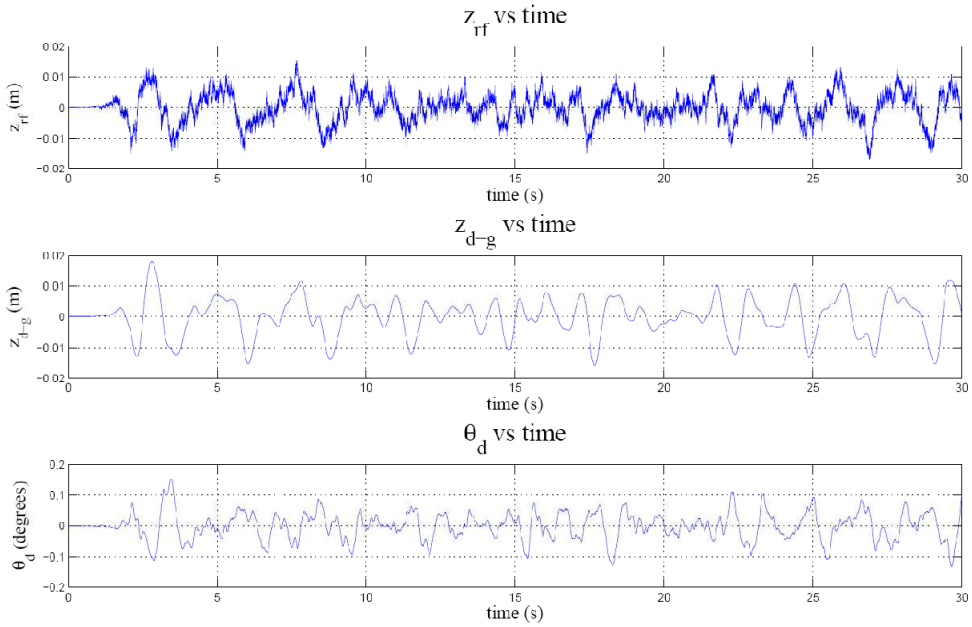

Fig 4.19: Time domain displacement outputs for the pitch bounce ride model

The acceleration outputs shown in Fig. 4.20 are more concerning. In this model, the maximum vertical accelerations are near 1g and the maximum pitching accelerations are slightly larger than 1 rev/s^2.

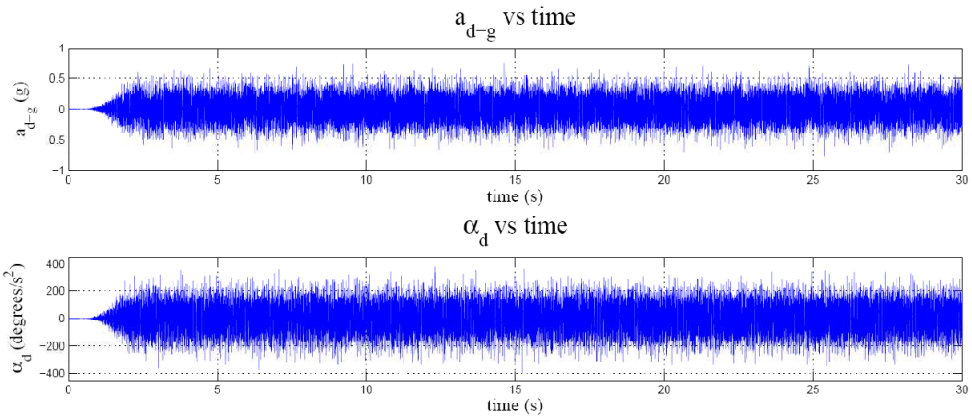

Fig 4.20: Time domain acceleration outputs for the pitch bounce ride model

It is clear, however, that the large accelerations occur at high frequencies, as is predicted by the response curves in the previous section. This is to be expected without unsprung masses and tyres in the model. The histograms in Fig. 4.21 and 4.22 show the statistics of the pitch bounce displacement and rotation outputs respectively.

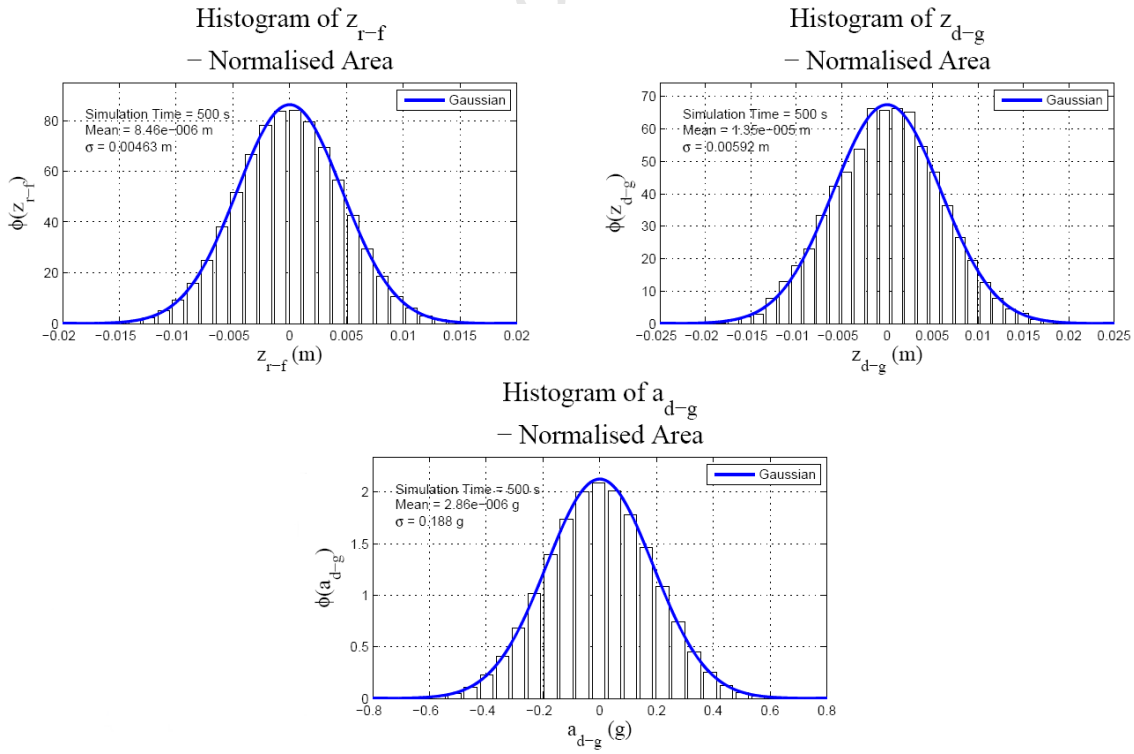

Fig 4.21: Normalised histograms of translation outputs for the pitch bounce ride model

The small standard deviations of the vertical displacement (5.92mm) and the vertical acceleration (0.188g) are noted. Comparing this to the outputs of the quarter car model suggest that the simple pitch bounce model overestimates the accelerations significantly. The standard deviation of the pitch displacement is very small at just 0.0445° while the pitch acceleration is 100deg/s^2. Again, the pitch acceleration is likely overestimated.

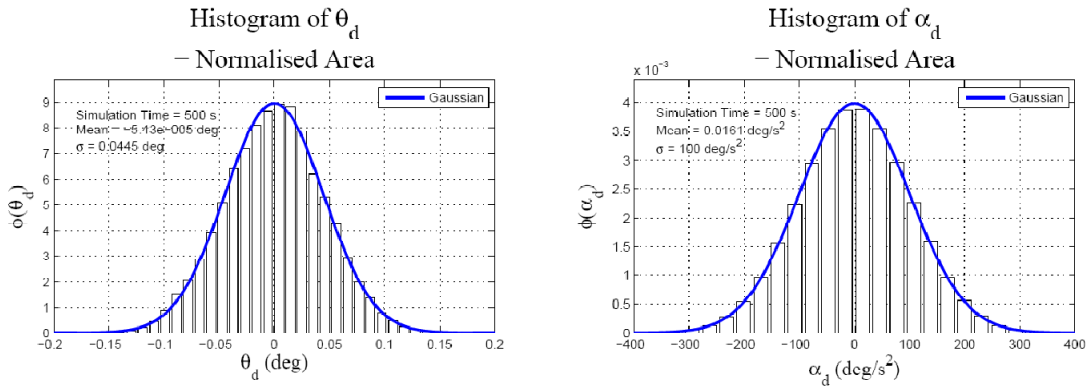

Fig 4.22: Normalised histograms of rotation outputs for the pitch bounce ride model

Finally the accelerations at a point representing the location of the aircraft, *A*, were modelled (see Fig 4.9). The total acceleration is not combined into a single vector for two reasons. First, it was already stated that the best location for the balance is vertically above the c.g. Secondly, keeping the acceleration in components is illustrative in determining the main physical effects.

The simulations were conducted with $\overrightarrow{R_A}$ set to a reasonable value of 3m. In Fig. 4.23 the time domain outputs it is noted that the tangential acceleration is greater than the vertical acceleration with a peak value just under 2g predicted. The vertical acceleration of the aircraft is obviously identical to that of the vehicle. The normal acceleration is insignificantly small owing to the very small pitch velocities achieved and can be ignored.

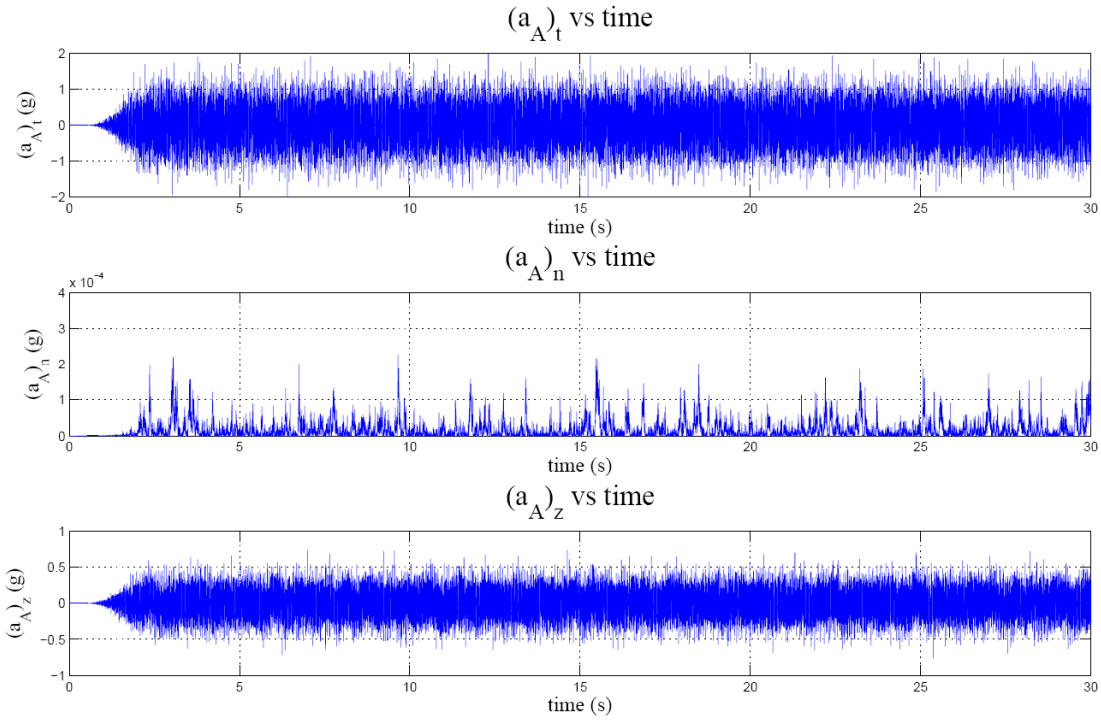

Fig 4.23: Time domain acceleration at a point, *A*, representing the aircraft position in the pitch bounce model

In Fig. 4.24 below, the standard deviation of the tangential acceleration is shown to be 0.534g compared to the 0.188g predicted in the vertical direction.

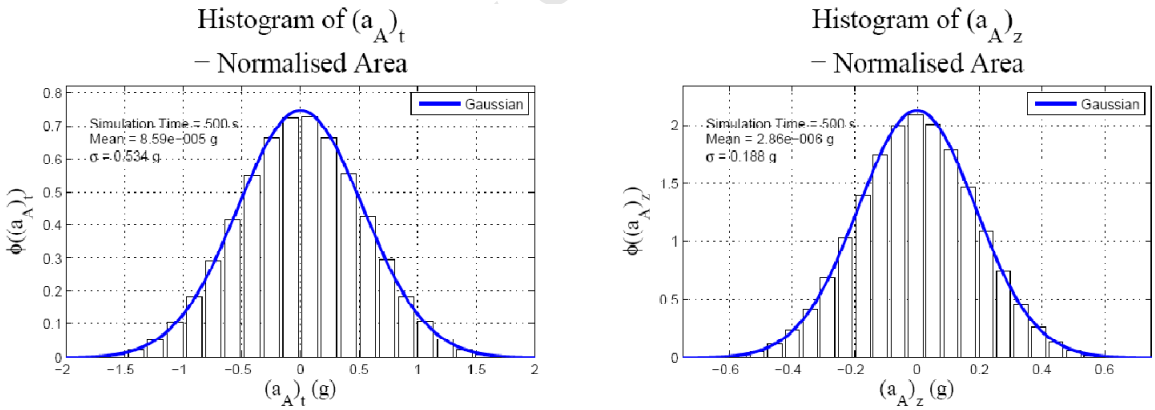

Fig 4.24: Normalised histograms of tangential and vertical accelerations at point *A*

It is again noted that there is clearly a large high frequency component transferred to the acceleration outputs using the pitch bounce model developed. It is likely that additional shock absorption between the vehicle and the testing apparatus, together with some low pass filtering on the output signals, should mitigate the accelerations predicted.

4.5 Discussion and Summary of Ride Investigation and Modelling

The modelling in this chapter was conducted with the aim of investigating the ride dynamics at a point on a road vehicle. In particular the pitch displacement and the accelerations of a point representing the location of the aircraft were desired. In the process of investigating and modelling those problems several important points have been noted which give important physical insight into the problem, and which have practical implications for the proposed apparatus.

Firstly it is important to note that real roads will not have a zero mean since they always change inclination and elevation. They may only be assumed to be stationary for limited sections of road and even these will have transient features disturbing the output data. Unless a smooth saltpan is used, such as the Hakskeen pan in the Northern Cape, the road surface will always require some data to be disregarded. Testing with the apparatus shrouded, and a dead weight on the balance, would be an ideal means to test the statistical properties of the forces resulting from ride over a real road and the methods used to filter and average the data.

The random road generator provides an excellent basis for testing the system with different layouts, models and parameters on a selection of roads. However, it is noted again that the random road generator used here has only one hundred harmonics for generating the road, limiting its fidelity at high frequencies. This could be improved through more careful programming which would produce a much improved road signal. It is also noted that sources of noise internal to the vehicle have also not been considered here.

The high frequency vibrations are clearly a concern in the modelling conducted in this chapter. The largest accelerations predicted have all been in the high frequency range where it is known that the vehicle models are inaccurate. Most of the assumptions made for the vehicle models in sub-section 4.3.1 become invalid at high frequencies. Useful information may still be obtained from the modelling, however.

The high frequency vibrations causing the large accelerations may be reduced using shock absorbers fitted between the apparatus and the vehicle. It is also possible to filter out high frequency noise using low-pass filters, however, load cells do not behave well under strong vibration. The high frequency noise also requires that the sampling of the load cells be

conducted at a very high rate which increases the cost of the sampling system. It is therefore advisable that these vibrations be mitigated as far as possible without significantly increasing the cost of the system.

Further practical considerations have been noted by studying the ride modelling. Testing at lower speeds will reduce the intensity of the vibrations experienced by the system. Slower testing speed is not a straightforward solution however, as lowering the speed decreases the magnitude of the aerodynamic forces relative to the acceleration forces. Reducing the mass of the test model is highly desirable as a means of reducing the forces resulting from the accelerations. On the other hand increasing the mass and pitch inertia of the vehicle is more desirable for reducing the accelerations of the vehicle.

Finally, placing the aircraft vertically above the vehicle c.g. and reducing the distance between the c.g. of the aircraft and the vehicle is also a desirable means of reducing the accelerations and forces. This is complicated by the influence of the road vehicle on the aerodynamics of the system. It is for this reason that the next chapter focuses on developing an understanding of the flow field around a ground vehicle.

5 Vehicle Aerodynamics

The focus is now shifted to the second major physical problem facing a vehicle mounted aerodynamic testing apparatus. This is the effect of the vehicle on the flow over the test aircraft. The flow around a road vehicle is very complex. In front of the vehicle the air is deflected vertically and horizontally around the fore body, with a portion of the flow passing though the engine bay and into the vehicle interior. At the rear there are regions of flow separation, vortex formations, turbulent flow and possible unsteady vortex shedding.

This chapter begins with a qualitative investigation into the external aerodynamics of road vehicles. Overall flow features common to appropriate passenger and commercial vehicles have been described. Beyond this it was desirable to model the airflow over a vehicle in order to approximate the deflection of the airflow over a representation of the test aircraft. Potential flow methods were used for aerodynamic modelling after their applicability and limitations were identified.

A 2D, surface-source code developed by the author for a separate project was initially used to gain some insight into the flow distortion and potential flow techniques. Limitations of the 2D modelling led to the development of two axisymmetric line-source codes using constant and linearly varying source strengths respectively. Although these models were ultimately unreliable and ill-suited to the type of modelling conducted, they were successfully implemented and provided some approximate results as required. These models were used to draw conclusions about the positioning of the aircraft near the vehicle before the aerodynamic concerns have been summarised.

5.1 Common Features and Aspects of the External Aerodynamics of Road Vehicles

This section draws from Hucho, W. In: The Aerodynamics of Road Vehicles [45]. Other sources are referenced where relevant.

The history of the aerodynamics of road vehicles is closely linked to that of aircraft. The tools and techniques used to develop aircraft are essentially the same; however, there are several areas which distinguish the aerodynamics of road vehicles from aircraft. The flow over road vehicles is almost entirely turbulent, whereas laminar flow is maximised as far as possible on

aircraft. Road vehicles experience large regions of flow separation whereas aircraft require mostly attached flow. This is owing to the different scales of the Reynolds numbers involved and the practical constraints on the shapes of vehicles. In this section, the particular flow features relating to road vehicles are described and the requirements for additional aerodynamic modelling are stated.

5.1.1 Typical Flow Features of Road Vehicles

The major flow features common to passenger vehicles are shown in Fig. 5.1 and 5.2. At the front road vehicles the positive pressure gradients tend to inhibit boundary layer growth resulting in mainly smooth, laminar flow in this region [*30*]. However, small pockets of circulating flow may form where the vehicle has defined edges, particularly where the windscreen meets the bonnet and around features such as wing mirrors. Still, potential flow models should provide a good approximation of the flow in this region, at distances reasonably far from the surface of the vehicle.

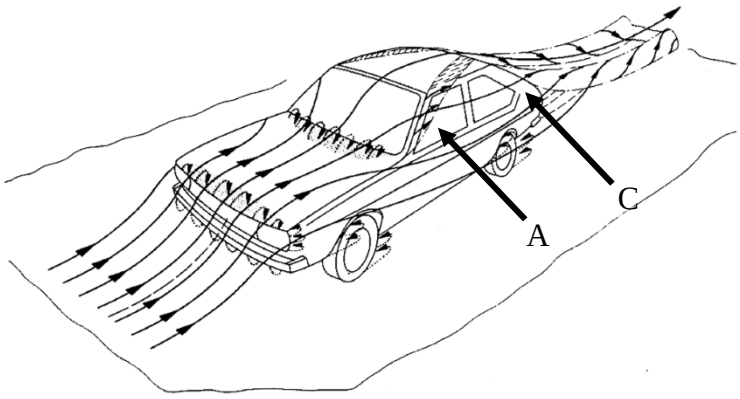

Fig 5.1: Flow features at the front of a ground vehicle. [*46*]

Cone shaped vortices are commonly formed at the A and C pillars (indicated in the figure) where the flow attempts to follow the curve of the vehicle. These vortices have strong circulation and persist for some distance behind the vehicle. These vortex formations are associated with the lift and pitching moments on the vehicle.

The flow at the back of the vehicle is characterised by separation, owing to the negative pressure gradients occurring as the vehicle tapers to its end. Three types of rear end design are shown in Fig. 5.2. From left to right the rear end shapes are called “square back”, “fast back” and “notch back”.

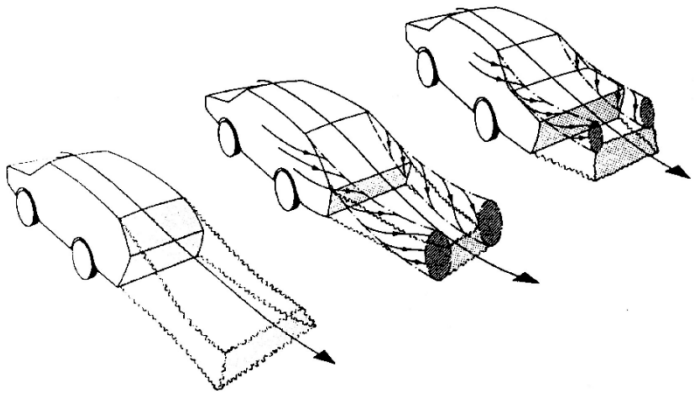

Fig 5.2: Flow separation at the rear of three types of vehicle: square back, fast back and notch back. [*45*]

In the figure above, the strongest vortex formations are indicated along with regions of wake sometimes called “dead water”. The vortices are of concern for the proposed system as they may contribute to the vortices trailing from the aircraft and alter the lift generated. Of the above cases, the square back is most desirable for the base vehicle of the aerodynamic testing apparatus as it generates only very weak vortex formations. Utility vehicles and vans such as those in Fig. 3.2 display this type of flow separation.

While the flow features close to the surface of the vehicle are very important, it has been stated that the aircraft will be positioned relatively far from the vehicle to avoid aerodynamic interference. The flow in this region is laminar and may be modelled as potential flow owing to the insignificant viscous forces outside the boundary layer. The following three figures show the flow over three vehicles in full scale wind tunnel tests.

Figure 5.3 shows the flow over a luxury sedan where the extent of the laminar flow is clearly visible. The separation at the rear window is also noted, where the smoke trails depart from the contour of the rear.

Fig 5.3: Flow over the centreline of a luxury sedan (Mercedes Benz E-class W210). [*47*]

The significant deflection of the airflow around the vehicle is of primary concern for this work. The maximum angle on the highest streamline is 6° and this angle decreases to 0° within half the wheelbase of the vehicle as the flow moves over the roof and then becomes negative at the rear of the vehicle. This angle also decreases as you move laterally away from the centre line of the vehicle, tending to zero. These are all significant changes in the angle of the airflow in distances less than the equivalent wingspan of a large test aircraft. This is owing to the complicated profile of the vehicle.

Passenger vehicles tend to have more curved profiles than utility and commercial vehicles. This may help reduce the magnitude of the flow deflection. In Fig. 5.4 the flow over the centreline of a van is shown. This particular van has a sloped fore body which guides the flow more smoothly over the transition from the windscreen to the roofline. This is in contrast to the commercial vehicle shown in Fig. 5.5 in which large areas of separation have occurred at the forward edges of the cab and body. The van displays promising flow conditions for the proposed apparatus although the apparatus would need to be positioned behind the cg.

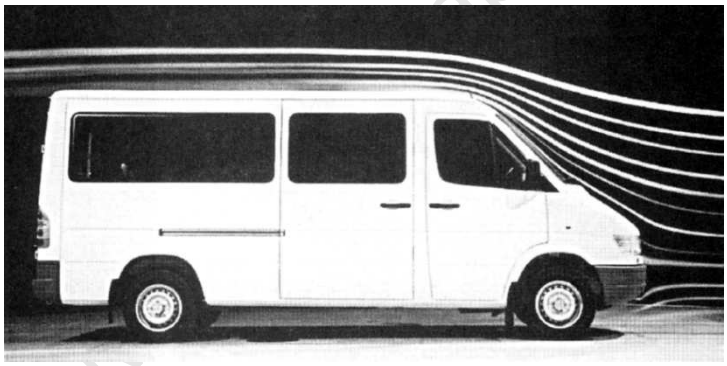

Fig 5.4: Flow over centreline of a van [*48*].

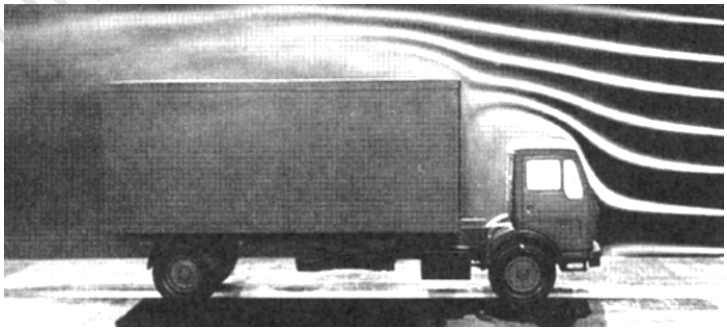

Fig 5.5: Turbulent flow over commercial vehicle [*48*].

Not shown in Fig. 5.4 are the flow patterns near the A pillars at which vortices would develop owing to the raked angle of the windscreen and fore body. These vortices would interfere with the flow field at span-wise distances from the aircraft centreline though their extent has not been modelled in this work.

5.1.2 Additional Aerodynamic Concerns

There are several important aspects of the aerodynamics of road vehicles which have not been discussed or modelled in detail in order to limit the scope of this work. These are briefly discussed here.

The issue of crosswinds and their significant effect on the flow field around the vehicle has not been considered. This is a major reason why low wind conditions will be required for testing. Unsteady vortex shedding is also possible on certain kinds of vehicle and, again, the speed at which vortex shedding is periodic and significant should be avoided.

The thickness of the boundary layer on ground vehicles may be quite significant. As can be seen in Fig. 5.6, the boundary layer on a large commercial vehicle may be as thick as one meter. If the aircraft is to be positioned such that it is not located within this velocity gradient it would need to be positioned significantly further from the vehicle than this.

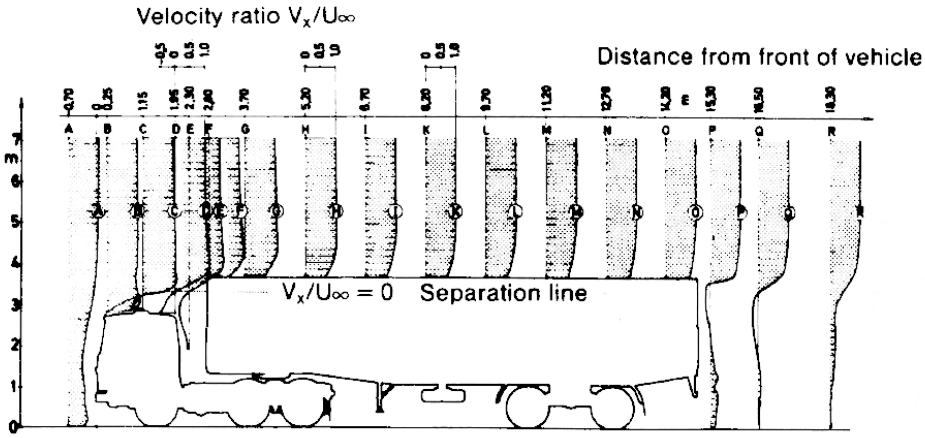

Fig 5.6: Velocity ratios of the flow about a semitrailer with a box shaped body. [*48*].

If the aircraft is positioned outside of the boundary layer, it will still exist within a velocity gradient caused by the deflection of the flow around the vehicle body. This velocity gradient will result in a pressure gradient, causing a buoyancy force on the aircraft. However, if this force is significant it is probable that the flow distortion is too great in the region where the test aircraft has been positioned.

The last major issue which poses a major concern is that of the directional stability of the combined system. The addition of the aircraft will have an effect on the centre of pressure of the vehicle, and will introduce additional moments on the vehicle. It was suggested in chapter 5 that the aircraft be positioned above the centre of gravity for dynamic reasons. It is also

advisable to position the aircraft here from a yaw stability perspective. When positioned above the centre of gravity the aircraft should have nearly zero influence on the lateral stability of the vehicle. There is, however, the problem of the moment of the drag force on the normal force at the front wheels. It is will result in reduced steering ability which could be unsafe.

5.1.3 Requirements of and Approach to Further Aerodynamic Modelling

The work in this section was limited to a literature study and has provided a qualitative overview of the flow field around ground vehicles. It is apparent that the flow field around a vehicle has many features which make it unsuitable for conducting accurate aerodynamic testing. This cast doubt on the feasibility of the concept of using a road vehicle as proposed. There was, however, a need for an approximate, quantitative model of the flow field for estimating the severity of the flow deflection around the test aircraft. In other words, the modelling must provide an approximate quantitative measure of the deflection of the flow along the wing and tail spans of a representation of a large model aircraft.

Options for obtaining this model included CFD, potential flow methods and scale wind tunnel testing. Road vehicles are notoriously difficult to model accurately with CFD and are not easily tested in wind tunnels as scaling effects are significant. Within the scope of this work, CFD and scale wind tunnel testing were not possible. The only option available within the scope of the project was to utilize potential flow methods to provide some approximate results. Further limits on the scope also meant that the influence of the aircraft on the airflow could not be included as 3D modelling was not feasible in the time available.

While it is not known which vehicle would be used for the proposed system, it is desirable to model the flow over some vehicle for which wind tunnel images are available, and which is available for contextual understanding. The Mercedes Benz E-Class (W210) is an aerodynamic luxury sedan which was available for testing and measurement. A wind tunnel image (Fig. 5.3) was also found. The large luxury sedan was a very desirable candidate on which to mount the system as it was fitted with a tow hitch, roof racks, a sun roof and comes standard with cruise control for maintaining test speeds. This vehicle was therefore chosen as the benchmark example.

5.2 Potential Flow Methods

Potential flow methods were deemed to be sufficiently accurate for the approximate aerodynamic modelling conducted in this work. This is because the aircraft would be positioned outside the boundary layer of the flow over the vehicle to avoid complicated aerodynamic interactions as far as possible. These methods have the advantages of simplicity of programming and rapid processing times which allow rapid development of the code for simple cases. Potential flow methods are discussed in this section.

5.2.1 Definition of Potential Flow

Potential flow methods treat fluid flow as inviscid, and irrotational, and ignore mass diffusion and thermal conduction effects. This type of flow is an accurate approximation of the flow outside the boundary layer, where the velocity gradients are small enough to ignore the viscous forces in the fluid. With the afore mentioned approximations, the flow is governed by Laplace's equation given below, where ϕ is the velocity potential.

$$\nabla^2\phi = 0 \qquad \textit{Eq. 5.1}$$

Solutions to the Laplace equation are referred to as harmonic functions and include definitions for uniform flow, sources, sinks, doublets and vortex singularities which have 2D and 3D equivalents.

5.2.2 Solution of Flow over General Bodies in Potential Flow

The Laplace equation is a linear differential equation which means solutions for the potential flow around bodies can be found by the summation of the elementary singularities. For certain fundamental bodies such a sphere, lifting and non lifting flow over cylinders and other bodies, the summations are simple. For finding the flow over a general body, the resulting flow is the result of a more complicated arrangement of singularities.

The surface element panel method is a technique wherein the surface of a body is approximated by dividing it into a number of contiguous elements called panels. Each panel is defined as a singularity (source, sink or vortex panels) with a defined strength distribution (constant, linear or cubic). The influence of the panel at any point in the flow is determined by integrating differential elements of the panel with the parametrically defined strength distribution along the length of the panel. Control points are then defined on each panel at

which the condition of zero flow velocity in the normal direction is imposed. The summation of the influence of all the panels plus the influence of the free stream leads to a set of linear equations which can be solved. These panel methods may be 2D or 3D (with triangular or quadrilateral sources), where the governing equation is the same (equation 5.1) but the complexity of the implementation differs greatly.

In addition to surface panels there exists a similar technique involving the distribution of line singularities on the axis of symmetry of a body of revolution. This method was first introduced by von Karman [*49*] and is termed an interior distribution because the singularities are located within the body. Control points are still defined on the profile and the condition of zero normal velocity is imposed by finding the stream function influence of each singularity on each control point and setting it to zero.

While this technique is more prone to numerical errors caused by poor conditioning of the linear equations, it is a very simple means of solving the flow around bodies of revolution. Surface element panel methods exist for axisymmetric bodies where each panel is a thin conical frustum surface [*50*]. This approach provides a more stable and better conditioned solution to the problem [*51*] but has not been investigated further owing to the limited scope of this work.

5.2.3 Approach to Potential Flow Modelling

For this work, it was initially hoped that the code structure of a 2D surface source panel method, developed by the author for a separate project, could be extended to a full 3D surface source model of a road vehicle. Since 3D panel methods are widely used in industry [*52*], they would have been capable of producing a good approximation of the flow around the ground vehicle. The problem with these methods, however, is that the influences of general triangular and quadrilateral elements require a much more complicated integral to be performed than in 2D. The singularity strength distribution on the panel is also more complicated to define.

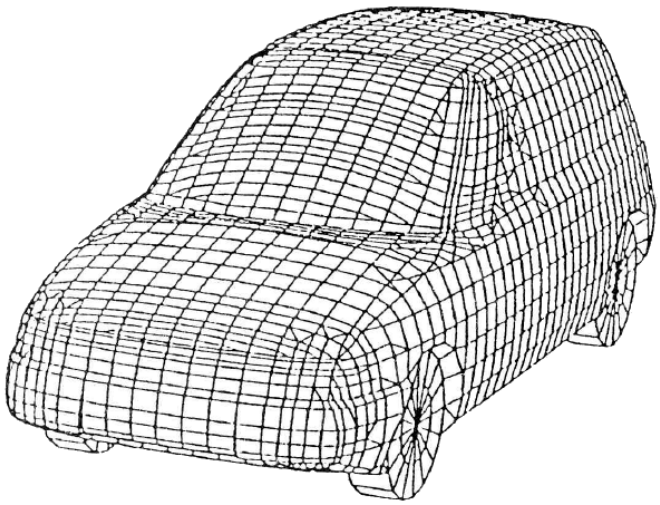

Fig 5.7: Distribution of panels on a vehicle for panel method modelling [*52*].

While the solutions to these integrals were found in the literature [*53*], it was apparent that defining the panels, checking for convergence of the solutions, and solving for the zero normal velocity condition would be impossible within the scope of this work. It is clear from looking at the panel distribution shown in Fig. 5.7 that defining this grid would be a substantial task. Additionally, since potential (and Euler) flow neglect viscous forces, the models are not capable of simulating the separation of the flow at the rear of the vehicle. The inclusion of a wake surface is thus required, usually defined with dipole panels. This poses an additional problem for the implementation of the method, which is compounded by the unknown shape of the wake surface.

Since the 2D flow model is not capable of modelling the variation of the incidence angle of the flow along the wing span of the aircraft, and since a full 3D panel method solution was not feasible, an approximate model was required. It was decided that the vehicle might be approximated as a body of revolution, with the upper part of the profile being revolved around a z-axis which was positioned on the road surface. This model would exhibit an approximation of how the incidence angle of the flow would vary along the wing span. It is noted that this model is a gross approximation of the actual flow and was intended to give a rough numerical solution to note some characteristics of the flow.

The constant strength line source sink method as described in Shames [*54*] was used for the initial formulation of the panel method. This code was later adapted to use linearly varying strength distributions when the shortcomings of the constant strength method were noted. The results of the 2D and axisymmetric modelling are described in the following subsections.

5.3 Approximate Flow using a Two Dimensional Surface-Source Panel Method

A 2D panel method was developed as part of a separate course in aerodynamics. It closely followed the method presented by Anderson [*55*]. Utilising surface source-sink panels, the code used a crude numerical integration of the volume flow rate along the constant potential lines to generate the stream lines. This numerical integration required several hours to produce smooth streamlines, however, the solution of the flow was robust and repeatable.

The streamline technique was validated using the analytical equation for the streamlines over a cylinder which produced very accurate results shown in Fig. 5.8 below.

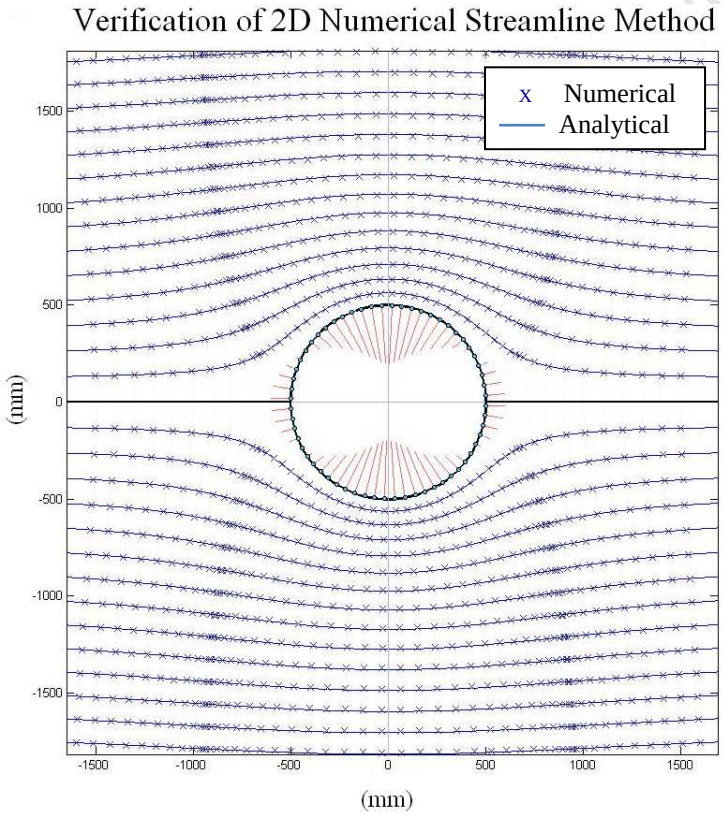

Fig 5.8: Verification of 2D surface source panel method using numerical and analytical streamlines for a cylinder.

The results for the pressure ratio on the surface of the cylinder were also accurately reproduced by the code (indicated with red lines on the control points in the figure). Additionally, it was shown that the volume addition error converged to zero with an increasing number of panels. An example of the conversion check is shown in Fig. 5.9. The curve fit for the volume flow rate error check clearly converges to zero as the number of panels tends to infinity.

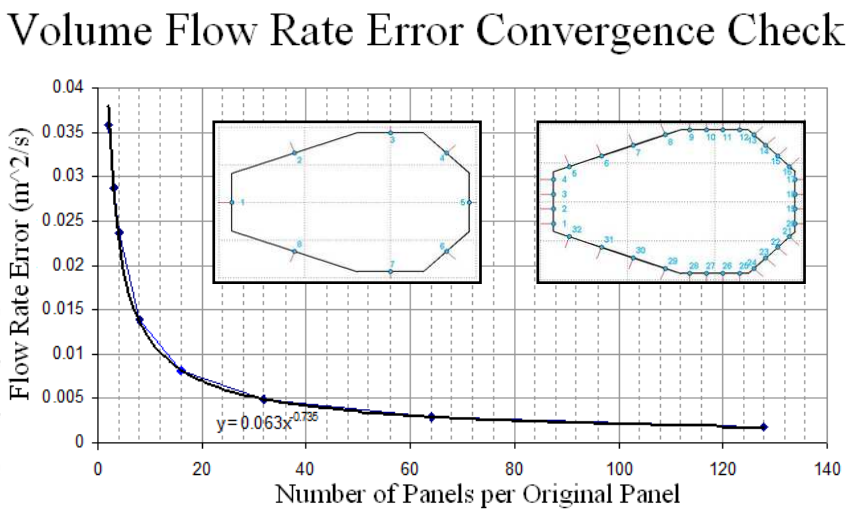

Fig 5.9: Convergence check on 2D panel method.

To model the car, the profile was sampled from a series of carefully taken photographs. The luxury sedan was then approximated by dividing the profile into a large number of panels. The number of panels near the more curved edges was increased to improve the solution in these areas and reduce the volume flow rate error. In order to account for the effect of the road, the vehicle was mirrored about the road line which results in streamline representing the road. The result of the modelling is shown in Fig. 5.10.

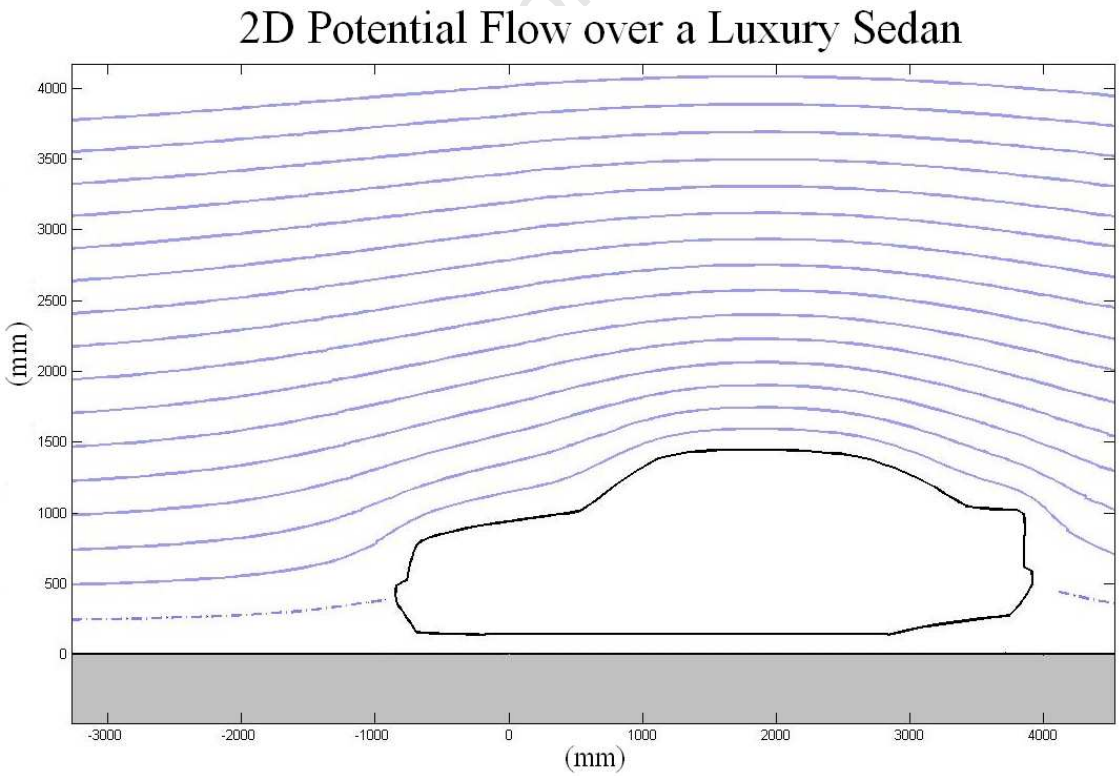

Fig 5.10: 2D Potential flow over an approximation of a luxury sedan.

While the code implementation was successful, it was found to not adequately reproduce the flow. The difference in the angle between the 2D code and the wind tunnel image of the vehicle was as high as 7° in the relevant areas of the flow around the vehicle. The other major shortcoming of this code is that it does not allow any approximation of the variation of the angle of attack along the span-wise directions of the wind and tail.

Examining the results of Fig. 5.8 and comparing to the photograph Fig. 5.3 leads one to draw two important initial conclusions about the positioning of the aircraft in the flow near the vehicle. Firstly, it is clear that the lack of a wake model in the panel method results in a significant discrepancy between the simulated and real flow in the region above and towards the rear of the vehicle. Secondly it is noted that the influence of the vehicle extends significantly far from the vehicle itself, which implies the aircraft should be positioned as far from the vehicle as possible. It should also be noted that it is at the thickest section of the vehicle that the flow is its straightest and so it may be favourable to position the aircraft slightly back from the centre of gravity for aerodynamic reasons.

5.4 Approximate Flow over a Vehicle using an Axisymmetric, Distributed Line Source Method

As mentioned in the approach to the aerodynamic modelling, two axisymmetric interior line source codes were developed. The first code utilised constant strength line sources while the second used linearly varying source strengths. The development and testing of these singularity methods is shown in more detail in appendix E. It was found that, although these codes had been correctly implemented, they were extremely sensitive to the profile shape and to almost all of the simulation parameters available. Despite attempting an extensive range of modelling experiments, only a handful of combinations of the parameters produced any useful results and only the linearly varying line source method provided a reasonable answer.

The best result is shown in Fig. 5.11. An inverted colour version of Fig. 5.3 is shown below for comparison. In this simulation, the number of singularities, f , was set to only 12. The singularities on the axis are linearly distributed but set in from the edges of the body by a distance on 7% of the total length of the body. The control points are linearly distributed between the ends of the body profile. The free stream, V_∞, was set to 120 km/h, in agreement with the ride modelling.

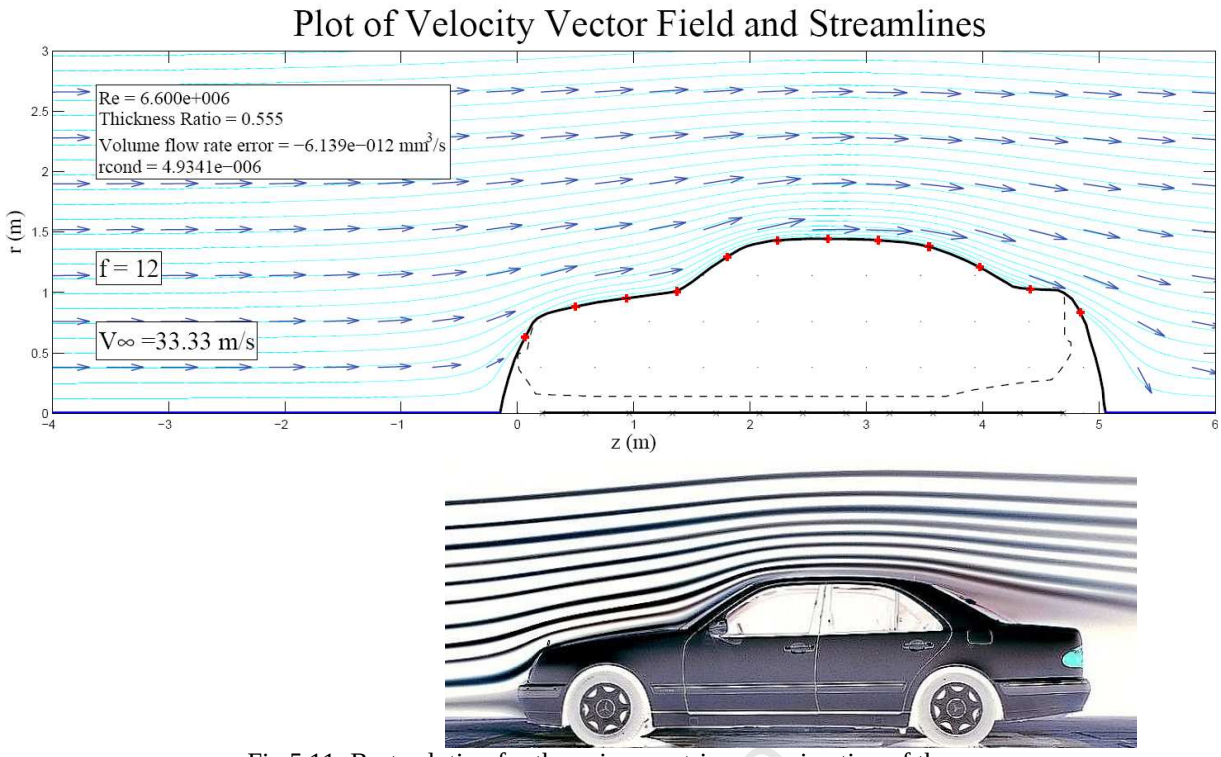

Fig 5.11: Best solution for the axisymmetric approximation of the flow around a Mercedes Benz E-Class (W210).
– Inverted colour image of Fig. 5.3 shown below for comparison [47]

It should be noted that agreement between the axisymmetric flow in the region forward of the separation point on the vehicle, and away from the front bumper of the vehicle where the actual flow splits, is remarkably good. Given the approximations made in this model, it is interesting that such similarity in the longitudinal plane would exist.

While the small number of line sources used above resulted in the best solution of the flow, it was unsatisfactory because the body profile was not accurately captured. It can be seen in Fig. 5.11 that some of the streamlines intersect the surface of the vehicle. While the number of singularities may easily be increased, this causes two types of error to occur which are shown in Fig. 5.12 and 5.13.

In Fig. 5.12 one notes the hazy appearance of the streamlines as well as peculiar bumps in the flow field right near the front and rear of the vehicle. The noise in the streamlines is likely numerical error occurring because the strengths of the sources vary so wildly. Important to note is that the conditioning of this flow is extremely poor. Generally it was noted that increasing the number of singularities resulted in poorer conditioning of the solution.

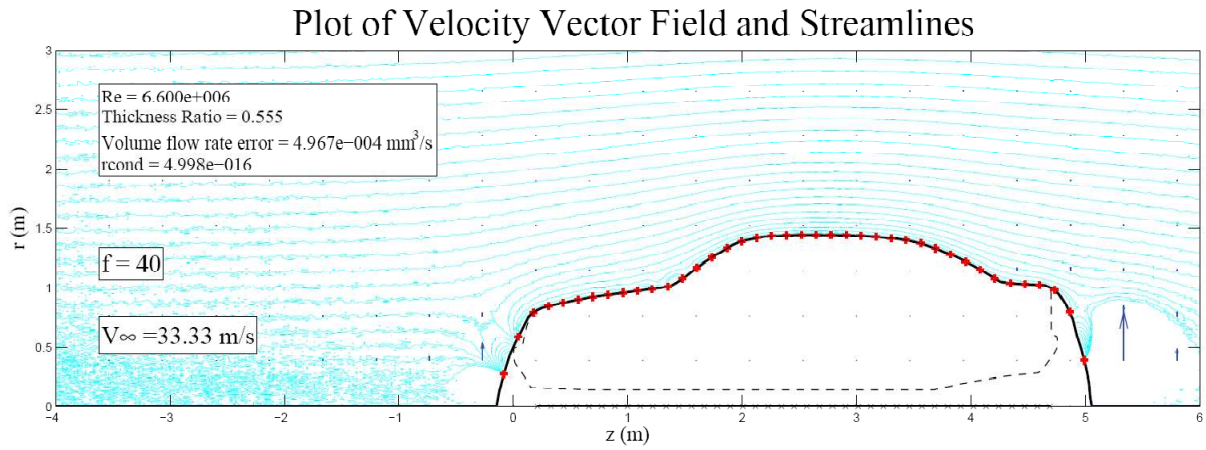

Fig 5.12: Poor numerical accuracy in the flow solution

The second kind of problem that is the most prevalent in these methods is shown in fig 5.13. It is noted that the flow appears to arrive at the vehicle after undergoing a significant departure from a reasonable orientation.

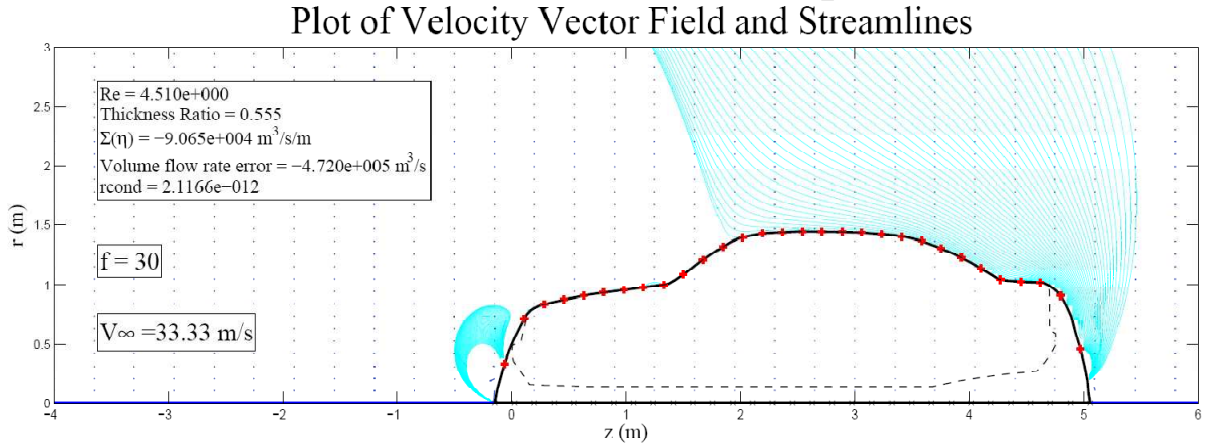

Fig 5.13: An example of an undesirable solution to an axisymmetric flow problem.

This type of solution forms the bulk of the outputs from simulations attempted for this vehicle profile. The constant strength method produces significantly worse performance in this regard. Interestingly, the solution shown above is correct according to the formulation of the linear equations. There is indeed a streamline which passes though each of the control points. This, together with the problem of poor conditioning, is a shortcoming in the interior singularity distribution method.

While the codes developed have been shown to be sensitive to the input parameters and unreliable, the result given in Fig. 5.11 is sufficient to obtain some estimate of the deflection of the airflow in the region described as being best suited to the dynamic performance and longitudinal stability of the proposed apparatus. In Fig. 5.14 a hypothetical aircraft based on

the maximum specifications allowed by the SAMAA has been positioned 3 m above the road, roughly above the centre of gravity of the road vehicle. Note this is slightly less than the height of 3 m distance between the centre of gravity of the vehicle and the model aircraft used in the ride modelling owing to the height of the centre of gravity (this data was not available). The aircraft has a wingspan of 5 m and a tail span of 2 m with the distance between the tail and the wing being set to 2 m.

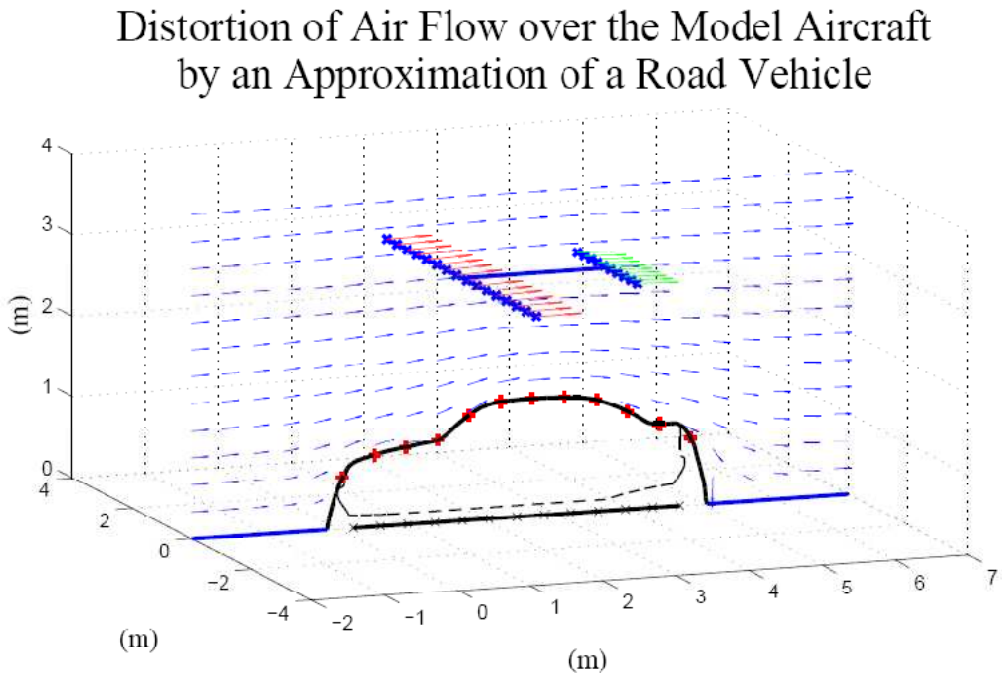

Fig 5.14: A representation of a large model aircraft positioned above the road vehicle. Velocity vectors for the wing (red) and tail (green) are shown.

The velocity vectors at points along the wing and tail are easy to determine for axisymmetric flow as distances along the span line correspond to an increased radius from the axis but on a plane through the z axis, containing the point of interest. The vectors were then resolved into components in the aircraft axis system which allowed the local angle of attack, α, and slip angle, γ, to be found. The local slip angle, γ, is defined as the angle of the velocity vector to the longitudinal plane of the aircraft. Figures 5.15 and 5.16 show the resulting angle variation along the wing and tail respectively.

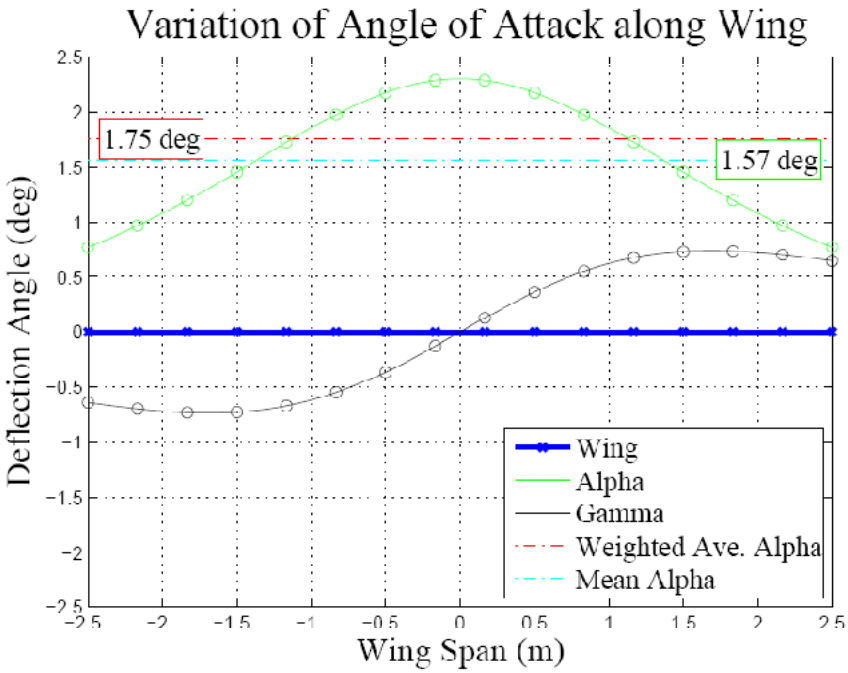

Fig 5.15: Variation of the angle of attack and the slip angle along the wing span.

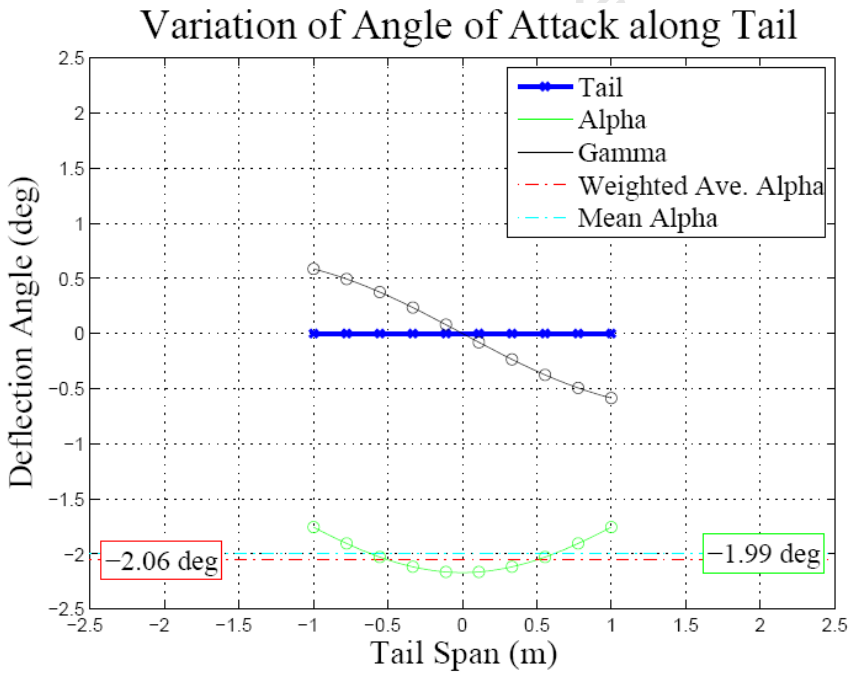

Fig 5.16: Variation of the angle of attack and the slip angle along the tail span.

Shown on the figures are two numbers. The numbers shown in the green boxes indicate the mean angle of attack along the wing and tail. The numbers in red indicate an elliptically weighted average for the angle of attack. These numbers give a better indication of how much the lift and drag coefficients will change. The difference between the two elliptically weighted average angles gives an indication of the error in the pitching moment that will be measured.

At this point, lifting line theory could be used to determine the lift and drag coefficients for the wing and the tail to work out how the error will affect the final readings of the aerodynamic coefficients. The optimal angle at which the aircraft could be oriented could be found in order to determine the maximum potential accuracy which could be obtained. While these calculations would be very instructive, they represent an overstepping of the scope of this analysis and will be fruitless given the approximations made thus far and the unknowable configuration of the aircraft and road vehicle.

What is more important to note is that a variation in the angle of attack along the wing span over about 3° has been predicted. The effective change in the angle of attack seen by the wing is in the region of 1.75°, which would be much higher for a smaller wing. The difference in the elliptically weighted average angle between the wing and the tail is 3.81° (though this angle would be less if a wake model had been included). Considering that these angles would represent a significant change in the lift forces be generated, the result does not bode well for the configuration proposed for this system as a means of obtaining aerodynamic coefficients.

5.5 Summary and Discussion of the Aerodynamic Issues facing Vehicle Mounted Testing

The investigations in this chapter have been only partially successful and partially conclusive. What has been made apparent is that the distortion of the airflow around a road vehicle is significant. For even approximately accurate aerodynamic measurements to be obtained it is clear that the aircraft must be positioned far from the influence of vortex formations, thick boundary layers and turbulence. Additionally, the distortion of the flow away from the vehicle, where potential flow is applicable, is itself significantly distorted even at a reasonable distance from the road vehicle.

However, it must be noted that this study has been limited in scope. The techniques chosen to model the flow around the vehicle were unstable and gross approximations have been made in numerous places. The flow of only one vehicle has been modelled which may not be the ideal vehicle for the purposes of the proposed apparatus. Vehicles such as the utility vehicle and van shown in Fig. 3.2 may have a more suitable flow field for testing, as seen in Fig. 5.4. The limited scope of this chapter therefore, is not conclusive in determining the potential to test the aircraft on other vehicles.

The slip angle, γ, indicates that there may be an additional contribution to the wingtip vortices due to the flow being blown outwards under the wing assisting the vortex formation. It has also not been established how the vortex formations on the road vehicle may interact with the wingtip vortices of the aircraft and how this will affect lift and drag. Also not investigated is the additional lift generated on the aircraft by the pressure distribution in the flow around the vehicle. The current work has not modelled these and other interactions between the aircraft and the road vehicle.

On the other hand, the problem of the changing angle of attack of the flow around the vehicle has indicated that the varying angle of attack will be a significant problem which has no easy solution while maintaining the safety of the test vehicle. This may mean that a ground vehicle mounted aerodynamic testing apparatus may only be useful in conducting the other kinds of testing mentioned in Chapter 3. Since the angle variation is small enough not to cause stall at low angles of attack, the system should still be capable of measuring an increase in certain performance figures relative to a base measurement (for example, determining the decrease in drag with the addition of winglets).

6 Discussion and Conclusion

With both the ride and aerodynamics of the road vehicle examined and modelled in order to better understand the interactions between the vehicle and the aircraft to be tested, a final assessment on the feasibility of such a system must be made. Before this is done, however, it is important to note that the scope of this study was limited at the end of Chapter 3 in order to isolate the important physics of the proposed ground vehicle mounted aerodynamic testing apparatus. What this means is that conclusions drawn here are made only in the context of the concept as defined in Chapter 3, and that they are only made on the basis of two parts of a larger, more complex system requiring further modelling and design.

The ride investigation brought to light the problems faced by the system in terms of the accelerations imparted to the aircraft which would be measured. It was noted that since no road has a zero mean, that limited sections of test road or runway would be required and even in this case there would be transient features at these test sites which would require sections of data to be scrapped. This tied together with the aerodynamic worries of unsteady aerodynamics and additional aerodynamic forces being generated on the aircraft.

It was noted that one of the most serious concerns for the system from a ride perspective are the higher frequency vibrations which would generate the highest forces. These high frequency vibrations could be filtered out mechanically to some degree but, in order to obtain useful data, filtering and statistical analysis of the output signals would be necessary.

Examining the output of the ride models and simulations, the effect of altering certain parameters revealed some important insights. It was noted that if the mass and pitching moment of inertia of the vehicle could be increased it would reduce the accelerations of the vehicle. It was seen that the positioning of the aircraft plays a significant role in changing the accelerations measured by the balance. The result from this section concluded that the best location for the aircraft would be vertically above the centre of gravity and as close as possible to it.

This conclusion was in conflict of the outcome of the aerodynamic investigations undertaken. Here it was clear that the further from the vehicle the aircraft was positioned, the lower the distortion of the airflow would be. This would also reduce the interactions between the aerodynamics of the aircraft and other features of the flow around vehicles such as the

boundary layer and powerful vortices present at the rear of the vehicle. The aerodynamic requirements favoured a slightly rearward positioning of the aircraft towards the thickest part of the vehicle where the flow straightens before following the contour of the rear of the vehicle.

Not modelled directly but discussed was the aerodynamic stability of the vehicle with the apparatus. From a yaw perspective, locating the aircraft above or behind the centre of gravity would be acceptable. The pitching moment of the aircraft drag force on the vehicle was also mentioned as a concern. Placing the aircraft too high would cause a reduction in the normal force on the front wheels of the vehicle reducing its ability to steer. This would also be a concern for the lateral stability of the vehicle, where the side winds would cause a rolling moment, raised centre of gravity would cause the vehicle to be less stable in roll.

The aerodynamic modelling was limited by the scope of this work and was not able to provide any concrete answers about the final errors measured by the system in terms of the desired aerodynamic coefficients. The potential flow models simply provided an indication of the magnitude of the angle of attack and slip angle variation along the wing and tail. Elliptically weighted averages suggested that, for a position where the wing was located above the centre of gravity of the road vehicle a height of 3 m above the road, the angle of attack would be increased by 1.75° with a variation along the span of approximately 3°. This amount of distortion suggests that the system may not be capable of measuring the aerodynamic coefficients of a model aircraft. However, this result is not conclusive since only a specific case has been investigated using only approximate models.

Change in the angle of attack is also concerning when it is considered that the vehicle statics have not been taken into account. This means that the angle of attack of the aircraft relative to the road is not likely to be known with any degree of certainty. Should such a system be constructed, there will have to be some form of wind angle sensor included in the system.

Concluding from this point, it is tempting to state that the system may only be capable of providing a very crude measure of the forces acting on an aircraft and is not likely to provide any useful data for aircraft designers. It is important to first look at concepts for slight modifications to the definition of the conceptual system in Chapter 3. Indeed, the definition was left non-specific to allow for some speculation to be made at this point. Figure 6.1 presents a number of concepts which have been proposed as variations on the basic idea.

	Sketch:	Description:	Advantages (+) and Disadvantages (-):
a)	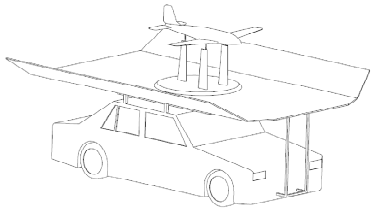	Vehicle with guides for straightening flow	+ Reduce flow distortion + Operate on runways and highways + Mounted to available road vehicles + Ride isolation by vehicle - Complicated construction - Effect on stability of vehicle - Exposed to weather - Limited by road regulations - Risk to vehicle and operator
b)	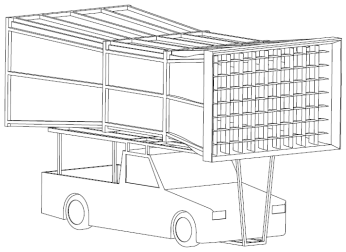	Enclosed test section	+ Reduce flow distortion + Protection from gusts + Operate on runways and highways + Ride isolation by vehicle - Complicated construction - Effect stability of vehicle - Limited by road regulations - Risk to vehicle and operators - Limited test section size - Large size
c)	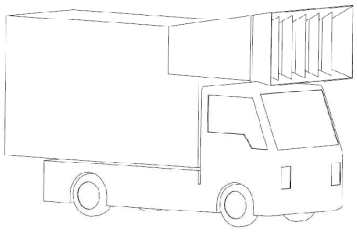	Light truck completely enclosing test section	+ Reduce flow distortion + Protection from gusts + Operate on runways and highways + Ride isolation by vehicle - Significant modification to vehicle - Limited test section size - Large size - Vehicle cost
d)	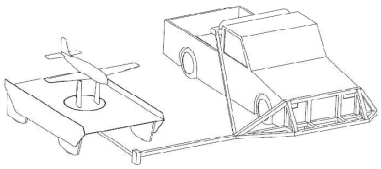	Towed trailer outside of vehicle wake	+ Avoid flow distortion by vehicle + Minimal flow distortion by trolley + No drive on trolley - Exposed to weather - Operate on runways only - Trailer must provide ride isolation - Complicated tow arrangement
e)	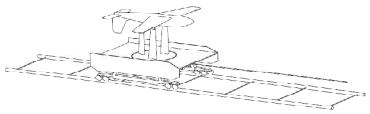	Indoor, self-powered trolley	+ Weather not an issue + Minimal flow distortion by trolley + Smooth surface limits ride vibration - Requires large empty indoor space - Long rails or guides - Requires drive system (low speed)
f)	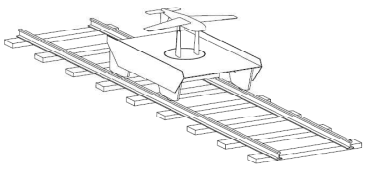	Railway trolley	+ Minimal flow distortion by trolley - Exposed to weather - Trailer must provide ride isolation - Long, straight, rail must be found

Fig 6.1: Variations of the basic concept for a ground vehicle mounted aerodynamic testing apparatus.

Each of these concepts addresses the problem of flow distortion in some way. While many of these concepts are commonly suggested, it is clear that they all have disadvantages. All but one of the concepts proposed above have fatal flaws which are owing to the safety of the vehicle and its operators (a and b), increased size and expense (b and c) or lack of availability of test locations (c, e and f). Concept e, however, may be feasible as a project specifically for the University of Cape Town.

The concept is the only indoor concept proposed which would eliminate the problem of weather and wind. Large indoor facilities with long open smooth floors are not commonly available. However, the sports centre at University of Cape Town a long indoor venue if it is empty and all the section dividers are removed. Reaching the maximum speeds of some UAVs for testing will be difficult and require high acceleration indoors, with short distances available. This will require a high power drive system. However, it may be acceptable to limit the maximum testing speed of the apparatus. Designing and constructing a drive system capable of this will not be cheap. It is not necessary to travel at maximum speed to obtain aerodynamic coefficients for low speed aircraft. There is a significant problem with the availability of this large venue.

In conclusion, the proposed road vehicle mounted system as defined in Chapter 3, is unlikely to provide sufficiently accurate data for obtaining the aerodynamic coefficients of large model aircraft. This claim cannot be verified without more detailed modelling of a vehicle and aircraft or, alternatively, actual experimental data from a prototype system. The system would, however, be able to provide a useful tool for comparing the performance gain of a modification to an airframe amongst other forms of testing. A powered indoor trolley could provide a platform for a ground vehicle testing apparatus; however, large indoor venues are not widely available.

The project has highlighted all of the physical and logistical problems facing the development of such a system, however, it has not been able to draw a final conclusion owing to the limited scope of the work. The overall aim of the project has only been partially met but has been investigated to the furthest degree possible within the scope of this dissertation. In completing this study the following additional outputs were produced:

- An accumulation of literature relating to road roughness, road modelling and random road generation.
- A pair of PSD and time domain simulation vehicle models have been developed for the quarter car and pitch bounce models.
- A random road generator capable of generating roads from discontinuous roughness models was developed.
- An accumulation of papers, reports and text book on two-dimensional, two-dimensional axisymmetric and three dimensional panel methods.
- A pair of two dimensional, axisymmetric, interior distribution, potential flow models have been developed with constant and linearly varying line source strengths.

7 Recommendations

The recommendations for this work are divided into those which indicate the best direction in which to develop a low cost ground vehicle based aerodynamic testing apparatus, and those which indicate improvements to the mathematical models developed in the process of conducting this work.

7.1 Recommendations for Further Investigation of the Ground Vehicle Mounted Aerodynamic Testing Apparatus Concept

As far as the development of a low cost aerodynamic testing apparatus is concerned, it is believed that further numerical modelling and simulations will not be capable of providing any deeper insight into the problem. The complicated nature of the flow around a vehicle, and the interactions between this flow and the flow over an aircraft, while undergoing ride motions, will not be able to be modelled to any meaningful accuracy. This concept requires a prototype system to be built and tested. The foundation of this work will guide intelligent design decisions for the prototype which will lead to conclusive results. The following steps should be carried out:

- Obtain a model aircraft of which the aerodynamic characteristics are well known. The CSIR's Indiza airframe is suggested as a good test case.
- Design a simple, low cost longitudinal balance capable of measuring the forces on the aircraft. A spring balance, utilizing displacement sensors to obtain forces, is suggested as a potential method for both isolating the aircraft from high frequency vibrations and eliminating the problem of shock loading of load cells. The balance should be capable of logging data.
- Design a trolley capable of achieving and maintaining a reasonable speed indoors without excessively accelerating the aircraft and balance. This trolley may be on rubber wheels or mounted on PVC rails as shown in Fig. 3.1. Conduct testing with the aircraft inverted in order to prevent the trolley from lifting at higher speeds. Compare the results obtained to those measured for the aircraft in a wind tunnel.

- Mount the balance on a road vehicle such as those shown in Fig. 3.2 and conduct test runs on a closed airfield. Compare the results obtained to those measured for the aircraft in a wind tunnel. Determine if a wind angle sensor is required.
- In both sets of testing flow visualisations should be made in order to identify areas of the flow field which may be resulting in errors.

7.2 Recommendations for the Further Development of the Random Road Generator and Vehicle Ride Models

The ride modelling conducted produced some very interesting and useful results. The capability of the random road generator in generating roads for PSD models with discontinuities is a valuable tool for vehicle ride simulation. However, the limitation of the road generator to 100 harmonic components was a major concern. The simulation models of the vehicle were successfully implemented, but have scope to be improved to include the unsprung masses at the wheels and to include roll. Roll would require correctly correlated left and right tracks of the road surface to be generated. The recommendations are as follows:

- Improve the random road generator to allow it to be composed of a greater number of harmonic components.
- Extend the road generator such that it is capable of generating a pair of correctly correlated left and right road tracks.
- Extend the pitch-bounce ride model to include roll and the unsprung masses at each wheel.

7.3 Recommendations for the Further Development of the Axisymmetric Potential Flow Methods

The axisymmetric potential flow methods developed for the vehicle modelling were very unstable for the modelling required in this dissertation. If further axisymmetric modelling is to be conducted, the following recommendations have been made:

- Change the singularity type from sources to doublets and re-test the performance of the code.
- Replace the interior singularity distribution method with a panel method using conical frustum surface source elements.

8 References

[1] Denel Dynamics. Denel Dynamics. [Online]. http://www.deneldynamics.co.za/brochures/Broc0268_Seeker%20II%20External.pdf

[2] ATE. ATE-group. [Online]. http://www.ate-group.com/medias/articles/ATE%20Vulture%20Brochure%20small.pdf

[3] ATE. ATE. [Online]. http://www.ate-group.com/medias/articles/ATE%20Kiwit%20Brochure%20small.pdf

[4] ATE. ATE-group. [Online]. http://www.ate-group.com/ate_Product/2/index.html

[5] National Health Laboratory Services. [Online]. http://www.nhls.ac.za/about_news.html

[6] CSIR. (2008, October) CSIR Research Space. [Online]. http://researchspace.csir.co.za/dspace/bitstream/10204/3287/1/Monk_2008.pdf

[7] B.A. Broughton, R. Heise, and D. Blaauw, "A Variable Stability, Blended-Wing-Body, Research UAV," in *Royal Aeronautical Society Annual Applied Aerodynamics Research Conference*, London, 2008, p. 6.

[8] CSIR, "Annual Report 2008/9," 2009.

[9] CSIR. (2008, May) CSIR. [Online]. http://www.csir.co.za/researcher_profiles/Bennie_Broughton.html

[10] CSIR. (2009, February) CSIR. [Online]. http://www.csir.co.za/enews/2009_feb/gen_02.html

[11] Candes Keating. Cape Peninsula University of Technology. [Online]. http://info.cput.ac.za/News/news.php?aid=690

[12] DIY Drones. [Online]. http://diydrones.com/

[13] South African Model Aircraft Association. (2001, February) South African Model Aircraft Association. [Online]. http://www.samaa.org.za/pdf/manual_of_procedures.pdf

[14] L.A. Ingham, T. Jones, and A. Maneschijn, "Considerations for Flight Testing of UAVs in South African Airspace," *The Aeronautical Journal*, pp. 803-811, December 2006.

[15] M.A. Leschziner, "Modelling Turbulent Separated Flow in the context of Aerodynamic Applications," *Fluid Dynamics Research*, vol. 38, pp. 174-210, 2006.

[16] R Agarwal, "Computational Fluid Dynamics of Whole Body Aircraft," *Annual Review of Fluid Mechanics*, vol. 31, pp. 125-169, 1999.

[17] D.D. Baals and W.R. Corliss, *Wind Tunnels of NASA. (NASA SP; 440)*., 1981.

[18] U.S.centennial of flight commission. [Online]. http://www.centennialofflight.gov/essay/Evolution_of_Technology/first_wind_tunnels/Tech34G2.htm

[19] R.C. Pankhurst and D.W. Holder, *Wind Tunnel Technique*.: Sir Isaac Pitman & Sons LTD, 1952.

[20] Scaled Composites. (2003, October) Scaled Composites. [Online]. http://www.scaled.com/projects/tierone/spaceshipone_ground_tests

[21] Scaled Composites. Scaled Composites. [Online]. http://www.scaled.com/projects/tierone/gallery/ground_general/wind_tunnel_800

[22] G.J. Brown and Vertigo_inc., "Tethered Parafoil Technique," *AIAA-1989-903*, 1989.

[23] J.M. Stein, "Parachute Testing for the NASA X-38 Crew Return Vehicle," NASA, Houston, Texas, 2005.

[24] Bram Timmer. (2010, July) Inside. [Online]. http://www.inside.ca/2010/07/09/dolly/

[25] Thule. (2010) Thule. [Online]. http://www.thule.co.za/Frames/

[26] Department of Transport. (1999) National Road Regulations. [Online]. http://nasp.dot.gov.za/library/regulations/1999/roadregs.pdf

[27] SANS 10047:2009 - The testing of motor vehicles for roadworthiness, 2009.

[28] The Automoile Association (AA) South Africa. (2010, June) The AA South Africa. [Online]. http://www.aa.co.za/content/62/vehicle-operating-costs/

[29] Toyota. Toyota South Africa. [Online]. http://www.toyota.co.za/VehicleSpecification.aspx?VehicleModelID=47

[30] T. D. Gillespie, "Road Loads," in *Fundamentals of Vehicle Dynamics*. Warrendale, PA, United States of America: Society of Automotive Engineers, 1992, ch. 4, pp. 79-124.

[31] J. Y. Wong, "Mechanics of Pneumatic Tyres," in *Theory of Ground Vehicles*.: John Wiley & Sons, 1978, ch. 1, pp. 3-54.

[32] J. B. Barlow, W. H. Rae, and A. Pope, "Wind Tunnel Design," in *Low-Speed Wind Tunnel Testing*.: John Wiley & Sons, 1999, pp. 61-135.

[33] K. Watkins. PCB Load and Trque. [Online]. http://www.pcbloadtorque.com/downloads/Load_Cells_article.pdf

[34] J. B. Barlow, W. H. Rae, and A. Pope, "Flow Instrumentation," in *Low-Speed Wind Tunnel Testing*.: John Wiley & Sons, 1999, pp. 154 - 170.

[35] T. D. Gillespie, "Ride," in *Fundamentals of Vehicle Dynamics*. Warrendale, PA, United States of America: Society of Automotive Engineers, 1992, ch. 5, pp. 125-194.

[36] M. W. Sayers and S. M. Karamihas. (1998, September) The Little Book of Profiling. [Online]. www.umtri.umich.edu/content/LittleBook98R.pdf

[37] C. J. Dodds and J. D. Robson, "The description of road surface roughness," *Journal of Sound and Vibration*, vol. 32, no. 2, pp. 175-183, 1973.

[38] J. Y. Wong, "Vehicle Ride Characteristics," in *Theory of Ground Vehicles*. New York: John Wiley & Sons, Inc., 1978, ch. 7, pp. 264 - 289.

[39] B. Bruscella, V. Roulliard, and M. Sek, "Analysis of road surface profiles," *Journal of Transportation Engineering*, vol. 125, no. 1, pp. 55 - 59, January/Februarry 1999.

[40] V. Rouillard, M. A. Sek, and B. Bruscella, "Simulation of Road Surface Profiles," *Journal of Transport Engineering*, vol. 127, no. 3, pp. 2047-2043, May/June 2001.

[41] S. Türkay and H. Akçay, "A study of random vibration characteristics of the quarter car model," *Journal of Sound and Vibration*, vol. 282, pp. 111-124, 2004.

[42] M. Shinozuka, "Simulation of Multivariate and Multidimensional Random Processes," *The Journal of the Acoustical Society of America*, vol. 49, no. 1, pp. 357-368, 1971.

[43] J. Y. Wong, "Vehicle Axis System," in *Theory of Ground Vehicles*. New York: John Wiley & Sons Inc., 1978, p. 211.

[44] J. Marzbanrad, G. Ahmadi, Y. Hojjat, and H. Zohoor, "Optimal Active Control of Vehicle Suspension System Including Time Delay and Preview for Rough Roads," *Journal of Vibration and Control*, vol. 8, pp. 967-991, 2002.

[45] W. Hucho, "Aerodynamic Drag of Passenger Cars," in *Aerodynamics of Road Vehicles*, 4th ed., W. Hucho, Ed. Warrendale, Pa: SAE International, 1998, ch. 4, pp. 131-237.

[46] W. Hucho, "Introduction to Automobile Aerodynamics," in *Aerodynamics of Road Vehicles*, 4th ed., W. Hucho, Ed. Warrendale, Pa: SAE International, 1998, ch. 1, pp. 1-57.

[47] J Edgar. (2007, July) Aero Testing - Part 4: A fantastic collection of DaimlerChrysler wind tunnel pics. [Online]. http://autospeed.com/cms/A_108676/article.html?popularArticle

[48] H. Gotz and G. Mayr, "Commercial Vehicles," in *Aerodynamics of Road Vehicles*, 4th ed., W. Hucho, Ed. Warrendale, Pa: SAE International, 1998, ch. 9, pp. 415-488.

[49] T. von Karman, "Calculation of Pressure Distribution on Airship Hulls," NACA-TM-574, 1930.

[50] J. L. Hess, "Review of Integral Equation Techniques for Soving Potential-Flow Problems with Emphasis on the Surface-Source Method," *Computer Methods in Applied Mechanics and Engineering*, vol. 5, pp. 145-196, 1975.

[51] J. L. Hess and R. P. Martin, "Improved Solution for Potential Flow about Arbitrary Axisymmetric Bodies by the Use of a Higher Order Surface Source Method," Douglas Aircraft Company, Long Beach, California, Contractor Report NASA CR 134694, 1974.

[52] S. R. Ahmed, "Computational Fluid Mechanics," in *Aerodynamics of Road Vehicles*, 4th ed., W. Hucho, Ed. Warrendale, Pa: SAE International, 1998, ch. 15, pp. 765-836.

[53] F. A. Woodward, "An Improved Method for the Aerodynamic Analysis of Wing-Body-Tail Configurations in Subsonic and Supersonic Flow: Part 1 - Theory and Application," Langley Research Center, NASA-CR-2228, 1973.

[54] H.I. Shames, "Part F: Axisymmetric Three-Dimentional Flows," in *Mechanics of Fluids*, 3rd ed.: McGraw-Hill, 1992, ch. 12, pp. 599-614.

[55] J. D. Anderson, "Fundamentals of Inviscid, Incompressible Flow," in *Fundamentals of Aerodynamics, International Edition*, 4th ed. New York, NY: McGraw Hill, 2007, ch. 3, pp. 187-293.

[56] T. D. Gillespie, M. Sayers, and L. Segel, "Calibration of Response Type Road Roughness Measuring Systems," Final Report 1980.

[57] J. Marcondes, G. J. Burgees, R. Harichandran, and M. B. Snyder, "Spectral Analysis of Highway Pavement Roughness," *Journal of Transportation Engineering*, vol. 117, no. 5, pp. 540-549, 1991.

[58] J. A. Marcondes, M. B. Snyder, and P. S. Singh, "Predicting Vertical Acceleration in Vehicles Through Road Roughness," *Journal of Transportation Engineering*, vol. 118, no. 1, pp. 33-49.

[59] O. Kropáč and P. Múčka, "Estimation of waviness of longitudinal road profile from straightedge measurement," *Journal of Transport Engineering*, vol. 135, no. 11, pp. 801 - 812, November 2009.

[60] O. Kropáč and P. Múčka, "Alternative single-number indicator of longitudinal road uneveness," *Canadian Journal of Civil Engineering*, vol. 36, no. 3, pp. 389 - 401, March 2009.

[61] B. D. van Deusen, "Analytical techniques for designing ride quality into automotive vehicles," *SAE Transactions*, vol. 76, 1967.

[62] K. Ramji, A. Gupta, V. H. Saran, V. K. Goel, and V. K. Kumar, "Road roughness measurement using PSD approch," *Institute of Engineering (India) Journal - Civil Engineering*, vol. 85, pp. 193 - 201, November 2004.

[63] O. Kropáč and P. Múčka, "Be careful when using the international roughness index as an indicator of road roughness," *Journal of Sound and Vibration*, vol. 287, pp. 989 - 1003, 2005.

[64] H. M. Ngwangwa, P. S. Heyns, F. J. Labuschangne, and G. K. Kululanga, "Reconstruction of road defects and road roughness classification using vehicle response with artificial neural networks simulation," *Journal of Terramechanics*, vol. 47, no. 2, pp. 97-111, 2010.

[65] B. Bruscella, "Analysis and simulation of the spectral and statistical properties of road roughness for package performance testing," Victoria University of Technology, Masters Thesis 1997.

[66] A. N. Heath, "Application of the isotropic road roughness assumption," *Journal of Sound and Vibration*, vol. 115, no. 1, pp. 131-114, 1987.

[67] International Organisation for Standardization (ISO), ISO 8608: 1995(E). Mechanical vibration - road surface profiles - reporting of measured data, 1995.

[68] M. F. Zedan and C. Dalton, "Potential Flow around Axisymmetric Bodies: Direct and Inverse Problems," *AIAA Journal*, vol. 16, no. 3, pp. 242-250, 1977.

[69] J. L. Hess, "The Unsuitability of Ellipsoids as Test Cases for Line-Source Methods," *Journal of Aircraft*, vol. 22, no. 4, pp. 346-347, 1985.

[70] V. N. Belykh, "On Solving the Problem of an Ideal Incompressible Fluid Flow Around Large-Aspect-Ratio Axisymmetric Bodies," *Journal of Applied Mechanics and Technical Physics*, vol. 47, no. 5, pp. 661-670, 2006.

[71] C. Anderson. (2007, June) DIY Drones. [Online]. http://diydrones.com/profiles/blog/show?id=705844%3ABlogPost%3A731

[72] G. Ruf, "The Calculation of the Vibrations of a Four-wheeled Vehicle, Induced by Random Road Roughness of the Left and Right Track," *Vehicle system dynamics*, vol. 7, no. 1, pp. 1-23, 1978.

Appendix A – Definition and Differentiation of Road Roughness PSD Curves

In this appendix, the continuous elevation PSD function is defined and the relationships with the slope and spatial acceleration functions are found. This is achieved by differentiating a spatial harmonic component of the road signal with respect to distance, and then defining the required spectral density functions. The harmonics can also be defined in terms the temporal frequency which allows PSD functions for velocity and acceleration to be found. This is achieved by taking the time derivatives of the harmonic components and then defining the new PSD functions.

Units in this appendix are reported without simplification to more basic forms. This is done to maintain complete units of frequency in the denominator of the PSD functions, and to preserve the distinction between units of distance in the elevation and horizontal translation.

This appendix draws heavily on the initial definition of the spectral density function presented in Wong [*38*], and expands upon it to obtain the desired results.

A.1 PSD Curves with Spatial Frequency

A single harmonic component, z_n, of the road as a function of the horizontal displacement, x^E, in m, is given below in equation A.1.

$$z_n(x^E) = Z_n \sin(2\pi\Omega_n x^E) \qquad \textit{Eq. A.1}$$

Where Ω_n is the spatial frequency in $cycles/m$ and Z_n is the magnitude of the harmonic component in m. The mean square of this component is found as follows.

$$\overline{z_n}^2 = \Omega_n \int_0^{\frac{1}{\Omega_n}} [Z_n \sin(2\pi\Omega_n x^E)]^2 \, \mathrm{d}x^E$$

$$= \frac{{Z_n}^2}{2} \qquad \textit{Eq. A.2}$$

Differentiating equation A.1 with respect to x^E, one obtains:

$$\frac{dz_n(x^E)}{dx^E} = z_n'(x^E) = 2\pi\Omega_n Z_n \cos(2\pi\Omega_n x^E) \qquad \textit{Eq. A.3}$$

Obtaining the mean square:

$$\overline{z_n'}^2 = \Omega_n \int_0^{\frac{1}{\Omega_n}} [2\pi\Omega_n Z_n \sin(2\pi\Omega_n x^E)]^2 \, dx^E$$

$$= (2\pi\Omega_n)^2 \frac{{Z_n}^2}{2} = (2\pi\Omega_n)^2 \overline{z_n}^2 \qquad \textit{Eq. A.4}$$

The factor $(2\pi\Omega_n)^2$ appears in front of the mean square value for the elevation function. This factor appears again following a second differentiation giving:

$$\overline{z_n''}^2 = (2\pi\Omega_n)^4 \overline{z_n}^2 \qquad \textit{Eq. A.5}$$

In Wong [*38*], the definition of the discrete spectral density function is presented as the starting point for defining the continuous spectral density function. The mean square contribution of a small interval, $\Delta\Omega$, of the total bandwidth is:

$$\overline{z_n}^2 = G_{z_r}(\Omega_n)\Delta\Omega \qquad \textit{Eq. A.6}$$

Where $G_{z_r}(\Omega_n)$ is defined as the density of the mean square value in the interval. The units are in elevation squared per frequency, but the specific units used in the literature vary depending on the units chosen for frequency and elevation. In this work, units of $m^2/cycles/m$ are used for reporting the elevation PSD. However, for ease of implementation, the accompanying code makes use of the units $m^2/rad/m$ internally. These are converted to other units which are selected from a list in the accompanying computer code.

To define the continuous spectral density function, the number of discrete harmonic frequencies is increased towards infinity. The spectral density function then becomes essentially continuous. The continuous spectral density function is therefore defined so that the mean square value of any frequency band is:

$$\bar{z}^2_{\Omega_1 \to \Omega_2} = \int_{\Omega_1}^{\Omega_2} G_{z_r}(\Omega) d\Omega \qquad \textit{Eq. A.7}$$

Now the slope and spatial acceleration PSD functions must be found. Multiply both sides of equation A.6 by the factor $(2\pi\Omega_n)^2$ found in equation A.4. One obtains:

$$\overline{z'_n}^2 = (2\pi\Omega_n)^2 G_{z_r}(\Omega_n)\Delta\Omega \qquad \textit{Eq. A.8}$$

Again, letting the number of frequencies increase towards infinity one can write a different continuous function:

$$\overline{z'}^2_{\Omega_1 \to \Omega_2} = \int_{\Omega_1}^{\Omega_2} (2\pi\Omega)^2 G_{z_r}(\Omega) d\Omega$$

$$= \int_{\Omega_1}^{\Omega_2} G_{z'_r}(\Omega) d\Omega \qquad \textit{Eq. A.9}$$

Where $G_{z'_r}(\Omega)$ is defined as the road slope PSD function with units of $(m/m)^2/cycle/m$. Similarly one can define the continuous spatial acceleration PSD function shown below in equation A.10.

$$\overline{z''}^2_{\Omega_1 \to \Omega_2} = \int_{\Omega_1}^{\Omega_2} (2\pi\Omega)^4 G_{z_r}(\Omega) d\Omega$$

$$= \int_{\Omega_1}^{\Omega_2} G_{z''_r}(\Omega) d\Omega \qquad \textit{Eq. A.10}$$

Where $G_{z''_r}(\Omega)$ is the spatial acceleration PSD function with units of $(m/m^2)^2/cycle/m$.

Summarizing the results of this section, the following simple relationships may be used for obtaining the slope and spatial acceleration PSD functions from elevation PSD model:

$$G_{z_r'}(\Omega) = (2\pi\Omega)^2 G_{z_r}(\Omega)$$

$$G_{z_r''}(\Omega) = (2\pi\Omega)^4 G_{z_r}(\Omega)$$

The factor of $(2\pi\Omega)^2$ is easily identified in the slope and elevation models given by Gillespie in [*56*] and other literature [*57*], [*58*].

A.2 PSD Curves with Temporal Frequency

Defining the PSD functions in terms of the spatial frequency is suitable for characterising, comparing and modelling roads. However, spatial road models are not directly useful for modelling the ride behaviour of vehicles. The dynamic response variables of interest to ride modelling are derivatives of position with respect to time. This requires that the PSD models be found describing the road as position, velocity and acceleration inputs in the time domain.

The harmonic component in equation A.1 can be found as a function of time using the simple relationship in equation A.11 below.

$$\omega_n = \Omega_n V \qquad \textit{Eq. A.11}$$

Where ω_n is the temporal frequency in Hz, and V is the vehicle speed in m/s. The temporal harmonic component corresponding to Ω_n is then:

$$z_n(t) = Z_n \sin(2\pi\omega_n t) \qquad \textit{Eq. A.12}$$

Where Z_n is the magnitude of the harmonic component in m. Finding the mean square:

$$\overline{z_n}^2 = \omega_n \int_0^{\frac{1}{\omega_n}} [Z_n \sin(2\pi\omega_n t)]^2 \, \mathrm{d}t$$

$$= \frac{{Z_n}^2}{2} \qquad \textit{Eq. A.13}$$

The same result as equation A.2. Differentiating equation A.12 with respect to t, one obtains:

$$\frac{dz_n(t)}{dt} = \dot{z}_n(t) = 2\pi\omega_n Z_n \cos(2\pi\omega_n t) \qquad \textit{Eq. A.14}$$

Finding the mean square:

$$\overline{\dot{z}_n}^2 = \omega_n \int_0^{\frac{1}{\omega_n}} [2\pi\omega_n Z_n \cos(2\pi\omega_n t)]^2 \, dt$$

$$= (2\pi\omega_n)^2 \frac{{Z_n}^2}{2} = (2\pi\omega_n)^2 \overline{z_n}^2 \qquad \textit{Eq. A.15}$$

Similar to eq. B.4, the factor $(2\pi\omega_n)^2$ appears in front of the mean square value for the elevation function. This factor appears again following a second differentiation giving:

$$\overline{\ddot{z}_n}^2 = (2\pi\omega_n)^4 \overline{z_n}^2 \qquad \textit{Eq. A.16}$$

Now, defining the discreet PSD function, the mean square contribution of a small interval of the total bandwidth, $\Delta\omega$, is:

$$\overline{z_n}^2 = G_{z_r}(\omega_n)\Delta\omega \qquad \textit{Eq. A.17}$$

Where $G_{z_r}(\omega_n)$ is defined as the density of the mean square value in the interval. The units are reported in this work as m^2/Hz while internally the accompanying code makes use of the units $m^2/rad/s$.

The continuous spectral density function is defined as before by increasing the number of discrete harmonic frequencies towards infinity. The continuous PSD function is:

$$\bar{z}^2_{\omega_1 \to \omega_2} = \int_{\omega_1}^{\omega_2} G_{z_r}(\omega) d\omega \qquad \textit{Eq. A.18}$$

Now the velocity and acceleration PSD functions must be found. Multiplying both sides of equation A.17 by the factor $(2\pi\omega_n)^2$ one obtains:

$$\overline{\dot{z}_n}^2 = (2\pi\omega_n)^2 G_{z_r}(\omega_n)\Delta\omega \qquad \textit{Eq. A.19}$$

Letting the number of discreet frequencies increase towards infinity, one can write a different continuous function:

$$\overline{\dot{z}_r}^2_{\omega_1 \to \omega_2} = \int_{\omega_1}^{\omega_2} (2\pi\omega)^2 G_{z_r}(\omega) d\omega$$

$$= \int_{\omega_1}^{\omega_2} G_{\dot{z}_r}(\omega) d\omega \qquad \textit{Eq. A.20}$$

Where $G_{\dot{z}_r}(\omega)$ is the velocity PSD function with units of $(m/s)^2/Hz$. Similarly, the continuous spatial acceleration PSD function can be defined:

$$\overline{\ddot{z}_r}^2_{\omega_1 \to \omega_2} = \int_{\omega_1}^{\omega_2} (2\pi\omega)^2 G_{z_r}(\omega) d\omega$$

$$= \int_{\omega_1}^{\omega_2} G_{\ddot{z}_r}(\omega) d\omega \qquad \textit{Eq. A.21}$$

Where $G_{\ddot{z}_r}(\omega)$ is in units of $(m/s^2)^2/Hz$.

The following simple relationships summarize the results of this section:

$$G_{\dot{z}_r}(\omega) = (2\pi\omega)^2 G_{z_r}(\omega)$$

$$G_{\ddot{z}_r}(\omega) = (2\pi\omega)^4 G_{z_r}(\omega)$$

A.3 Converting between Temporal and Spatial PSDs

Using the results from the two previous sections, it is easy to find the relationship between the temporal and spatial PSD functions. Equating the defining equations for each of the PSD functions and using equation A.11, one easily obtains the following.

$$G_{z_r}(\omega) = \frac{1}{V} G_{z_r}(\Omega) \qquad \textit{Eq. A.22}$$

$$G_{\dot{z}_r}(\omega) = V G_{z_r'}(\Omega) \qquad \textit{Eq. A.22}$$

$$G_{\ddot{z}_r}(\omega) = V^3 G_{z_r''}(\Omega) \qquad \textit{Eq. B.22}$$

Appendix B - Comparison and Selection of Road Roughness Models and Parameters

In the literature survey conducted, numerous references were found containing road roughness models. Several different models were found which used different parameters to describe roads of different roughness levels. The three most widely used models identified were the inverse power model, the spilt power model and a model used by Gillespie.

Although all of the roads modelled in the literature are available in the computer models written for this dissertation, it was necessary to choose a few representative models from which to draw conclusions. In this appendix, each of the three most popular models is presented followed by a section explaining the selection of the roughness models for evaluating the ride motions of the proposed aerodynamic testing apparatus.

B.1 Inverse Power Model

This is the simplest model used to describe roads. It expresses that the size of the undulations in the road is inversely proportional to the spatial frequency. The equation is typically of the form in equation B.1 bellow.

$$G_{z_r}(\Omega) = C\Omega^{-w} \qquad \textit{Eq. B.1}$$

Where: G_{z_r} is the PSD of the road which is found as a function of the spacial frequency Ω. C is an empirical constant sometimes called the "unevenness index" with awkward units dependant on w (for example: $m^{3-w}/cycle^{1-w}$). Finally, w is a dimensionless constant sometimes called the "waviness index" [*59*], [*60*]. This model generates a straight line on a log-log scale plot.

B.1.1 Inverse Power Model Data

The inverse power model is used by many authors, with a wide range of parameters given to specify different roads. This is likely because it is the most basic model required to fully describe the type of random process assumed for road profiles. In table B.1 that follows, some of the parameter values found in the literature are presented. For comparison, the units have been converted for PSD curves in $m^2/cycle/m$ with the original units given for

reference. The data has then been plotted in Fig. B.1. Discussion of the data follows in the next section.

Table B.1: Parameter values for inverse power road roughness model.

No.	Road Type	Original PSD Units	C $(\frac{m^{3-w}}{cycle^{1-w}})$	w	Low Cut-off Wavenumber $(cycle/m)$	High Cut-off Wavenumber $(cycle/m)$	Ref
1	Runway (σ=0.016)	$\frac{ft^2}{cycle/ft}$	4.14×10^{-11}	3.8	1.95×10^{-2}	3.87×10^{-2}	[*61*], [*38*]
2	Smooth Highway	$\frac{ft^2}{cycle/ft}$	4.12×10^{-7}	2.1	1.36×10^{-1}	3.87×10^{-1}	[*61*], [*38*]
3	Highway with Gravel	$\frac{ft^2}{cycle/ft}$	3.78×10^{-6}	2.1	1.29×10^{-1}	1.11	[*61*], [*38*]
4	Runway 35 (NACA-TN-3305)	$\frac{ft^2}{cycle/ft}$	2.64×10^{-7}	2.1	6.49×10^{-2}	1.79×10^{-1}	[*61*]
5	Runway (σ=0.250) (NASA-TN-D-510)	$\frac{ft^2}{cycle/ft}$	6.23×10^{-7}	1.9	7.70×10^{-2}	2.52×10^{-1}	[*61*]
6	Smooth Runway (NACA-TN-3484)	$\frac{ft^2}{cycle/ft}$	2.27×10^{-6}	2.1	2.99×10^{-1}	6.66×10^{-1}	[*61*]
7	Low w	$\frac{m^2}{rad/m}$	3.99×10^{-7}	1.5	1.10×10^{-2}	2.86	[*60*]
8	ISO w	$\frac{m^2}{rad/m}$	1.59×10^{-7}	2	1.10×10^{-2}	2.86	[*60*]
9	Mean w	$\frac{m^2}{rad/m}$	6.35×10^{-8}	2.5	1.10×10^{-2}	2.86	[*60*]
10	High w	$\frac{m^2}{rad/m}$	1.01×10^{-8}	3.5	1.10×10^{-2}	2.86	[*60*]
11	Newly Laid Road (IIT data)	$\frac{m^2}{cycle/m}$	2.2×10^{-7}	2.0	1×10^{-1}	10	[*62*]
12	Smooth Road (IIT data)	$\frac{m^2}{cycle/m}$	1×10^{-6}	2.4	1×10^{-1}	10	[*62*]
13	Rough Road (IIT data)	$\frac{m^2}{cycle/m}$	4.9×10^{-6}	2.2	1×10^{-1}	10	[*62*]
14	Smooth Highway (IIT data)	$\frac{m^2}{cycle/m}$	3.5×10^{-7}	2.1	1×10^{-1}	10	[*62*]
15	PCC Road (IIT data)	$\frac{m^2}{cycle/m}$	5.5×10^{-7}	1.7	1×10^{-1}	10	[*62*]

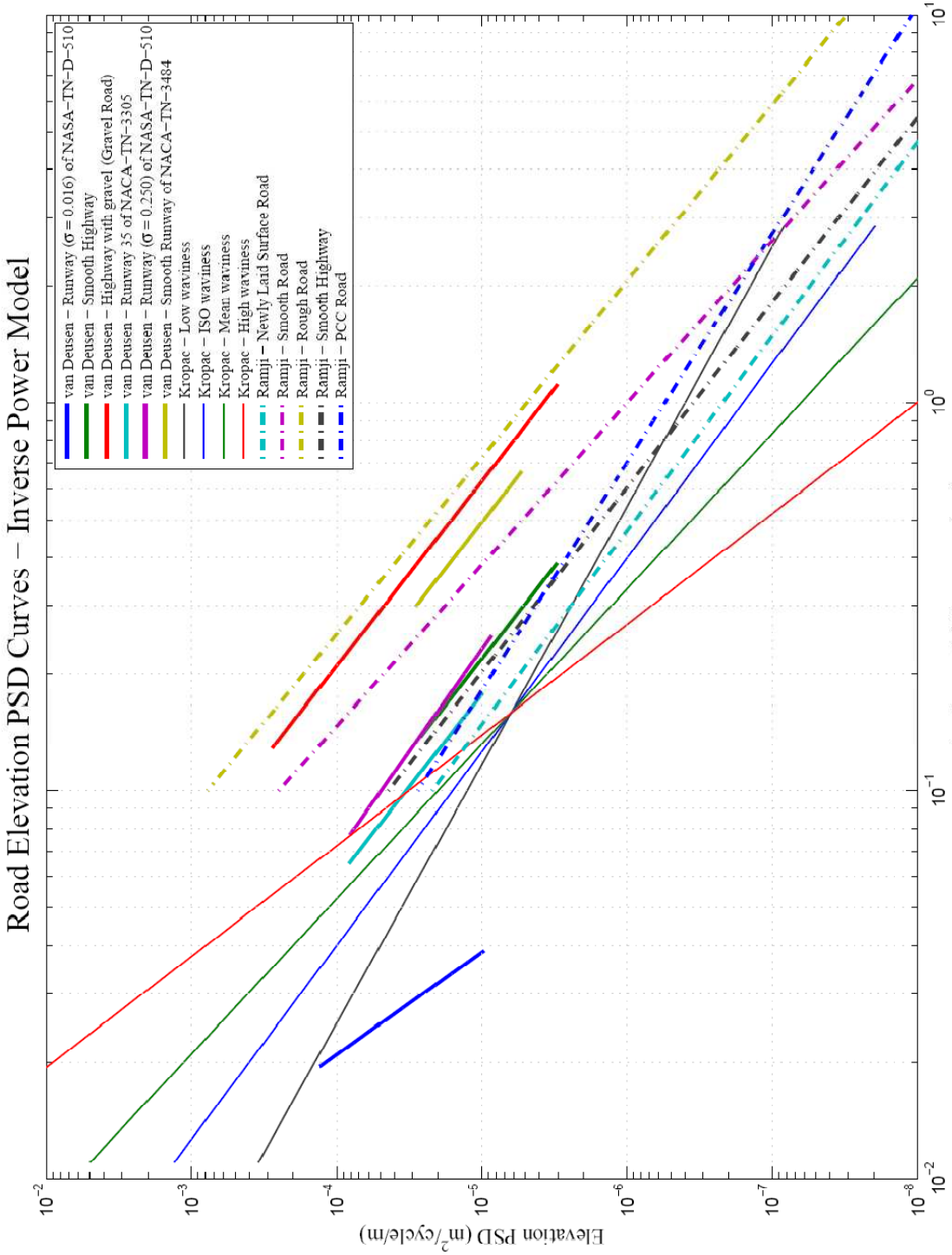

Fig B.1: Road elevation PSD curves of inverse power model data

B.1.2 Discussion of Parameter Data for the Inverse Power Model

The data presented by van Deusen [*61*] is widely quoted and covers a wide range of road and runway surfaces, bringing together road data from several sources. The data was checked against the plot presented in the text and another in Wong [*38*]. It was noticed that there was some discrepancy between the curves produced and those in the references. It was also noted that the conversion from metric to imperial units was not consistently accurate to the significant figures given. The conversion factor from $ft^{3-w}/cycle^{1-w}$ to $m^{3-w}/cycle^{1-w}$ for C is 0.3048^{3-w}. The discrepancy for roads 1 to 6 is shown in table B.2 which follows.

Table B.2: Check of unit conversion of C given by van Deusen [*61*].

No.	Road Type	w	Imperial C $(\frac{ft^{3-w}}{cycle^{1-w}})$	Metric C $(\frac{m^{3-w}}{cycle^{1-w}})$	Converted Imperial C $(\frac{m^{3-w}}{cycle^{1-w}})$	Difference $(\frac{m^{3-w}}{cycle^{1-w}})$
1	Smooth Runway	3.8	1.6×10^{-11}	4.3×10^{-11}	4.14×10^{-11}	0.16×10^{-11}
2	Smooth Highway	2.1	1.2×10^{-6}	4.8×10^{-7}	4.12×10^{-7}	0.68×10^{-7}
3	Highway with Gravel	2.1	1.1×10^{-5}	4.4×10^{-6}	3.78×10^{-6}	0.62×10^{-6}
4	Runway 35 (NACA-TN-3305)	2.1	7.7×10^{-7}	2.7×10^{-7}	2.64×10^{-7}	0.06×10^{-7}
5	Runway (σ=0.250) (NASA-TN-D-510)	1.9	2.3×10^{-6}	6.4×10^{-7}	6.23×10^{-7}	0.18×10^{-7}
6	Runway (NACA-TN-3484)	2.1	6.6×10^{-6}	2.4×10^{-6}	2.27×10^{-6}	0.14×10^{-6}

PSD curves calculated from the quoted data for roads 1 to 3 were overlaid on the plot given in Wong in an effort to determine if the error was in the application of the conversion factor or in plotting. An improved fit which closely matched the curves in both units was also plotted and overlaid. The plots are shown below in Fig. B.1 and the parameters used are given in table B.3. Note that in the original plot from Wong, the lines labelled “Smooth Runway” refer to road number 1 in table B.1 and those labelled “Gravel Road” refer to number 3.

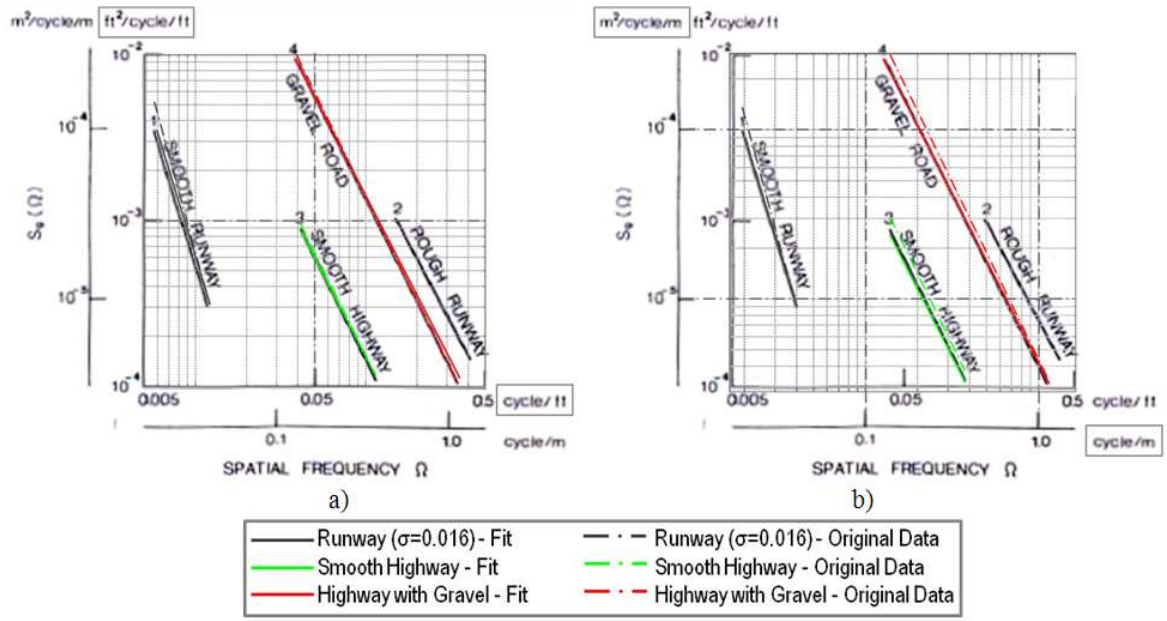

Fig B.2: PSD curves using metric, imperial parameters overlaid on figure extracted from Wong [*38*] with fit. a) Imperial units b) Metric units

Table B.3: Parameters used in Fig. B.1

No.	Road Type	w	w_{Fit}	C $(\frac{ft^{3-w}}{cycle^{1-w}})$	C_{Fit} $(\frac{ft^{3-w}}{cycle^{1-w}})$	C $(\frac{m^{3-w}}{cycle^{1-w}})$	C_{Fit} $(\frac{m^{3-w}}{cycle^{1-w}})$
1	Smooth Runway	3.8	3.32	1.6×10^{-11}	1.36×10^{-10}	4.3×10^{-11}	2.00×10^{-10}
2	Smooth Highway	2.1	2	1.2×10^{-6}	1.51×10^{-6}	4.8×10^{-7}	4.6×10^{-7}
3	Highway with Gravel	2.1	2	1.1×10^{-5}	1.39×10^{-5}	4.4×10^{-6}	4.25×10^{-6}

Closer agreement between the fit and the imperial units than to the metric units was noted. This, and the fact that the original work favoured imperial units, indicated that there was poor accuracy in the conversion to metric units. Poor agreement in both cases for the smooth runway plot also indicated that plotting accuracy contributed to the confusion. It was therefore decided to use the quoted values for $ft^2/cycle/m$ and convert to other units rather than use the metric values given. There is some concern about the accuracy of frequency bands measured off the plots, however, these values are not quoted in either of the cited works.

The papers of Kropáč and Múčka [*59*] [*60*] [*63*] focus on the waviness parameter, w, of the road model. It is argued that using the IRI alone does not account for the significant difference that the waviness parameter has on the shape of the road. Although the waviness parameter is often assumed to be 2, it was found to have a range of values varying from 1.5 to

3.5 with a mean value of 2.5. The unevenness index, C, used in the study of w was $1 \times 10^{-6}\, m^{3-w}/rad^{1-w}$.

For roads 7 through 10 in table B.1, the original PSD units used were $m^2/rad/m$. The units of radians per meter are useful since multiplying with speed gives the frequency in radians per second which can then be used directly in the sinusoidal components of the road without conversion. The paper is also the most recent reference quoted in this work which may suggest a change in the favoured units in the field. The units of cycles per meter on the other hand are more easily visualised. For the purposes of comparison, the units of C in table B.1 were converted from m^{3-w}/rad^{1-w} to $m^{3-w}/cycle^{1-w}$ by multiplying by $1/(2\pi)^{1-w}$. In the road data function file written for the ride models, the units are all entered in the units of the original sources and then converted to $m^2/rad/m$ and rad/m . They are later converted to a desired set of units.

Ramji, et al [*62*] conducted their testing at the Indian Institute of Technology (IIT) in Roorkee, India. They compare data obtained in their tests to data from other sources given in table B.1. Road 11 is compared to road 4, 12 to 6, 13 to 3, 14 to 2 and 15 to 5. The equipment and experimental procedure described in the text lead a bandwidth of approximately $0.1 cycles/m$ to $10\, cycles/m$. This is somewhat different to the bandwidth used in the compared roads.

B.2 Split Power Model

The split power type is similar to the inverse power type but characterises the road in two bands divided at a reference wavenumber. The piece-wise model is given in equation B.2 as presented by Dodds and Robson [*37*].

$$G_{z_r}(\Omega) = \begin{cases} G_{z_r}(\Omega_0)\left(\dfrac{\Omega}{\Omega_0}\right)^{-w_1}, & \Omega \le \Omega_0 \\ G_{z_r}(\Omega_0)\left(\dfrac{\Omega}{\Omega_0}\right)^{-w_2}, & \Omega \ge \Omega_0 \end{cases} \qquad \textit{Ref. [37]} \quad \textit{Eq. B.2}$$

In the above equation: G_{z_r} is the PSD of the road which is found as a function of the spacial frequency Ω. Ω_0 is the datum wavenumber and the constant $G_{z_r}(\Omega_0)$ is the elevation PSD value at the datum wave number, equivalent to the unevenness index, C, in the inverse power

model. Dimensionless constants w_1 and w_2 determine the slope of the two parts of the curve in log-log axes and are equivalent to the waviness index.

B.2.1 Split Power Model Data

The parameters for the split power model given by Dodds and Robson [*37*] are shown in table A.4. The datum wavenumber (Ω_0) is $1/2\pi\ cycles/m$.

Table B.4: Parameters for the split power model given by Dodds and Robson [*37*].

Road Class		$G_{z_r}(\Omega_0)$ Range 10^{-6} m^3/cycle	w_1		w_2	
			Mean	**Standard Deviation**	**Mean**	**Standard Deviation**
Motorways	Very Good	2-8	1.945	0.464	1.360	0.221
	Good	8-32				
Principal roads	Very Good	2-8	2.05	0.487	1.440	0.266
	Good	8-32				
	Average	32-128				
	Poor	128-512				
Minor roads	Average	32-128	2.28	0.534	1.428	0.263
	Poor	128-512				
	Very Poor	512-2048				

The literature [[*64*], [*65*], [*66*]] indicates that this classification system was later developed in to the standard proposed by ISO (ISO 8608 [*67*]); with constants w_1 and w_2 equal to 2 and 1.5 respectively and a wavelength band from 100 m to 0.1 m. Roads are classed using the values for $G_{z_r}(\Omega_0)$ above with letters from A being very good to E being very poor, with further rougher classifications up to H. These are plotted in Fig. B.3.

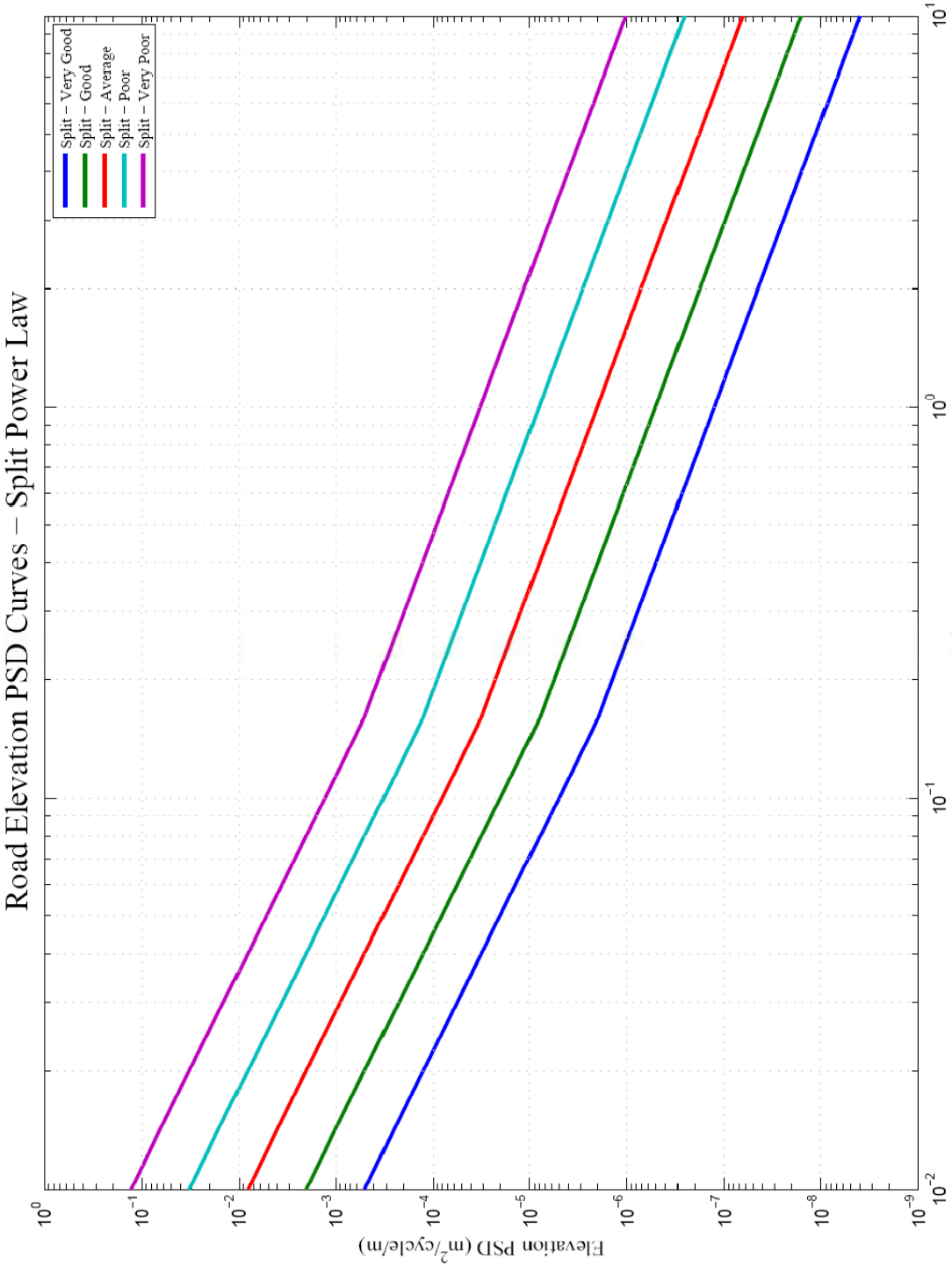

Fig B.3: Road elevation PSD curves of split power model data

B.3 Gillespie Model

T.D. Gillespie is a well known author in the field of road roughness, in particular for his work in developing the IRI. In his text [*35*] he presents a rational function to describe road roughness which is given below in equation B.3.

$$G_{z_r}(\Omega) = G_0 \frac{1 + \left(\frac{\Omega_c}{\Omega}\right)^2}{(2\pi\Omega)^2} \qquad \textit{Ref. [35]} \quad \textit{Eq. B.3}$$

Where: G_{z_r} is the PSD of the road which is found as a function of the spacial frequency Ω. Ω_c Is the cut-off wavenumber. G_0 is termed the roughness magnitude parameter and is equivalent to the unevenness index, C, in the inverse power model. This model is referred to in this work as the Gillespie model or Gillespie type.

B.3.1 Gillespie Model Data

In table B.5 the parameters given by Gillespie are presented. The wavenumber range given in the text is 0.005 $cycles/ft$ to 0.5 $cycles/ft$

Table B.5: Parameters suggested by Gillespie [*35*]

	Road Type	**Value**	**Units**
G_0	Rough Roads	1.25×10^{-5}	$ft.cycle$
	Smooth Roads	1.25×10^{-6}	$ft.cycle$
Ω_c	Bituminous Roads	0.05	$cycles/ft$
	PCC Roads	0.02	$cycles/ft$

On comparing the data above to the data presented in the figures given by Gillespie in [*35*] and [*56*] it was noted that the "Average Bituminous" line plotted corresponded to the parameters for a rough bituminous road given in table B.5. The "Average PCC" road corresponded to the cut-off wavenumber given above, but with the roughness magnitude parameter, G_0, equal to $2.15 \times 10^{-5}\ ft.cycle$, a higher value than that given for rough roads. The permutations of table B.5 with the "Average PCC" line are plotted in Fig. B.4.

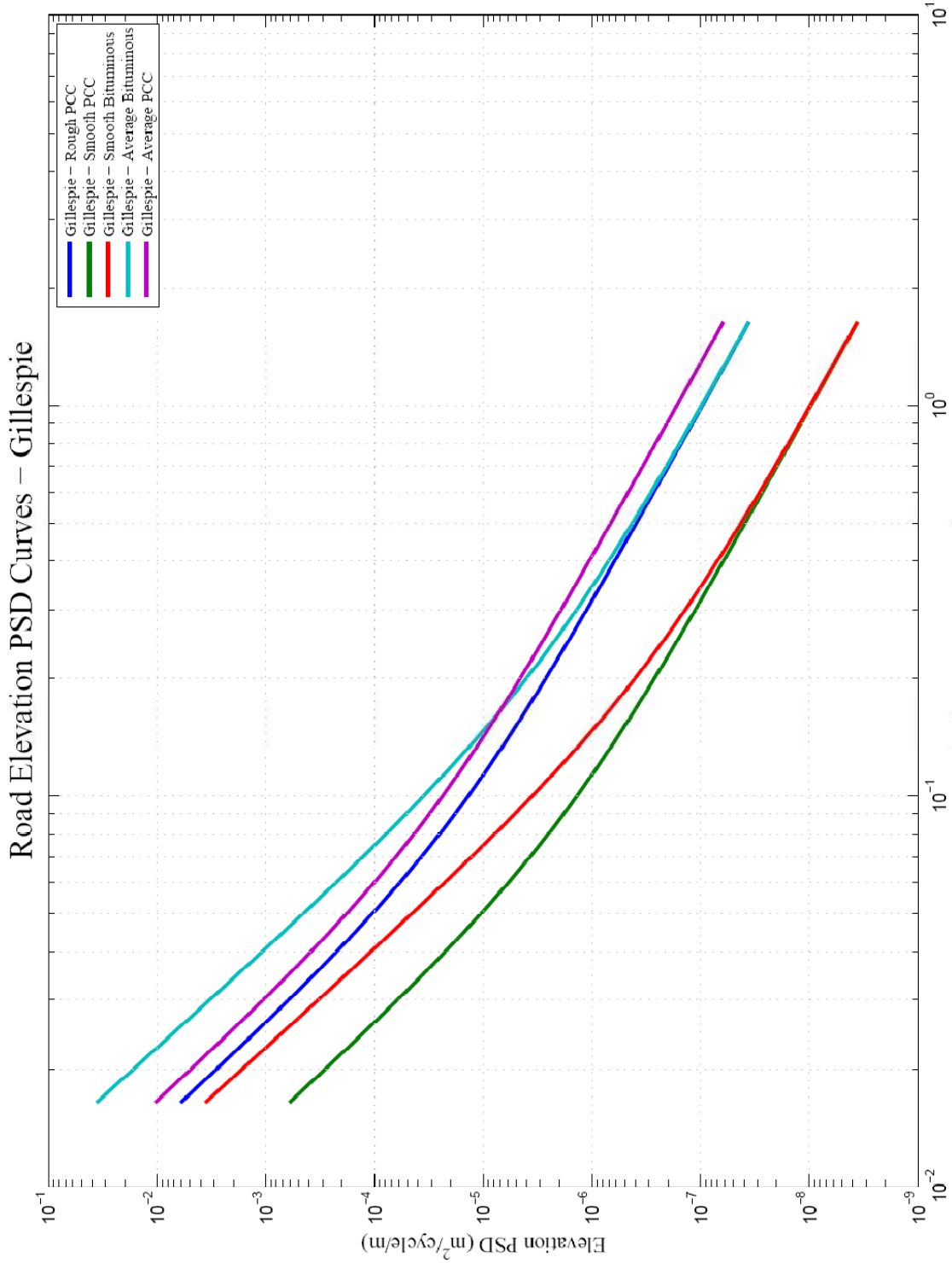

Fig B.4: Road elevation PSD curves of Gillespie model data

B.4 Selecting Representative Road Roughness Models

The road roughness models presented in this chapter are all valid approximate representations of different types of roads and runways. Therefore all of the models have been made available for modelling and simulation. However, in order to draw conclusions about the displacements and accelerations that may occur in the proposed system, models representing a rough, smooth and intermediate road were required. The wide variation of the models presented a problem when deciding which model to select.

The work of van Deusen, Dodds and Robson, and Gillespie are the most widely referenced and are focussed specifically of developing road models. It was decided to limit selection to the models and parameters given by those three authors. The models are plotted on the same axes in Fig. B.5 below for comparison.

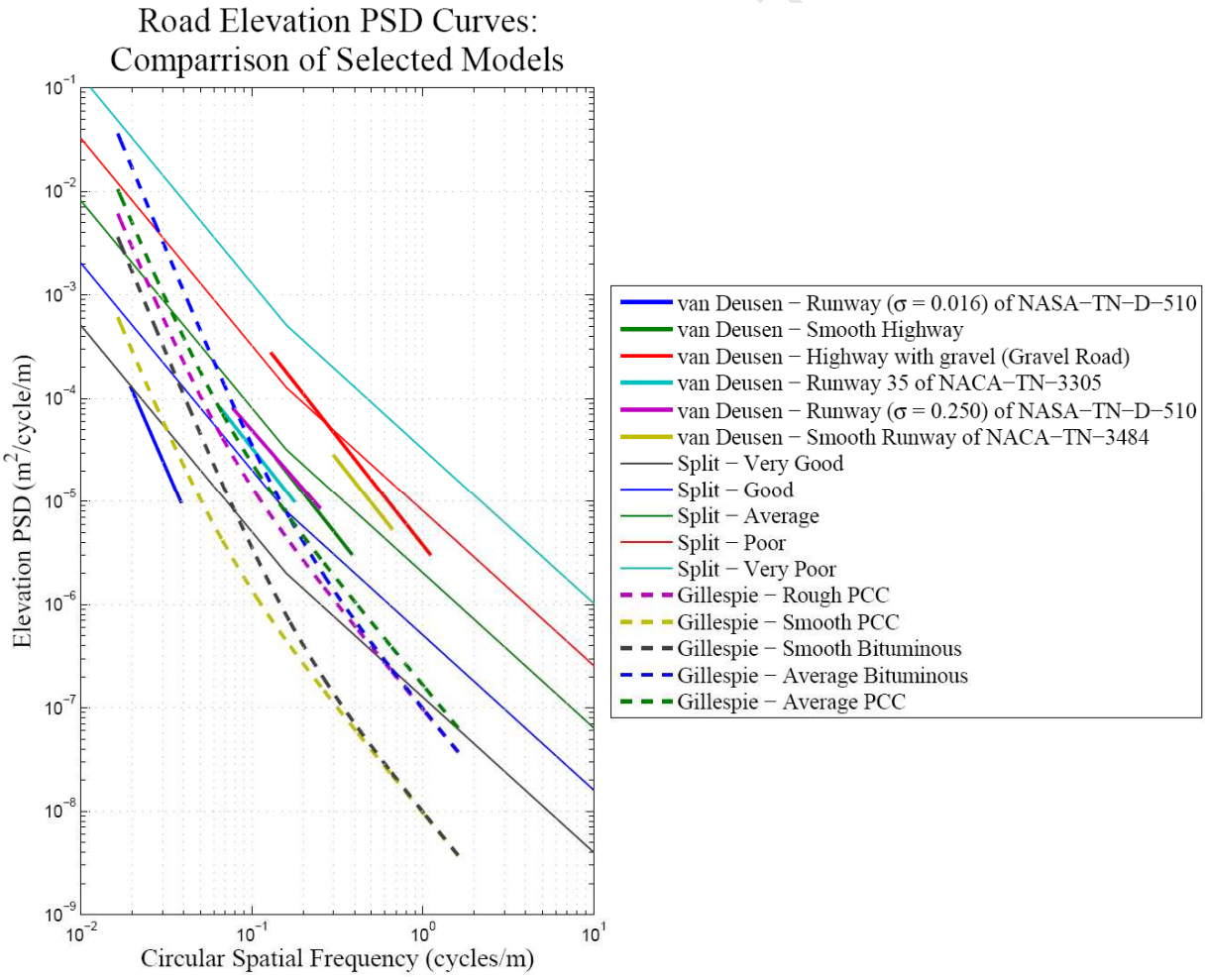

Fig B.5: Comparison of selected road roughness models

The models given by Gillespie appear to describe generally smoother roads than the rest of the models, giving lower values for the spectral density except at low wavenumbers. The data from van Deusen are based on measurements of specific runways and roads over limited bandwidths. This makes them suitable for comparison but not general enough for benchmark cases. It was decided that the split power models of Dodds and Robson, as used in the current ISO standard, represented the best models to be used for the modelling of the output responses of the system. The “very good”, “good” and “average” data have been selected as representing appropriate roads.

B.5 Notes on the Bandwidth of Road Models

Importantly it has been noted that the frequency band over which the models are applicable is limited. The selection of the wavenumber limits are guided by the minimum and maximum frequencies likely to affect passenger perception of ride. These are then used to determine the sampling rate for the road measurement system or method. The models used here will therefore not completely describe the spectrum of vibrations transmitted to the measurement system from the road.

These unaccounted for vibrations have been ignored for the current work. This is acceptable since the very high frequency vibrations excluded from these models will be very small and will ultimately be influenced by other noise sources. These may be filtered out from the data. Very low frequencies with wavelengths longer than 100m should have limited effect on the angle of attack of the vehicle to the relative wind, due to their slow speed.

Appendix C - Vehicle Ride Models

In this appendix, detailed derivations of the vehicle ride models are presented. The appendix is split into two parts dealing first with the quarter car, and then the pitch-bounce models. The appendix is concise and intended to separate the mathematical detail from section 4.3.

C.1 Quarter Car Model

Fig C.1 shows the free body diagram and axis definitions described in section 4.3.

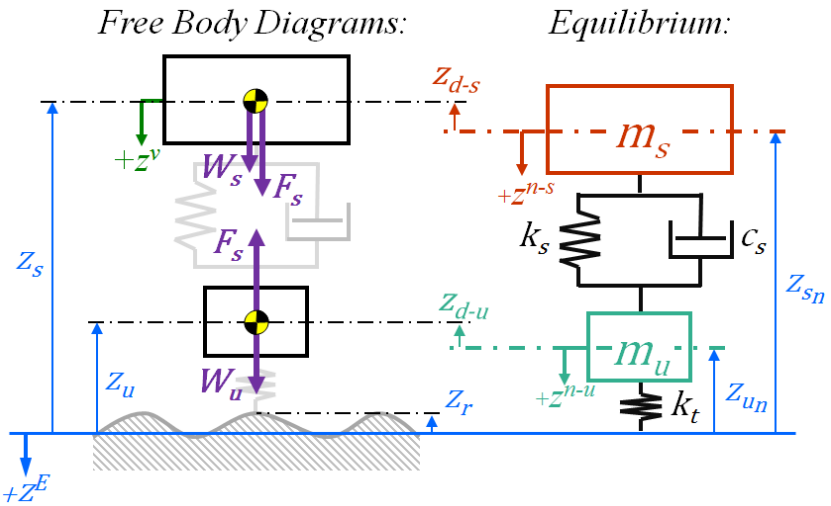

Fig C.1: Free body diagrams for quarter car model with model definitions

From this diagram, we can write two equations by applying Newton's second law to each of the masses. This gives the results shown in equations C.1 and C.2 below where z_{fl-s} is the free length of the suspension spring and z_{fl-t} is the free length of the tyre spring.

$$m_s\ddot{z}_s(t) = k_s\big(z_u(t) - z_s(t) - z_{fl-s}\big) + c_s(\dot{z}_u(t) - \dot{z}_s(t)) + m_s g \qquad \textit{Eq. C.1}$$

$$m_u\ddot{z}_u(t) = -k_s\big(z_u(t) - z_s(t) - z_{fl-s}\big) - c_s(\dot{z}_u(t) - \dot{z}_s(t)) - k_t\big(z_u(t) - z_r(t) - z_{fl-t}\big) + m_u g \qquad \textit{Eq. C.2}$$

Isolating the part of these equations which vary with time one obtains:

$$m_s\ddot{z}_{d-s}(t) = k_s(z_{d-u}(t) - z_{d-s}(t)) + c_s(\dot{z}_{d-u}(t) - \dot{z}_{d-s}(t)) \qquad \textit{Eq. C.3}$$

$$m_u\ddot{z}_{d-u}(t) = -k_s(z_{d-u}(t) - z_{d-s}(t)) - c_s(\dot{z}_{d-u}(t) - \dot{z}_{d-s}(t)) - k_t(z_{d-u}(t) - z_r(t)) \qquad \textit{Eq. C.4}$$

With zero initial conditions, the Laplace transforms of the LTI systems are then simply:

$$m_s s^2 \mathrm{z}_{d-s}(s) = k_s(z_{d-u}(s) - z_{d-s}(s)) + sc_s(\mathrm{z}_{d-u}(s) - \mathrm{z}_{d-s}(s)) \qquad \textit{Eq. C.5}$$

$$m_u s^2 \mathrm{z}_{d-u}(s) = -k_s(z_{d-u}(s) - z_{d-s}(s)) - sc_s(\mathrm{z}_{d-u}(s) - \mathrm{z}_{d-s}(s)) - k_t(z_{d-u}(s) - z_r(s)) \qquad \textit{Eq. C.6}$$

Rearranging one obtains:

$$\mathrm{z}_{d-s}(s)(m_s s^2 + sc_s + k_s) = \mathrm{z}_{d-u}(s)(sc_s + k_s) \qquad \textit{Eq. C.7}$$

$$\mathrm{z}_{d-u}(s)(m_u s^2 + sc_s + k_s + k_t) = \mathrm{z}_{d-s}(s)(sc_s + k_s) + \mathrm{z}_r(s)(k_t) \qquad \textit{Eq. C.8}$$

Now substituting C.7 into C.8 and simplifying one obtains the transfer functions, $G_{u/r}(s)$ and $G_{s/r}(s)$ shown in C.9 and C.10.

$$H_{u/r}(s) = \frac{z_{d-u}(s)}{z_r(s)} = \frac{m_s k_t(s)^2 + c_s k_t(s) + k_s k_t}{m_u m_s(s)^4 + (m_u + m_s)c_s(s)^3 + [(m_u + m_s)k_s + m_s k_t](s)^2 + c_s k_t(s) + k_s k_t} \qquad \textit{Eq. C.9}$$

$$H_{s/r}(s) = \frac{z_{d-s}(s)}{z_r(s)} = \frac{c_s k_t(s) + k_s k_t}{m_u m_s(s)^4 + (m_u + m_s)c_s(s)^3 + [(m_u + m_s)k_s + m_s k_t](s)^2 + c_s k_t(s) + k_s k_t} \qquad \textit{Eq. C.10}$$

Since this is an LTI system, the frequency transfer functions are found by making $s = j\omega$ giving the final results in C.11 and C.12 below.

$$H_{u/r}(j\omega) = \frac{z_{d-u}(j\omega)}{z_r(j\omega)} = \frac{m_s k_t(j\omega)^2 + c_s k_t(j\omega) + k_s k_t}{m_u m_s(j\omega)^4 + (m_u + m_s)c_s(j\omega)^3 + [(m_u + m_s)k_s + m_s k_t](j\omega)^2 + c_s k_t(j\omega) + k_s k_t} \qquad \textit{Eq. C.11}$$

$$H_{s/r}(j\omega) = \frac{z_{d-s}(j\omega)}{z_r(j\omega)} = \frac{c_s k_t(j\omega) + k_s k_t}{m_u m_s(j\omega)^4 + (m_u + m_s)c_s(j\omega)^3 + [(m_u + m_s)k_s + m_s k_t](j\omega)^2 + c_s k_t(j\omega) + k_s k_t} \qquad \textit{Eq. C.12}$$

C.2 Pitch-Bounce Model

As with the previous section, Fig. C.2 shows the free body diagram of the system along with the axis definitions described in section 4.3.

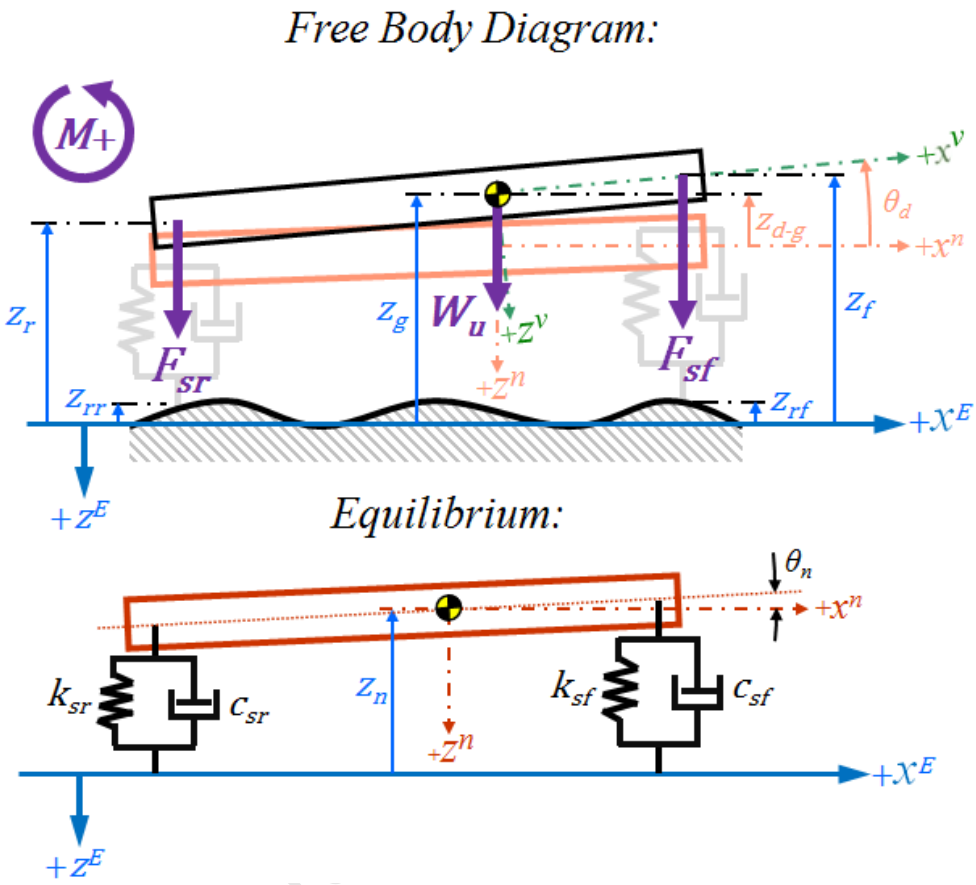

Fig C.2: Free body diagrams for pitch-bounce model with model definitions

From this diagram, we can again write two equations by applying Newton's second law but this time for the pitch and bounce motions. This gives the results shown in equations C.13 and C.14 below. Here the symbols are as defined in the figures above with z_{fl-f} equal to the free length of the front suspension spring and z_{fl-r} the free length of the rear.

$$m\ddot{z}_g(t) = k_f\left(z_{rf}(t) - z_g(t) + l_f\theta(t) - z_{fl-f}\right) + c_f\left(\dot{z}_{rf}(t) - \dot{z}_g(t) + l_f\dot{\theta}(t)\right) + k_r\left(z_{rr}(t) - z_g(t) - l_r\theta(t) - z_{fl-r}\right) + c_r\left(\dot{z}_{rr}(t) - \dot{z}_g(t) + l_r\dot{\theta}(t)\right) + mg \qquad \textit{Eq. C.13}$$

$$I_y\ddot{\theta}(t) = -l_f\left[k_f\left(z_{rf}(t) - z_g(t) + l_f\theta(t) - z_{fl-f}\right) + c_f\left(\dot{z}_{rf}(t) - \dot{z}_g(t) + l_f\dot{\theta}(t)\right)\right] + l_r\left[\left[k_r\left(z_{rr}(t) - z_g(t) - l_r\theta(t) - z_{fl-r}\right) + c_r\left(\dot{z}_{rr}(t) - \dot{z}_g(t) + l_r\dot{\theta}(t)\right)\right]\right] \qquad \textit{Eq. C.14}$$

Taking the dynamic part of these equations:

$$m\ddot{z}_{d-g}(t) = k_f\left(z_{rf}(t) - z_{d-g}(t) + l_f\theta_d(t)\right) + c_f\left(\dot{z}_{rf}(t) - \dot{z}_{d-g}(t) + l_f\dot{\theta}_d(t)\right) + k_r\left(z_{rr}(t) - z_{d-g}(t) - l_r\theta_d(t)\right) + c_r\left(\dot{z}_{rr}(t) - \dot{z}_{d-g}(t) + l_r\dot{\theta}_d(t)\right) \quad \textit{Eq. C.15}$$

$$I_y\ddot{\theta}_d(t) = -l_f\left[k_f\left(z_{rf}(t) - z_{d-g}(t) + l_f\theta_d(t)\right) + c_f\left(\dot{z}_{rf}(t) - \dot{z}_{d-g}(t) + l_f\dot{\theta}_d(t)\right)\right] + l_r\left[\left[k_r\left(z_{rr}(t) - z_g(t) - l_r\theta_d(t)\right) + c_r\left(\dot{z}_{rr}(t) - \dot{z}_{d-g}(t) + l_r\dot{\theta}_d(t)\right)\right]\right] \quad \textit{Eq. C.16}$$

The Laplace transforms of the LTI systems are then:

$$ms^2z_{d-g}(s) = k_f\left(z_{rf}(s) - z_{d-g}(s) + l_f\theta_d(s)\right) + sc_f\left(z_{rf}(s) - z_{d-g}(s) + l_f\theta_d(s)\right) + k_r\left(z_{rr}(s) - z_{d-g}(s) - l_r\theta_d(s)\right) + sc_r\left(z_{rr}(s) - z_{d-g}(s) + l_r\theta_d(s)\right) \quad \textit{Eq. C.17}$$

$$I_ys^2\theta_d(s) = -l_f\left[k_f\left(z_{rf}(s) - z_{d-g}(s) + l_f\theta_d(s)\right) + sc_f\left(z_{rf}(s) - z_{d-g}(s) + l_f\theta_d(s)\right)\right] + l_r\left[\left[k_r\left(z_{rr}(s) - z_g(s) - l_r\theta_d(s)\right) + sc_r\left(z_{rr}(s) - z_{d-g}(s) + l_r\theta_d(s)\right)\right]\right] \quad \textit{Eq. C.18}$$

This is a linear system with two inputs, $z_{rf}(s)$ and $z_{rr}(s)$. However, the relationship between these two inputs is known. The rear road signal is simply a time delayed repeat of the road input to the front wheels found using equation C.19

$$z_{rr}(t) = z_{rf}(t + \tau) \quad \textit{Eq. C.19}$$

where:

$$\tau = \frac{\mathrm{L}}{\mathrm{V}}$$

The Laplace transform of this delay is:

$$z_{rr}(s) = e^{-s\tau}z_{rf}(s) \quad \textit{Eq. C.20}$$

Since the relationship between the inputs is known, one could use this to find the required transfer functions. This approach would require more laborious mathematics to solve. Instead, owing to the linearity of the system, one can separate the equations above into two sets. One for the response of the system to the front road input and one for the response of the system to the rear input. The response of the system is then the sum of the responses to each set of wheels. One can then substitute the relationship between the two inputs (the time delay of τ).

After executing this procedure, one is left with the following:

$$H_{z/r}(s) = \frac{z_{d-g}(s)}{z_r(s)}$$

Eq. C.21

$$= \frac{F(s)^3+G(s)^2+H(s)+I}{A(s)^4+B(s)^3+C(s)^2+D(s)+E} + e^{-s\tau}\left(\frac{N(s)^3+O(s)^2+P(s)+Q}{A(s)^4+B(s)^3+C(s)^2+D(s)+E}\right)$$

$$H_{\theta/r}(s) = \frac{\theta_d(s)}{z_r(s)}$$

Eq. C.22

$$= \frac{J(s)^3+K(s)^2+L(s)+M}{A(s)^4+B(s)^3+C(s)^2+D(s)+E} + e^{-s\tau}\left(\frac{R(s)^3+S(s)^2+T(s)+U}{A(s)^4+B(s)^3+C(s)^2+D(s)+E}\right)$$

Where in the above equations:

$$A = mI_y$$
$$B = m\left(c_f {l_f}^2 + c_r {l_r}^2\right) + I_y(c_f + c_r)$$
$$C = m\left({l_f}^2 k_f + {l_r}^2 k_r\right) + I_y\left(k_f + k_r\right) + c_f c_r\left(l_f + l_r\right)^2$$
$$D = \left(c_f k_r + c_r k_f\right)\left(l_f + l_r\right)^2$$
$$E = k_f k_r\left(l_f + l_r\right)^2$$
$$F = I_y c_f$$
$$G = I_y k_f + c_f c_r\left({l_r}^2 + l_f l_r\right)$$
$$H = \left(c_f k_r + c_r k_f\right)\left({l_r}^2 + l_f l_r\right)$$
$$I = k_f k_r\left({l_r}^2 + l_f l_r\right)$$
$$J = -mc_f l_f$$
$$K = -c_f c_r\left(l_f + l_r\right) - ml_f k_f$$
$$L = -\left(c_f k_r + c_r k_f\right)\left(l_f + l_r\right)$$
$$M = -k_f k_r\left(l_f + l_r\right)$$
$$N = I_y c_r$$
$$O = I_y k_r + c_f c_r\left({l_f}^2 + l_f l_r\right)$$
$$P = \left(c_f k_r + c_r k_f\right)\left({l_f}^2 + l_f l_r\right)$$
$$Q = k_f k_r\left({l_f}^2 + l_f l_r\right)$$
$$R = mc_r l_r$$
$$S = c_f c_r\left(l_f + l_r\right) + ml_r k_r$$
$$T = \left(c_f k_r + c_r k_f\right)\left(l_f + l_r\right)$$
$$U = k_f k_r\left(l_f + l_r\right)$$

The frequency transfer functions then found by making $s = j\omega$ giving the final results in C.23 and C.24 below.

$$\frac{z_{d-g}(j\omega)}{z_r(j\omega)} = H_{z/r}(j\omega)$$

Eq. C.23

$$= \frac{F(j\omega)^3+G(j\omega)^2+H(j\omega)+I}{A(j\omega)^4+B(j\omega)^3+C(j\omega)^2+D(j\omega)+E} + e^{-\tau(j\omega)}\left(\frac{N(j\omega)^3+O(j\omega)^2+P(j\omega)+Q}{A(j\omega)^4+B(j\omega)^3+C(j\omega)^2+D(j\omega)+E}\right)$$

$$H_{\theta/r}(j\omega) = \frac{\theta_d(j\omega)}{z_r(j\omega)}$$

Eq. C.24

$$= \frac{J(j\omega)^3+K(j\omega)^2+L(j\omega)+M}{A(j\omega)^4+B(j\omega)^3+C(j\omega)^2+D(j\omega)+E} + e^{-\tau(j\omega)}\left(\frac{R(j\omega)^3+S(j\omega)^2+T(j\omega)+U}{A(j\omega)^4+B(j\omega)^3+C(j\omega)^2+D(j\omega)+E}\right)$$

Appendix D - SIMULINK Simulation Models

Two models were created to simulate a time domain response of the two models presented in Chapter 4. These were the pitch bounce model and the quarter car model. The models both use an input generator which can be used to input a number of useful inputs including a random road generator. This is input to a dynamic model of the system structured in the same way as the block diagrams presented. The transfer function blocks also provided a means to check the transfer functions obtained in appendix C against the block diagrams. The outputs are plotted and also animated. In this section, the input generator is described before the two models are presented.

D.1 Input Generator

The desired input specified by the `rspec` variable in the input cell of the m-file of the simulation models. The input is in the form of a binary sequence which controls a set of switches which direct the correct input signal from a number of signal generators in the model. The available inputs are presented in table D.1.

Table D.1: Available input signals

Input	`rspec`	Description
Random Road Generator	1101000	Random road calculated from a selected road model
Ramp	1100000	Constant slope ramp signal
Saw Tooth	1000100	Discontinuous saw tooth signal
Square Wave	1000000	Discontinuous square wave signal
Bump	0010010	Smooth sinusoidal pulse signal
Chirp	0010000	Chirp signal
Signal Builder	0000001	SIMULINK Signal builder block
Step	0000000	Step input

Parameters for changing each of the signals may be edited. All of the above signals were used to check the correct implementation of the model bar the random road generator.

It was noted that the discrepancy between the outputs obtained from the model and the transfer function blocks was insignificant except when discontinuous signals were used. This

discrepancy was larger for the pitch bounce model than for the quarter car model. This is likely due to the fact that for the pitch bounce model, the road input signal must be differentiable in order to find the damping force generated, whereas in the quarter car model the tyre damping has been neglected. This meant that numerical errors occurred at the discontinuities. This was an additional justification for the method used to generate the random road, rather than using the filtered white noise approach. For the reasons mentioned here the road signal is also attenuated to zero first and smoothly increased to unity gain in order for the signal to remain smooth.

The random road generator consists of 100 individual sine wave generators which are each assigned an amplitude and frequency determined by the method described in Chapter 4. This method of generating the road signal was laborious to implement as each sine wave generator had to be individually assigned to an element of the frequency vector. While having the number of harmonic components limited because of this is not ideal, the logarithmic distribution of the frequency bands used to find the signal has resulted in a very reasonable representation of a road signal. It has been recommended that a better method of implementing the generator be found.

D.2 Quarter Car Model

The SIMULINK model for the quarter car model is shown below in Fig. D.1. Colour coding is used to more easily identify the signals related to dynamics of the sprung and unsprung masses.

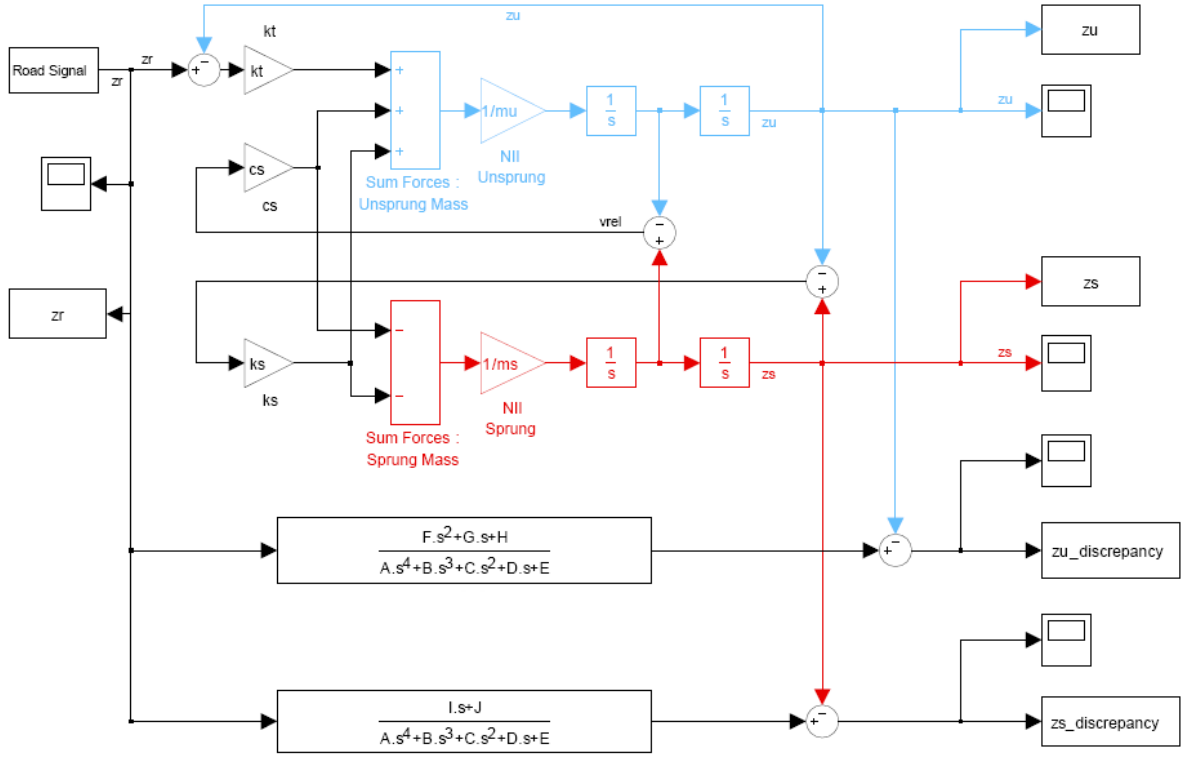

Fig D.1: SIMULINK model for the quarter car vehicle model

D.3 Pitch-Bounce Model

The SIMULINK model for the pitch-bounce model is shown below in Fig. D.2. Colour coding is again used to more easily identify the signals related to dynamics of the pitch and bounce motions as well as to clarify the numerous signals.

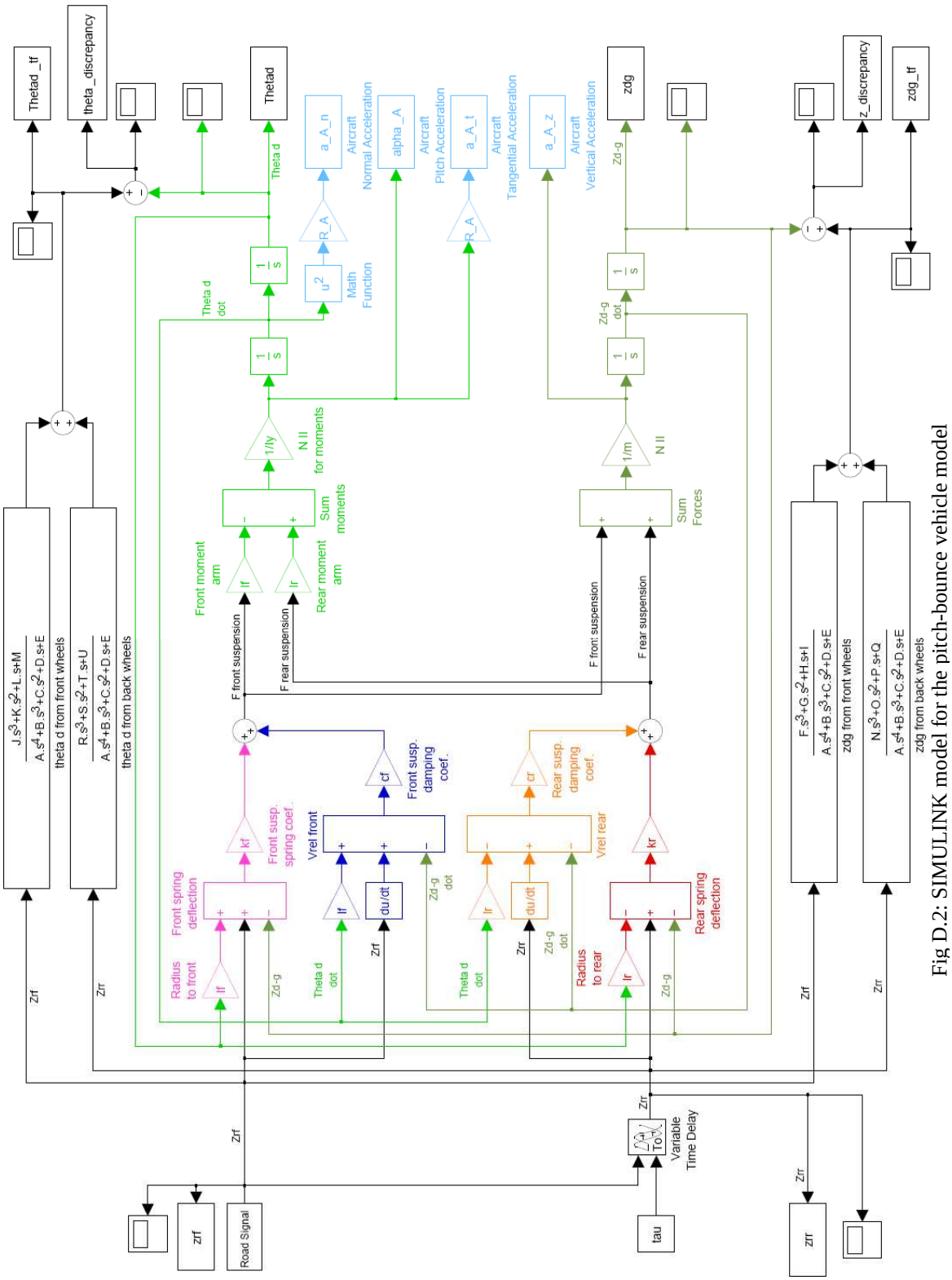

Fig D.2: SIMULINK model for the pitch-bounce vehicle model

Appendix E Development, Verification and Limitations of Axisymmetric Line-Source Potential Flow Methods

In this chapter the basic formulation of the axisymmetric potential flow methods used in this work are described. Owing to the basic, drawn out nature of the derivations of these methods, the important equations have been quoted rather than derived in full here. This chapter mainly focuses on the procedures used to verify the methods, and the sensitivities of the method to various input parameters.

E.1 Formulation of the Axisymmetric Potential Flow Methods

The technique used for finding the potential flow about a general axisymmetric body is identical to the original technique used by von Karman [*49*] for finding the flow around airships over 80 years ago. The formulation of the problem defines a number of constant strength line sources in a set of linear equations as described by Shames [*54*].

The stream function contribution, $\Delta\psi$, at a control point on the body profile, n, from a single constant strength line source, m, is found according to equation E.1 below where $'k_{nm}$ is the distance from the left hand side of the line source to the control point and k'_{nm} is the distance from the right.

$$\Delta\psi_{nm} = -\frac{\eta_m}{4\pi}('k_{nm} - k'_{nm}) \qquad \textit{Ref. [54]} \quad \textit{Eq. E.1}$$

The summation of all m line sources at control point n gives the total stream function at this point. Setting the stream function to zero at each control point forces the streamline following the axis of symmetry to pass through the control point. If the number of control points is equal to the number of line sources, f, then performing this summation for all the control points leads to a set of f simultaneous equations with f unknowns. This can be solved using standard linear algebra.

With the solution for the flow found the stream function may be calculated at any point in the flow field. Drawing contour lines for constant values of stream function the streamlines are

obtained. If the spacing between streamlines is to be even the constants must increase with a power of 2 as the spacing is determined by the flow rate through stream tubes.

The equations for the velocity components in the spherical coordinate system were found by taking derivatives according to equations E.2 and E.3 below.

$$V_R = \frac{1}{R^2 sin\beta}\frac{\partial \psi}{\partial \beta} \qquad \textit{Ref. [54]} \quad \textit{Eq. E.2}$$

$$V_\beta = -\frac{1}{Rsin\beta}\frac{\partial \psi}{\partial R} \qquad \textit{Ref. [54]} \quad \textit{Eq. E.3}$$

The differentiation is simple and the result was incorporated into the accompanying code.

The formulation of the linearly varying line source method is very similar to the linear method described above, except the strength distribution is no longer defined by the single parameter η_m, but is defined by two parameters giving the strength at either end of the line source. The strength at points where the adjacent line sources meet is assigned the same value so that there is no sudden change in magnitude along the singularity distribution.

The formulation described in Zedan and Dalton [*68*] was implemented identically where the velocity potential and stream function have both been defined in terms of parameters provided. An additional problem occurs in the formulation of the simultaneous equations for the linearly varying sources. Since each line source, m, requires two strength parameters, q_{1m} and q_{2m}, but the parameters at the junctions of the source lines are equal (i.e. $q_{2m} = q_{2m+1}$), the number of unknowns is equal to the number of sources, f, plus one. An additional equation is therefore required to solve for the unknowns. This is found by imposing a closure condition on the system. Stated simply, the total number of line sources, f, the total volume contribution to the flow must be zero. For panels of equal length this results in equation E.4 below.

$$\sum_{m=1}^{f} \frac{q_{1m} + q_{2m}}{2} = 0 \qquad \textit{Eq. E.4}$$

There were no significant hurdles in implementing these codes according to the formulation provided by the cited authors.

E.2 Verification of Axisymmetric Potential Flow Methods with a Sphere as a Test Case

In order to check the implementation of the axisymmetric potential flow methods developed, the stream functions generated by the codes were compared to the analytical solution for a sphere. Numerous test simulations were calculated with a range of varying simulation parameters. Figures E.1and E.2 show good results for both the constant strength and linearly varying line source potential flow methods.

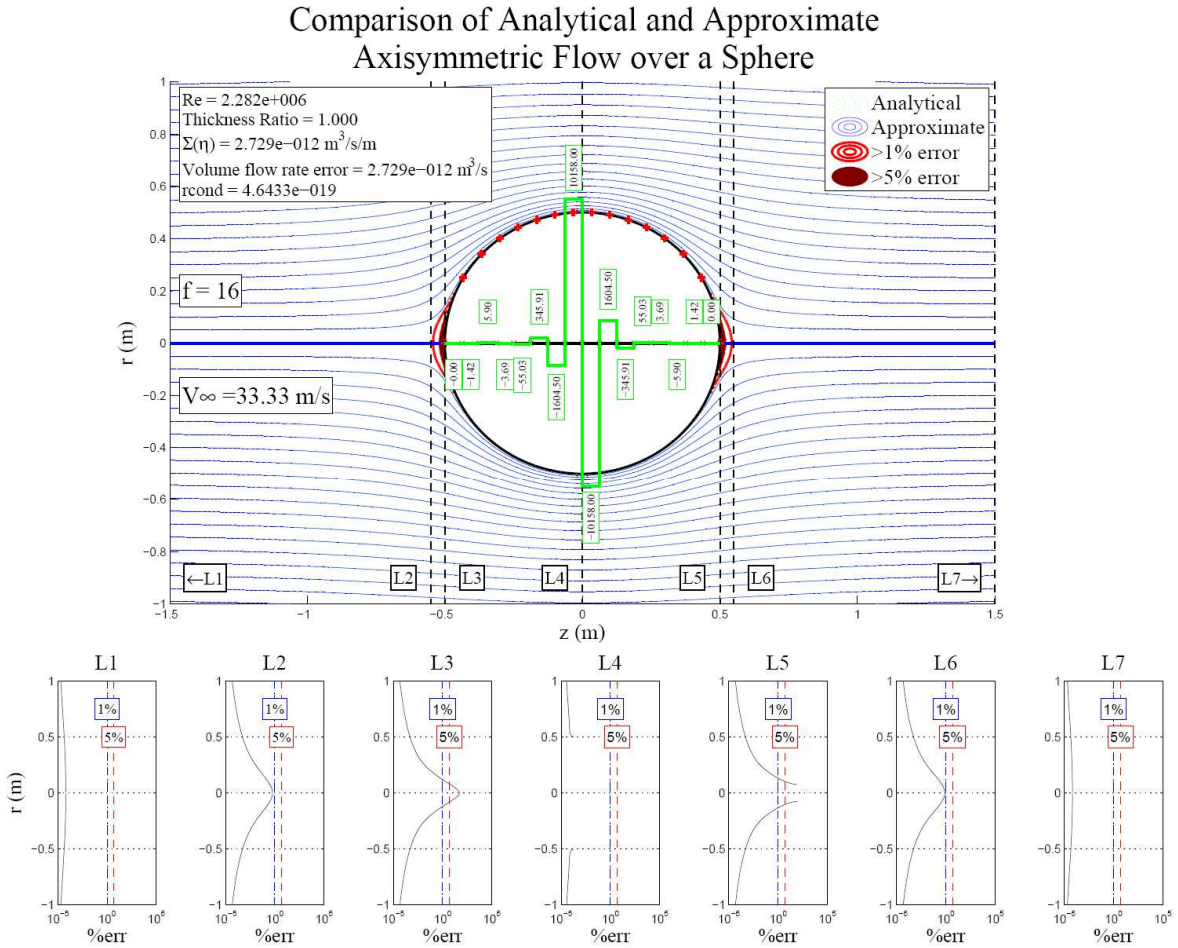

Fig E.1: Comparison of analytical and approximate flow over a sphere with constant strength line sources.

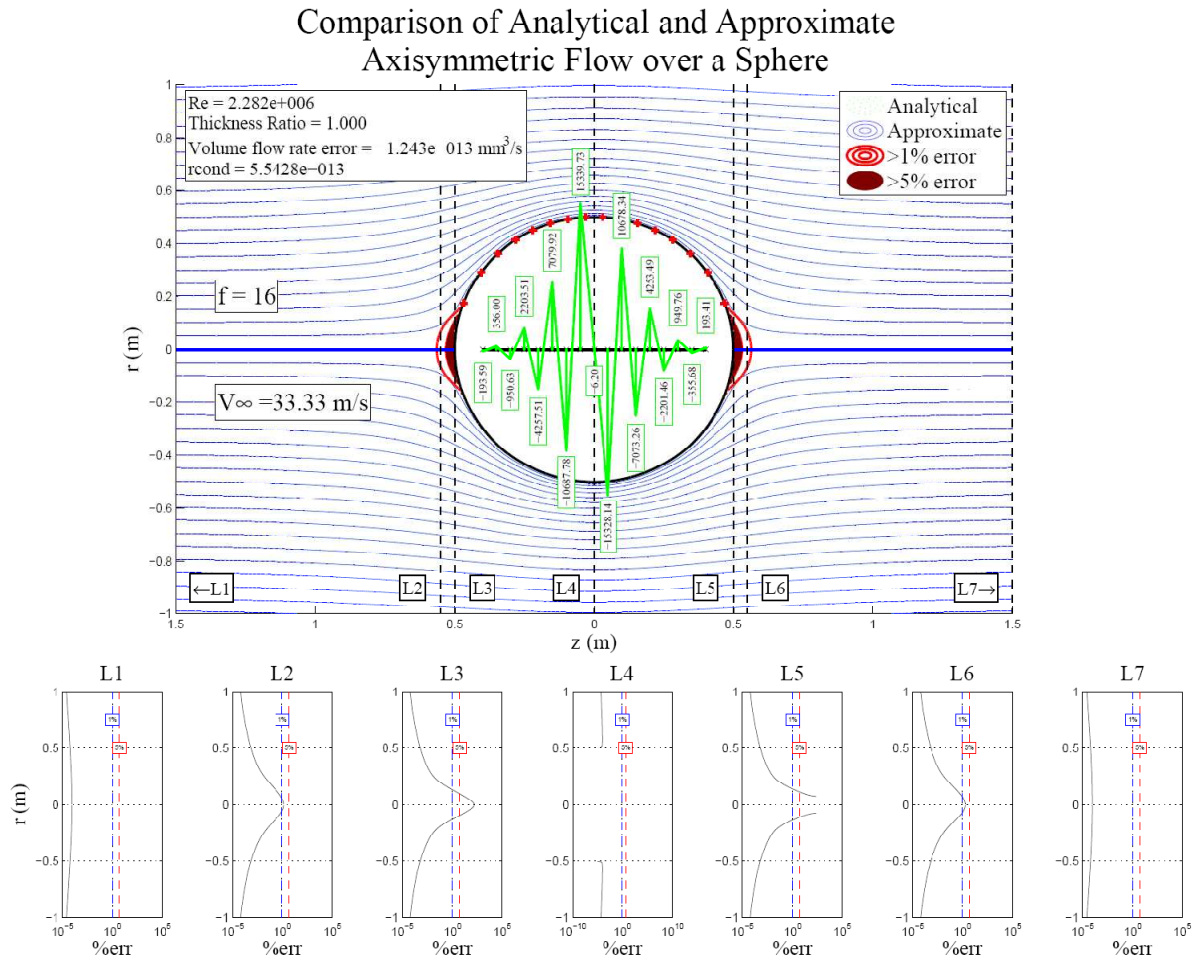

Fig E.2: Comparison of analytical and approximate flow over a sphere with linearly varying line source strengths. The line sources have been inset a distance of 10% of the diameter from each end.

The figures clearly show a very good agreement between the approximate and analytical solutions for both cases. The only areas where any significant errors are visible are near the stagnation points on the spheres. It also happens that for the case of the sphere shown above, the constant strength line sources provide a more accurate solution. It was noted however that the success rate for the linearly varying sources was much higher with different numbers of sources.

The inset of 10% from the edges of the sphere was included as this resulted in an improved solution for the flow. While the optimal inset angle was not easily found, it was an important parameter for the successful modelling of the vehicle. Hess [*69*] stated that the line sources cannot extend to the ends of the body as this will result in infinite singularity strengths at these points. Since there was no inset distance for the constant strength line source solution in Fig. E.1, the importance of insetting the singularities some distance from the ends of the body was noted. Hess continues to state that ellipsoids are not suitable test cases for line source methods as there are exact solutions for the singularity distributions which produce these

bodies. In this case, however, they have been used to test the implementation of a known method and have not been used to validate a new technique.

It should be noted that the success rate for generating results of this agreement is very low, with a large fraction of the results producing unusable solutions. While this might be expected for very low numbers of panels, it is not fully understood why the solutions become erroneous with higher numbers of singularities. The only indication is that the conditioning of the matrix generally becomes worse as the number of panels is increased. But this is not a sure means of predicting a correct solution of the flow.

E.3 Shortcomings and Peculiarities of the Axisymmetric Potential Flow Methods

The methods used for the modelling in this chapter have been noted by several authors to be very unreliable. With regards to the shapes which the method is capable of modelling, it was noted by von Karman [*49*] that not all shapes could be modelled by the constant strength line source method. Zedan and Dalton [*68*] found that the linearly varying source method is capable of modelling inflections whereas the constant strength method is not. Finally, Belykh [*70*] noted the inability of the method to model large aspect ratio bodies with thicknesses greater than their lengths.

The problems encountered with large aspect ratios have been noticed in the testing of the implementation of the method. Also noted is the sensitivity of the solution to the number of singularities used. There is no clear means of determining how many singularities should be used, and how the thickness ratio of the body will affect this. The problem of the inflection points indicates why no solution for the vehicle profile could be found using the constant strength sources.

Also problematic were the generally ill-conditioned equations resulting from the formulation of the problem. This requires that double-precision calculations be conducted to provide good results. The conditioning should be viewed as a separate problem to the issues regarding the shape of the body, and more related to the maximum number of singularities possible.